University of California
Los Angeles

A Deep Survey of the Galactic Plane at Very High Energies

A dissertation submitted in partial satisfaction
of the requirements for the degree
Doctor of Philosophy in Physics

by

Yeuk Chun Chow

2010

The dissertation of Yeuk Chun Chow is approved.

David Saltzberg

Ferdinand Coroniti

Marek Biskup

Rene Ong, Committee Chair

University of California, Los Angeles

2010

To my family

Table of Contents

List of Figures

List of Tables

Acknowledgments

I would like to thank my advisor, Professor Rene Ong, for all his support during my time here at UCLA. Rene is a preeminent scientist and a leader in the field of gamma-ray astronomy and particle physics but more importantly, to me anyway, is that he is a great advisor who genuinely care about his students' progress and well being. This dissertation is not possible without his encouragement and patience all these years.

I would also like to thank our post-doc, and soon to be a professor, Amanda Weinstein. Amanda has been working with me on the sky survey project since the beginning. She is an unspoken leader of the survey group, providing important suggestions and guidances on different aspects of the project. She has also spent countless hours cross checking and correcting some of my analysis. This work would probably have taken much longer without her help.

I am also grateful to my fellow graduate student Matthew Wood. Matt is a very diligent and talented member of our team at UCLA. He and Steve Fegan wrote the ChiLA package which I used for the the survey simulations. Matt has also read a few chapters of this dissertation and provided very valuable feedback. Steve Fegan had helped me a lot when he was in UCLA and his legacy, the ChiLA code, is an essential component of my simulations, so I must thank Steve here.

My thanks to fellow graduate student Tim Arlen for proof reading a part of this dissertation. I also would like to express my appreciation for the many talented undergraduates who have worked with me and our VERITAS group at UCLA, especially Matt Matolcsi, Daniel Margala and Jacob Schwartz who had worked with me in managing the UCLA archive. I have fond memories working with Pierre-Francoys Brousseau and Cyrus Rustomji at the basecamp in the

summer of 2007.

Finally I would like to thank everyone in the VERITAS collaboration because they have all contributed to my work and also I would also like to thank them for building such a great instrument.

Vita

1998-2002	MPhys (Mathematics and Physics), University of Warick, UK
2002-2005	Teaching Assistant, Department of Physics and Astronomy, UCLA
2003 Summer	Summer Research Assistant, Fermi National Laboratory, Illinois
2004	M.S. (Physics), UCLA, Los Angeles, California.
2005-2010	Research Assistant, Department of Physics and Astronomy, UCLA

Publications

V. A. Acciari et al. Discovery of Very High Energy Gamma Rays from PKS 1424+240 and Multiwavelength Constraints on Its Redshift *The Astrophysical Journal Letters, Volume 708, Issue 2, pp. L100-L106 (2010).*

V. A. Acciari et al. A connection between star formation activity and cosmic rays in the starburst galaxy M82 *Nature, Volume 462, Issue 7274, pp. 770-772 (2009).*

V. A. Acciari et al. Detection of Extended VHE Gamma Ray Emission from G106.3+2.7 with Veritas *The Astrophysical Journal Letters, Volume 703, Issue 1, pp. L6-L9 (2009).*

V. A. Acciari et al. Detection of Extended VHE Gamma Ray Emission from

G106.3+2.7 with Veritas *The Astrophysical Journal Letters, Volume 703, Issue 1, pp. L6-L9 (2009).*

V. A. Acciari et al. Simultaneous Multiwavelength Observations of Markarian 421 During Outburst *The Astrophysical Journal, Volume 703, Issue 1, pp. 169-178 (2009).*

V. A.Acciari et al. Radio Imaging of the Very-High-Energy γ-Ray Emission Region in the Central Engine of a Radio Galaxy *Science, Volume 325, Issue 5939, pp. 444 (2009)*

V. A. Acciari et al. Observation of Extended Very High Energy Emission from the Supernova Remnant IC 443 with VERITAS *The Astrophysical Journal Letters, Volume 698, Issue 2, pp. L133-L137 (2009).*

V. A. Acciari et al. Evidence for Long-Term Gamma-Ray and X-Ray Variability from the Unidentified TeV Source HESS J0632+057 *The Astrophysical Journal Letters, Volume 698, Issue 2, pp. L94-L97 (2009).*

V. A. Acciari et al. VERITAS Observations of the BL Lac Object 1ES 1218+304 *The Astrophysical Journal, Volume 695, Issue 2, pp. 1370-1375 (2009).*

V. A. Acciari et al. Multiwavelength Observations of Markarian 421 in 2005-2006 *The Astrophysical Journal, Volume 695, Issue 1, pp. 596-618 (2009).*

V. A. Acciari et al. Veritas Observations of a Very High Energy γ-Ray Flare From the Blazar 3C 66A *The Astrophysical Journal Letters, Volume 693, Issue 2, pp. L104-L108 (2009).*

V. A. Acciari et al. The June 2008 Flare of Markarian 421 from Optical to TeV Energies *The Astrophysical Journal Letters, Volume 691, Issue 1, pp. L13-L19 (2009).*

V. A. Acciari et el. Discovery of Very High Energy Gamma-ray Radiation from the BL Lac 1ES 0806+524 *The Astrophysical Journal Letters, Volume 690, Issue 2, pp. L126-L129 (2009).*

V. A. Acciari et al. VERITAS Discovery of ¿200 GeV Gamma-Ray Emission from the Intermediate-Frequency-Peaked BL Lacertae Object W Comae *The Astrophysical Journal, Volume 684, Issue 2, pp. L73-L77.*

V. A. Acciari et al. VERITAS Observations of the γ-Ray Binary LS I +61 303 *The Astrophysical Journal, Volume 679, Issue 2, pp. 1427-1432.*

M. Wood et al. A Search for Dark Matter Annihilation with the Whipple 10 m Telescope *The Astrophysical Journal, Volume 678, Issue 2, pp. 594-605.*

G. Fossati et al. Multiwavelength Observations of Markarian 421 in 2001 March: An Unprecedented View on the X-Ray/TeV Correlated Variability *The Astrophysical Journal, Volume 677, Issue 2, pp. 906-925.*

A. Konopelko Observations of the Unidentified TeV γ-Ray Source TeV J2032+4130 with the Whipple Observatory 10 m Telescope *The Astrophysical Journal, Volume 658, Issue 2, pp. 1062-1068.*

E. Linton et al. A new search for primordial black hole evaporations using the Whipple gamma-ray telescope *Journal of Cosmology and Astroparticle Physics, Issue 01, pp. 013.*

Abstract of the Dissertation

A Deep Survey of the Galactic Plane at Very High Energies

by

Yeuk Chun Chow

Doctor of Philosophy in Physics

University of California, Los Angeles, 2010

Professor Rene Ong, Chair

The Cygnus region of the Galactic plane contains many known supernova remnants, pulsars, X-Ray sources and GeV emitters which makes it a prime candidate for a Very High Energy (VHE) survey study in the Northern Hemisphere. VERITAS, an array of atmospheric Cherenkov telescopes located in southern Arizona, USA, is the most sensitive very high energy gamma-ray telescope in operation today. Between April 2007 and Fall 2009, VERITAS carried out an extensive survey of the Cygnus region between 67 and 82 degrees in Galactic longitude and between -1 and 4 degrees in Galactic latitude. The survey, comprising more than 140 hours of observations, reached an average VHE flux sensitivity of less than 5% of the Crab Nebula flux at energies above 200 GeV, making it the most sensitive VHE gamma-ray survey ever done in the northern Hemisphere. The survey data set revealed two highly probable gamma-ray sources in the region. A detailed description of the obervational strategy and analysis methodology of the survey are given and a discussion of the scientific implications resulting from the survey is provided.

CHAPTER 1

Introduction

Gamma-ray astronomy is the study of the universe as seen through photons that have energies ranging from 10^6 eV to 10^{20} eV. This is the last band of the electromagnetic spectrum to be investigated since gamma rays are intrinsically difficult to detect on Earth due to their complete absorption by the atmosphere. However with the arrival of gamma-ray satellite telescopes and ground-based atmospheric Cherenkov telescopes, it has become possible to study gamma rays both on and off the Earth's surface. The work carried out in this dissertation is concerned with the very high energy (VHE) part of gamma-ray astronomy, defined as photons having energies above 100 GeV. It was accomplished using the ground-based Very Energetic Radiation Imaging Telescope Array System (VERITAS) to study possible VHE gamma-ray sources in the Cygnus Arm region of the Galactic plane.

In this introductory chapter, an overview of the history of both spaced-based and ground-based gamma-ray astronomy is outlined in section 1.1; then, the production mechanism of VHE gamma rays and the different types of known galactic VHE gamma-ray emitters are discussed in section 1.2. Finally, a review of important results from surveys at GeV/TeV energies is found in section 1.3 and a reading guide to this dissertation is presented in section 1.4.

1.1 Overview of Gamma-ray Astronomy

Gamma rays are photons that are at least 10^6 times more energetic than visible light. The range of energies spanned by gamma rays is at least fourteen decades and it is divided into different sub-ranges which roughly correspond to the different experimental techniques that are suitable for detecting gamma rays. The following scheme of division and nomenclature have been generally accepted by the gamma-ray astronomy community; $\sim$ 10 GeV to $\sim$ 100 GeV is defined as the high energy (HE) band, $\sim$ 100 GeV to $\sim$ 100 TeV is the very high energy (VHE) band, $\sim$ 100 TeV to $\sim$ 100 PeV is the ultra high energy (UHE) band and from $\sim$ 100 PeV to $\sim$ 100 EeV is defined as the extremely high energy (EHE) band. The HE band of energy is currently only accessible by satellite experiments whereas higher energy bands are investigated using ground-based detectors. See Table 1.1 for a description of the detection techniques for the different energies bands. In the following subsections, a brief description of various space-based and ground-based gamma-ray experiments is presented.

1.1.1 Satellite Experiments

The first detection of gamma-ray emission from an astrophysical source is the discovery of the Crab Nebula in 1960s with balloon experiments [1] [2] [3]. Then, a series of pioneering gamma-ray satellite experiments (SAS-II and COS-B) [4], with spark-chamber detectors, established the gamma-ray flux from the Galactic plane and a few isolated sources [5]. However, the major breakthrough in gamma-ray astronomy came in 1991 with the launch of the Compton Gamma-Ray Observatory (CGRO) (figure 1.1).

CGRO had four scientific instruments on board, the Burst and Transient

Energy Range	Nomenclature	Detection Technique
10 GeV - 100 GeV	High Energy (HE)	Satellite pair-production telescope
100 GeV - 100 TeV	Very High Energy (VHE)	Ground-based atmospheric Cherenkov telescope
100 TeV - 100 PeV	Ultra-High Energy (UHE)	Ground-based air shower particle detector
100 PeV - 100 EeV	Extremely High Energy (EHE)	Ground-based air shower particle or air fluorescence detector

Table 1.1: Photon energy ranges and their detection method.

Source Experiment (BATSE), the Oriented Scintillation Spectrometer Experiment (OSSE), the imaging Compton Telescope (COMPTEL) and the Energetic Gamma Ray Experiment Telescope (EGRET) [6]. The four instruments together covered a total of six decades of energy, from 30 keV to 30 GeV. The instrument most relevant to the study of HE and VHE Astronomy was EGRET which was sensitive in the 20 MeV to 30 GeV range. EGRET employed a spark chamber as the particle detector where an incoming gamma ray interacted and the resulting electron/positron pair was tracked; a sodium iodide crystal calorimeter was used to absorb the electron/positron pair to measure its total energy; finally, an anti-coincidence shield was used to reject the cosmic-ray particle background (figure 1.2) [7]. During its nine-year mission, EGRET discovered over 270 point sources of HE gamma rays [8], including over 90 extragalactic gamma-ray emitters, mainly blazars which are a subclass of Active Galactic Nuclei(AGN) [9]. Moreover over 170 of the EGRET sources were unidentified objects, mainly due

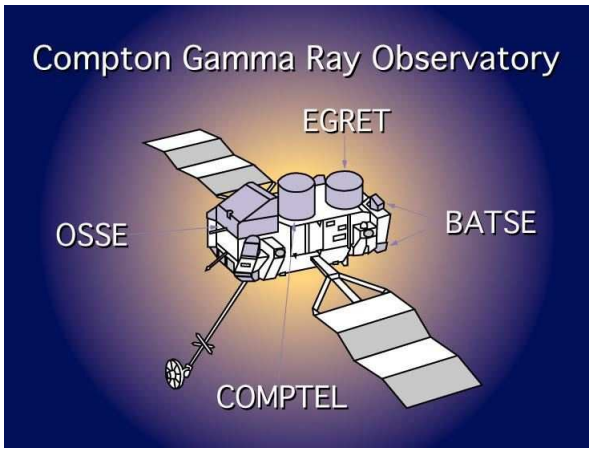

Figure 1.1: A schematic Drawing of the Compton Gamma-Ray Observatory and its four onboard scientific instruments. Figure taken from a NASA website [10].

to the poor angular resolution ($\sim 0.5^{\circ}$) of EGRET. In many cases, more than one optical, X-ray or radio source was found within such a big error circle which made firm identification of the counterpart difficult.

The Fermi Gamma-ray Space Telescope, formerly named GLAST, launched in June 2008, is the successor to the CGRO (figure 1.3). Fermi uses the same design principles as CGRO but with significant enhancement in all aspects of its performance over its predecessor. Fermi carries two instruments on board, the Large Area Telescope (LAT) which covers the energy range between $\sim$ 10 MeV and 300 GeV and the GLAST Burst Monitor (GBM) which monitors gamma-ray bursts (GRBs) of energy between 20 keV and 25 MeV [11]. The LAT has a field of view ($\sim$ 2 steradians) that is twenty times that of EGRET ($\sim$ 0.1 steradians) and an eight times larger collection area. Fermi is at least ten times more sensitive than EGRET at 100 MeV. The positional accuracy of the LAT for point sources is also much improved to be between 30 arcseconds and 5 arcminutes. Within a year of its launch Fermi has already produced significant contributions to HE gamma-ray astronomy, e.g. it has detected over 200 bright HE sources and over

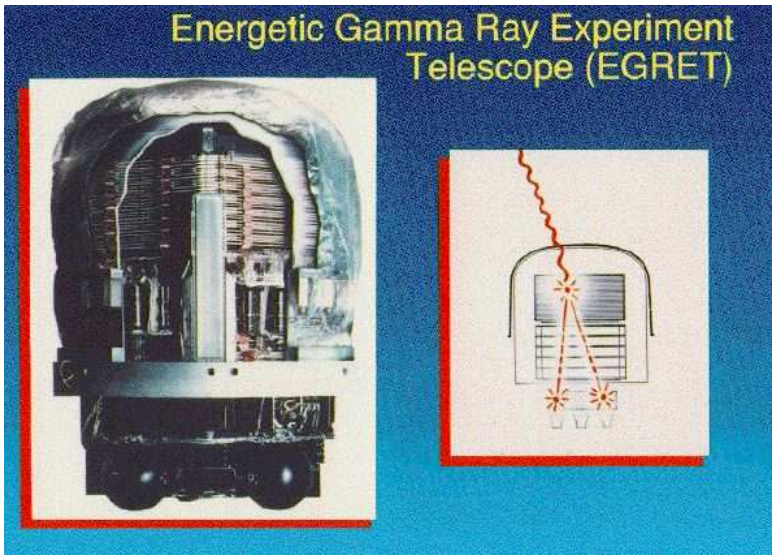

Figure 1.2: A cross sectional view of the structure of EGRET. On the right hand side, an illustration of an incoming gamma ray interacts in the spark chamber and the resulting electron/positron pair is collected in the calorimeter. Figure taken from a NASA website.

25 pulsars from its early data [12].

1.1.2 Ground-based Detectors

At energies higher than $\sim$ 300 GeV, space-based detectors become limited by the rapidly falling power law spectrum of gamma rays due to their small collection area. Fortunately at these higher energies, the gamma ray can interact with the Earth's atmosphere and produce flashes of Cherenkov radiation. Instead of observing the gamma rays directly, ground-based detectors can observe the secondary photons instead. The most successful ground-based detectors are the imaging atmospheric Cherenkov telescopes (IACTs). More details on the production mechanism of Cherenkov radiation and the detection principle of IACTs will be presented in Chapter 2.

Figure 1.3: An artist's rendition of the FERMI telescope in orbit. Figure taken from a NASA website [10].

The first atmospheric Cherenkov telescope was the Harwell air shower array; each of its telescopes was composed of a 25 cm diameter parabolic mirror and a 5 cm photomultiplier tube connected to an amplifier and oscilloscope [13]. The array successfully detected Cherenkov radiation produced from cosmic-ray primaries in the 1950s[14]. Other Cherenkov detectors were constructed in the 60s and 70s but due to their inability to distinguish gamma-ray events from the dominant cosmic-ray background, they were unable to establish any reliable gamma-ray sources. The breakthrough came only after the development of the imaging atmospheric Cherenkov technique first suggested by Weekes and Turver [15]. The pioneering experiment in this new field of gamma-ray astronomy was the Whipple 10 m Telescope on Mount Hopkins in Arizona, USA. Whipple was the first experiment to definitively establish a VHE source, the Crab Nebula in 1989 [16]. After the success of Whipple, a series of similar experiments were set up around the globe in the 1990s including SHALON [17], HEGRA [18], CAT [19], Durham Mark 6 [20], TACTIC [21] and the Crimean Astrophysical Observatory

[22]. Since the early 2000s, a new generation of ground-based VHE gamma-ray detectors have began operation which provide a significant increase in sensitivity over their predecessors. This new generation of new detectors includes HESS [23], MAGIC [24], CANGAROO III [25] and VERITAS. A brief description of some of these ground-based VHE detectors is given below.

Whipple 10m The pioneering IACT Whipple 10m is located on Mount Hopkins in southern Arizona (figure 1.4(a)). The telescope was first constructed in 1968 but has since gone through several upgrades. The elevation of the site is 2300m above sea level. The telescope has a 10 m diameter Davies-Cotton [26] reflector and total mirror surface area of 75 m^2. It also has a 379 pixel camera, a field of view of 3.5° and an energy threshold of 250 GeV. The Whipple telescope has made significant contribution to the field of VHE gamma-ray astronomy, and some highlights of its discoveries are the detection of the Crab Nebula [16], the blazars Markarian 421 [27], Markarian 501 [28], 1ES 2344+514 [29] and H1426+428 [30], and the Galactic Center [31].

HEGRA The HEGRA (High Energy Gamma-Ray Astronomy) experiment (figure 1.4(b)) was the first IACT array system to employ the stereoscopic imaging technique [32]. It was situated on the island of La Palma, Spain. The elevation of the site is 2200 meters above sea level. HEGRA consisted of five small telescopes each equipped with a 3.4 m diameter reflector and a 271 pixel camera. HEGRA field of view was 4.6° and the energy threshold was approximately 500 GeV. Important discoveries made by HEGRA include Cassiopeia A [33], TeV J2032+4130 [34] and radio galaxy M87 [35].

(a) Whipple 10-m Telescope (b) HEGRA Telescope

Figure 1.4: Pictures of second generation IACTs, the Whipple 10-m (left) and one of the five HEGRA telescopes (right).

CANGAROO III The CANGAROO III (Collaboration of Australia and Nippon for Gamma-ray Observatory in the Outback) project is located in Woomera, South Australia at an elevation of 160 m (figure 1.5(a)). It consists of four IACTs each with a 10 m diameter reflector and a 256 pixel camera. The field of view is 3° and the energy threshold is 400 GeV [36]. CANGAROO operates in a pseudo-stereo mode, meaning that each telescope takes its own data and these events are combined later using the events' GPS timestamps.

HESS The HESS (High Energy Stereoscopic System) experiment is the successor to the HEGRA project (figure 1.5(b)). It is located in the Khomas Highland in Namibia at an elevation of 1800 m. It consists of four IACTs occupying the four corners of a 120 m side square. Each telescope is equipped with a 12 m reflector having a total mirror area of 108 m^2 and a 960-pixel camera. The energy threshold of HESS is 100 GeV and it has a large field of view of 5° which makes

it suitable for survey-style observations.

The HESS collaboration is currently constructing a fifth telescope which will have a 24 m diameter reflector with total mirror area of 596m^2 and a 2048-pixel camera. The addition of this new telescope is expected to lower the overall HESS energy threshold to approximately 50 GeV.

MAGIC II The MAGIC (Major Atmospheric Gamma Imaging Cherenkov) telescope is located on La Palma, Spain at an elevation of 2200 m (figure 1.5(c)) [38]. MAGIC has two IACTs, each with a 17 m diameter reflector (largest in the world) and a 576-pixel camera. MAGIC II has the fastest slewing speed among all existing IACTs; the average repositioning time to anywhere in the sky is only 40 s which makes it an ideal instrument for rapid follow up observations after a GRB alert. The field of view of the instrument is 3.8° and the energy threshold is as low as 25 GeV[24].

VERITAS The VERITAS experiment is the successor to the Whipple 10m Telescope and is located on the shoulder of Mount Hopkins at an elevation of 1270m (figure 1.5(d)). The work of this dissertation is carried out using VERITAS and hence a much more detailed technical description of the detector will be given in Chapter 3. Only a brief introduction is given here. VERITAS consists of four IACTs, each equipped with a 12 m reflector and a 499-pixel camera. The field of view is 3.5° and the energy threshold is 100 GeV. At the time of writing of this dissertation, VERITAS is the world's most sensitive VHE gamma-ray telescope.

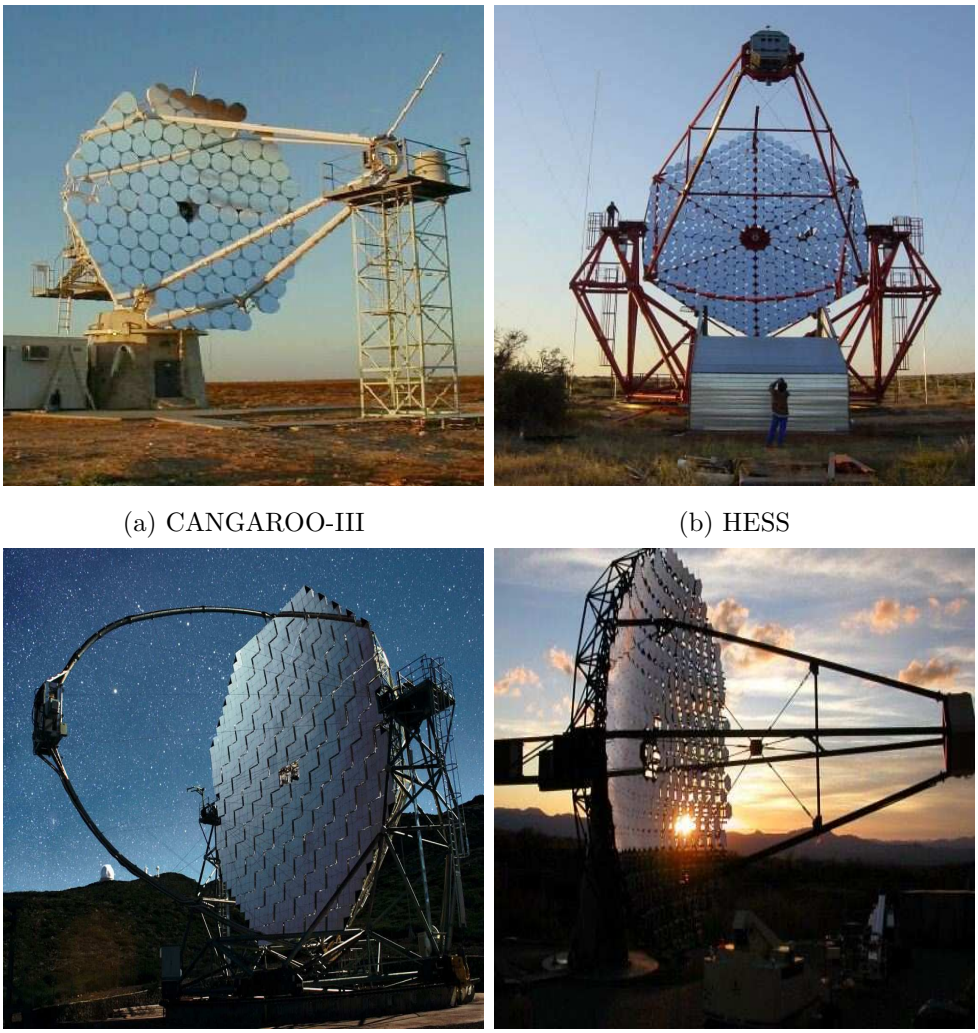

(a) CANGAROO-III (b) HESS

(c) MAGIC-II (d) VERITAS

Figure 1.5: Pictures of third generation IACTs: CANGAROO-III (top left), HESS (top right), MAGIC-II (bottom left) and VERITAS (bottom right).

1.1.3 Alternative Detectors

Besides IACTs there are other ground-based gamma-ray detectors which employ different detection techniques. The two main alternative detectors are air-shower particle detectors and wavefront sampling detectors. A brief introduction is given below.

Air-Shower Particle Detector The prime example of an air-shower particle detector is the Milagro experiment, which was a water Cherenkov air-shower detector. It was located in New Mexico at an elevation of 2630 m. The detector consisted of a 5000 m^2 pond filled with 6 million gallons of water together with 175 out-rigger water tanks [39]. The pond had two layers of photomultiplier tubes (PMTs), the first layer was used to detect Cherenkov radiation and the second deeper layer was used for detecting the more penetrating components of cosmic-ray showers for background rejection. The 175 out-rigger tanks, each equipped with a single PMT, were distributed in an area over 40,000 m^2 surrounding the main pond. The addition of these outriggers improved the angular resolution and increased the overall sensitivity of the instrument. The energy threshold of Milagro was approximately 100 GeV [40]. Milagro ceased operation in April 2008 and a successor experiment, called HAWC, is planned for a site in Mexico [41].

Wavefront Sampling Another approach is wavefront sampling and examples of these instruments include CELESTE [42], STACEE [43], GRAAL [44] and Solar Two [45]. These experiments utilized large arrays of reflecting mirrors, called heliostats, to reflect Cherenkov light in gamma-ray air shower, to an elevated collecting station. Due to the large mirror area, the energy threshold of these experiments was as low as 100 GeV. Currently there is no instruments in operation

(a) MILAGRO (b) STACEE

Figure 1.6: Alternative ground-based gamma-ray detectors. Left: The air shower particle detector Milagro. Right: the wavefront sampling detector STACEE.

that utilizes the wavefront sampling technique.

1.2 VHE Gamma Ray Production Mechanisms

Other branches of astronomy mainly investigate the thermal radiation of astrophysical objects. A typical surface temperature of 5000 K emits visible light according to Planck's law of radiation, and for even hotter objects like the accretion disk around neutron stars or black holes, electromagnetic radiation as energetic as X-rays can be produced. However, this is still several orders of magnitude below VHE gamma rays and hence it is clear that VHE gamma rays are produced by non-thermal processes. The two main processes that are most likely to produce VHE gamma rays are the decays of neutral pions and the inverse-Compton scattering of electrons. A brief introduction to the two processes is given below.

Decay of Neutral Pions Collisions of nucleons that can occur around astrophysical objects can produce neutral pions, π^0, which have a half-life of 8.4×10^{-17}s and a predominant decay mode into two photons. If the pion decays at rest, the resulting photons will each have an energy of $\frac{1}{2}m_{\pi^0}c^2$ where m_{π^0} is the rest mass of the pion and c is the speed of light in vacuum. But most π^0's do not decay at rest since they are mainly produced from collisions or decays of other hadrons. If the π^0 decays while moving at relativistic speeds, the photons produced can then have energies in the GeV - PeV range.

Inverse-Compton Scatterings of electrons Low energy photons can be up-scattered by high energy electrons into the gamma-ray energy range. This scattering process is called inverse Compton scattering (figure 1.7). Since low energy photons are present everywhere in the universe, VHE gamma rays can be produced near any astrophysical object that has an acceleration mechanism for charged particles, e.g. supernova remnants (SNRs), pulsars or active galactic nuclei (AGN).

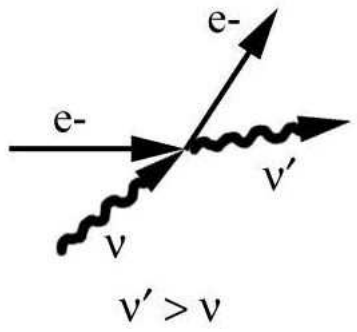

Figure 1.7: The inverse-Compton scattering process where a photon is upscattered to higher energy by an electron.

1.3 Motivations for VHE Gamma-ray Astronomy and Sky Survey

A VHE gamma ray has ean nergy that is more than ten orders of magnitude greater than a typical photon. The conventional thermal radiation production mechanisms therefore cannot explain the sources of these gamma rays. Instead, one would expect that these gamma rays to be produced via particle interactions in powerful acceleration sites in the universe. Known sources of VHE gamma rays include supernova remnants (SNRs), and its subclass pulsar wind nebulae (PWN), microquasars and active galactic nuclei (AGN). These astrophysical objects all contain powerful acceleration sites that can accelerate particles to very high energies, e.g. powerful magnetic fields produced by the pulsar in PWNs, and relativistic in from AGNs and microquasars. Furthermore, there may be gamma-ray sources that involve non-standard physics, for example, gamma rays produced from the decay or annihilation of particles beyond the Standard Model (e.g. dark matter). In summary, VHE gamma-ray astronomy provides a window to study physics in extreme conditions or involving unknown physical processes that are not accessible to conventional astronomical techniques.

Another important motivation for VHE gamma-ray astronomy is the question of the origin of the cosmic rays. Cosmic rays were discovered more than 90 years ago by Victor Hess but their origin still remains mysterious today. Cosmic-ray particles are the largest source of extra-solar material that reach Earth everyday and they have some remarkable properties. For example, they span over fourteen decades of energies from 10^6 eV to 10^{20} eV. They have an energy density of ~ 1 eVcm^{-3}, similar to the energy densities of the Galactic magnetic field and the cosmic microwave background. The sources that power the cosmic rays must have a total luminosity of more than 10^{41} erg s^{-1}. The galactic containment time

is estimated to be $\sim 10^6$ yr but there is evidence that cosmic rays have existed as long as the galaxy itself ($\sim 10^{10}$ yr), this suggests that cosmic rays are being replenished continuously [46].

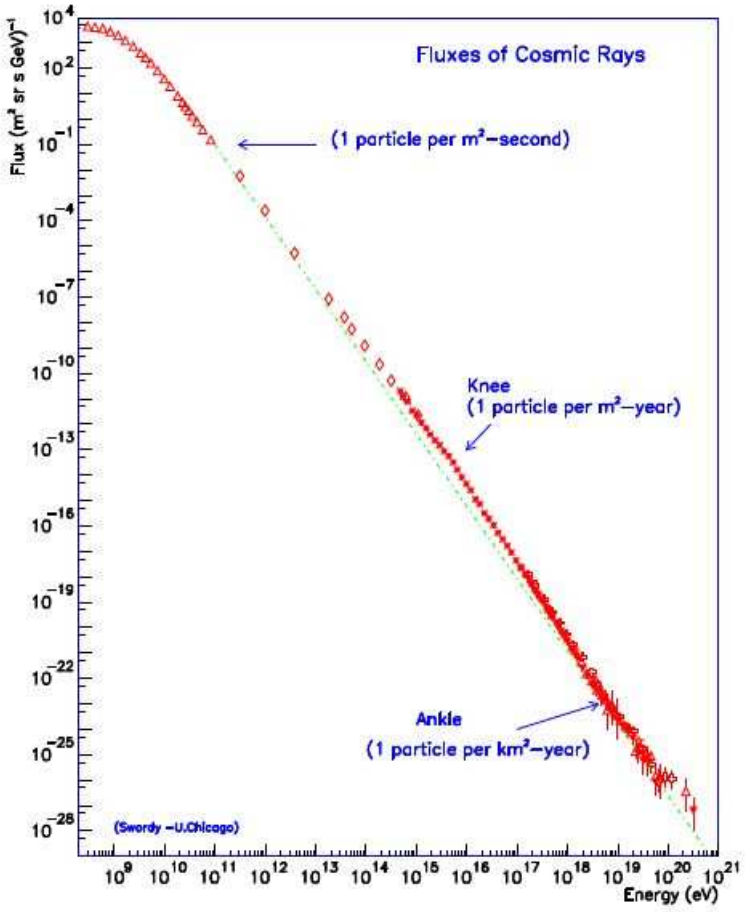

Figure 1.8: The cosmic-ray energy spectrum. The spectrum follows a nearly perfect power law for more than ten decades. The two distinctive features, the knee and the ankle are as shown on the plot. Figure taken from [47].

The energy spectrum of cosmic rays follows a near perfect power law for more than ten decades and there are two distinctive features, the knee at 10^{15} eV and the ankle at 10^{18} eV. The origin, acceleration and propagation mechanism

of the cosmic rays at MeV and GeV energies are reasonably well understood [48]. However, the exact sites of acceleration for particles above 10^{12} eV remain unknown even after decades of research. The difficulty arises from the deflections of the charged cosmic-ray particles by the interstellar magnetic fields. By the time cosmic rays arrive on Earth, their directional information has already been lost to the magnetic fields.

The favorite candidates responsible for cosmic rays up to $\sim 10^{14}$ eV are the Galactic supernova remnants (SNRs).The first reason is that supernovae and the resulting SNRs are the only known galactic objects that can provide the necessary amount of energy for cosmic rays. A typical supernova explosion releases 10^{51} ergs of kinetic energy and a supernova explosion happens once every few decades in our Galaxy. This means that supernovae inject on average 10^{42} erg s^{-1} of power into the interstellar medium. This is sufficient to power the cosmic rays if 10% of the kinetic energy from these supernovae is converted into the acceleration of the protons and nuclei in the galaxy. The other reason that favors SNRs being the acceleration sites is that there is a well established particle acceleration model called Fermi acceleration (or diffusive shock acceleration). In this model, the ejected charged particles from the explosion sweep up a cloud of stationary material to produce a shock front. A charged particle can diffuse back and forth accross the shock front and scatter off the magetic irregularities on either side. Assuming that the velocity distribution is isotropic on either side of the shock front, the charged particle diffusing from one side to the other sees a converging flow of scattering centers and gains energy each time it crosses the shock front [49]. The acceleration continues until the charged particle can escape the shock front. It can be shown that the diffusive shock mechanism leads to a power law spectrum of the accelerated particles with a spectral index of ~ 2 [50].

As mentioned earlier, the charged cosmic rays cannot be used to determine the acceleration sites because they are deflected by intergalactic magnetic fields. So, instead of relying on the charged cosmic rays, one can use the high energy neutral particles instead, such as neutrinos or gamma rays, to determine the sites of the acceleration since they are unaffected by magnetic fields and can point directly back to their origin. By discovering Galactic VHE gamma-ray sources, we can help to explain the origin of cosmic rays. Over the last two decades, many VHE gamma-ray sources have been discovered. A brief description of the various Galactic sources and a review of the recent GeV/TeV survey results are given in sections 1.3.1 and 1.3.2 respectively.

1.3.1 Galactic VHE Gamma-ray Sources

The recent advances of ground-based instruments, especially using the imaging atmospheric Cherenkov technique, have led to the discovery of different types of VHE gamma-ray emitters. Both Galactic and extra-Galactic VHE sources have been detected. Known sources of Galactic origin include supernova remnants (SNRs), pulsar wind nebulae (PWN) and microquasars, and sources of extra-Galactic origin are different types of active galactic nuclei (AGN). There are also many unidentified Galactic VHE sources, sources that have no known astrophysical counterparts in other wavebands. A brief description of each type of known Galactic VHE emitters is presented below.

Supernova Remnants The expanding shell of gas after a supernova explosion, which includes material from the supernova and any interstellar material swept up by the explosion, is called the supernova remnant (SNR). SNRs are divided into two main categories; the first is shell-type SNRs whose observed radiation

comes from the interaction of the supernova shell and interstellar medium with no apparent central power source (figure 1.8(a)). The second type of SNR is the plerion type which is formed when the core of the original star remains after the explosion as a compact object, i.e. as a neutron star or a black hole.

The life cycle of shell-type SNR can be divided into four phases. The first phase is the free expansion phase where the shell expands at a constant velocity and the temperature inside the SNR remains constant. The first phase can last for several hundreds years. The second phase, called the Sedov phase, is the adiabatic expansion of the shell. In this stage, the kinetic energy from the expansion is transferred to the internal energy of the system. The total energy stays constant (adiabatic). The radius, r, of the SNR during this phase is proportional to $t^{2/5}$ where t is the elapsed time. The third stage of the evolution is the "Snow-plough" phase, or the radiative phase. At this point, the shell cools down quickly due to radiation loss. A thin shell is formed and it radiates most of its energy through optical emission. The final stage is the merging phase. When the expansion speed drops to a level comparable to the interstellar medium (ISM), the SNR begin to dissolve and mix into the ISM. More detailed discussion of the evolution of shell-type SNRs can be found in [52].

As discussed previously, SNRs are favorite candidates as the acceleration sites for the cosmic rays. As of July, 2009 more than ten shell-type SNRs have been confirmed as VHE gamma-ray sources. Some of these SNRs are coincident with locations of molecular clouds (for examples, W28 [53] and IC443 [54]) which provide some evidence for proton acceleration.

Pulsar Wind Nebulae A particularly interesting type of plerion for VHE gamma-ray astronomers is one that contains a pulsar, called pulsar wind nebulae

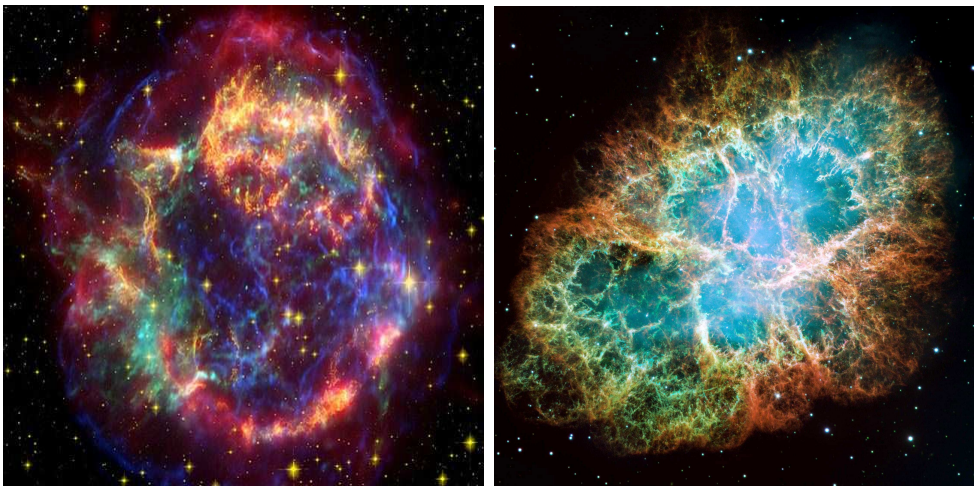

(a) Cassiopeia A (b) Crab Nebula

Figure 1.9: Examples of SNRs. Left: a Spitzer Space Telescope image of the shell type SNR Cassiopeia A. Right: a Hubble Space Telescope image of the Crab Nebula, a pulsar wind nebulae and the standard candle of VHE Astronomy. Figures taken from [10].

(PWN). The rapidly rotating pulsar produces enormous electric and magnetic fields which can accelerate charged particles, resulting in a relativistic wind of energetic particles called the pulsar wind. The wind can then interacts with the supernova shell to produces VHE gamma rays through the synchrotron and inverse Compton scattering processes. The first VHE source detected, and indeed still the most important VHE source, is the PWN Crab Nebula (figure 1.8(b)). The Crab was first observed by Chinese astronomers in the year 1054 and it was detected as a VHE gamma-ray source by the Whipple Observatory in 1989. As the only strong steady VHE source detected so far, it is tremendously helpful in calibrating any VHE gamma-ray instrument and for the optimization of analysis algorithms.

Microquasars A microquasar is a binary system consisting of a star orbiting a dense compact object such as a black hole or a neutron star (figure 1.10). The gravitational force of the compact object removes material from the star to form an accretion disk. In a system that contains a black hole, relativistic outflows of material, called jets, have been observed in which particles can be accelerated to high energies. A microquasar of this type is thus very similar to an active galactic nucleus but on a much smaller scale. VHE gamma rays are believed to be produced by inverse Compton scattering of background photons with the high energy electrons in the jet or by the decays of neutral pions produced from hadronic interactions that can occur in the jet [55]. On the other hand, in a binary system that contains a neutron star, it has been suggested that the accreting matter can penetrate into the magnetosphere of the neutron star. The matter can interact with the enormous magnetic field and produce a shock region where particles can be accelerated. VHE gamma rays can then be produced through inverse Compton scatterings with the electrons in the shock region [56]. Two microquasars have been firmly detected at VHE energies so far. They are LS 5039 [57] and LSI +61 303 [58].

1.3.2 Surveys at GeV/TeV Energies

As discussed earlier, gamma-ray astronomy explores the least understood part of the electromagnetic spectrum, therefore it is important to discover new VHE sources in order to uncover new astrophysical phenomena and to help explain the origin of the cosmic rays. In the last two decades, there has been tremendous progress in the field of gamma-ray astronomy. Systematic surveys at GeV/TeV energies have been successfully performed by different groups resulting in a large number of new sources. Highlights of these results are presented below.

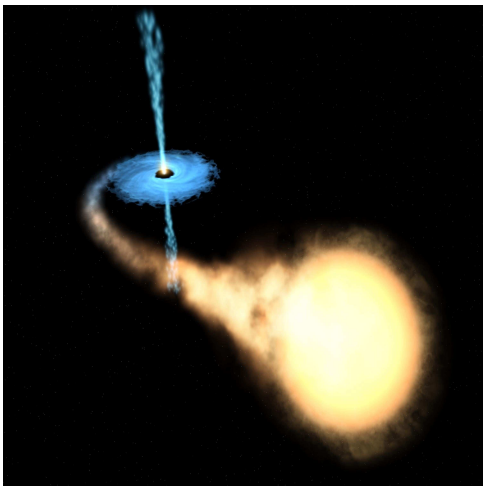

Figure 1.10: An artist rendition of a microquasar showing the accretion disk and the jets from the central compact object.

EGRET The pioneering satellite gamma-ray detector systematically scanned the entire sky for gamma-ray sources over its nine year life span. In the third EGRET catalog [8], 271 sources were detected of which 6 are pulsars, ~ 70 are AGNs and the majority are unidentified objects (~ 170) (See figure 1.11).

HEGRA HEGRA was a second generation IACT array. It undertook a Galactic plane survey in 1997-1998, covering the region $0^\circ \leq l \leq 83.5^\circ$ and $-2^\circ \leq b \leq 2^\circ$, where l and b are the Galactic longitude and latitude respectively. The sensitivity of the survey was at the 20% Crab level. One VHE source, TeV 2032 was discovered [59].

Milagro Milagro was a water Cherenkov extensive air shower array, it performed an all sky survey in the Northern Hemisphere with moderate exposure in the region $30^\circ \leq l \leq 220^\circ$ and $-10^\circ \leq b \leq 10^\circ$ between 2000 and 2007. Three new TeV sources were discovered [60] [61]. It should be noted that because of its

different detection technique, Milagro has a higher energy threshold then other ground-based instruments. It was most sensitive to energies above ~ 10 TeV [40] (See figure 1.12)

HESS HESS performed a survey of the Galactic plane region ($-30^\circ \leq l \leq 30^\circ$ and $-3^\circ \leq b \leq 3^\circ$) in 2004 and 2005. The sensitivity of the survey was at the 3 % Crab Nebula flux level. HESS discovered 17 new VHE point sources in this survey [62]. The HESS result was significant in that it practically doubled the number of known VHE objects. Some of these new sources have strong association with known SNRs or pulsars, but the majority of them are unidentified sources i.e. there are no unambiguous counterparts for these sources in other wavebands. Another Galactic plane survey was performed between 2005 and 2007 in the region $30^\circ \leq l \leq 60^\circ$ and $-3^\circ \leq b \leq 3^\circ$, no new sources were discovered, but one of the sources reported by Milagro was confirmed [63]. (See figure 1.13)

1.3.3 Motivations for the Sky Survey in the Cygnus Region

The results presented in the previous section show that modern gamma-ray experiments have greatly advanced our knowledge of the high energy universe. However, there is still much to be done especially if we are to explain the origin of cosmic rays. Although the surveys carried out by those instruments have been very successful, they only covered portion of the Galactic plane and a relatively narrow energy regime. For example, although HESS had a very successful sky survey campaign, it is located in the Southern Hemisphere and hence it is best suited for them to explore the Galactic center region. Milagro was able to perform an all sky survey but its energy regime is ≥ 10 TeV. For these reasons, there is a compelling case for a deep survey outside the Galactic center in the Northern

Hemisphere. VERITAS is the ideal instrument to carry out this task.

VERITAS is currently the most sensitive IACT and its location enables it to scan Galactic plane regions that are inaccessible to HESS. VERITAS also operates at a much lower energy regime than Milagro, i.e. at $\sim 200GeV$ TeV. With its sensitivity and energy threshold, VERITAS is well equipped to carry out a deep survey in the Northern Hemisphere that will complement the Galactic center survey done by HESS.

Because of the importance of the sky survey project, the VERITAS collaboration designated it as a key science project for its first two years of operation (2007-2009). The region chosen for the survey is the Cygnus Arm region in Galactic longitude between 67° and 82° and in Galactic latitude between $-1°$ and 4°. The Cygnus region was chosen because it is an interesting region with many known astrophysical objects in different wavebands. In the proposed survey region, there are 1416 X-ray sources [64], 2 pulsars [65], 9 SNRs [66], 6 X-ray binaries [67] and 4 EGRET unidentified GeV sources [8]. This arm includes the Cygnus OB2 region, an active star formation region. With such an abundance of interesting astrophysical objects, the Cygnus arm region has high potential for discovery in the VHE regime.

From 2007 and 2009, VERITAS scanned the proposed area of the Cygnus arm region. A total of more than 140 hours of data were taken reaching an average flux sensitivity of 5% of the Crab Nebula at energies above 200 GeV. The detialed results from this survey will be presented in Chapter 5.

1.4 Guide to this Dissertation

Following this introductory chapter, the detection technique of ground-based imaging atmospheric Cherenkov telescopes is discussed in Chapter 2. In Chapter 3, a detailed technical description of VERITAS is given. Analysis methods used by IACTs then follow in Chapter 4. Finally, the results from the VERITAS sky survey are presented in Chapter 5. A discussion of the results and the outlook for future observations is in Chapter 6.

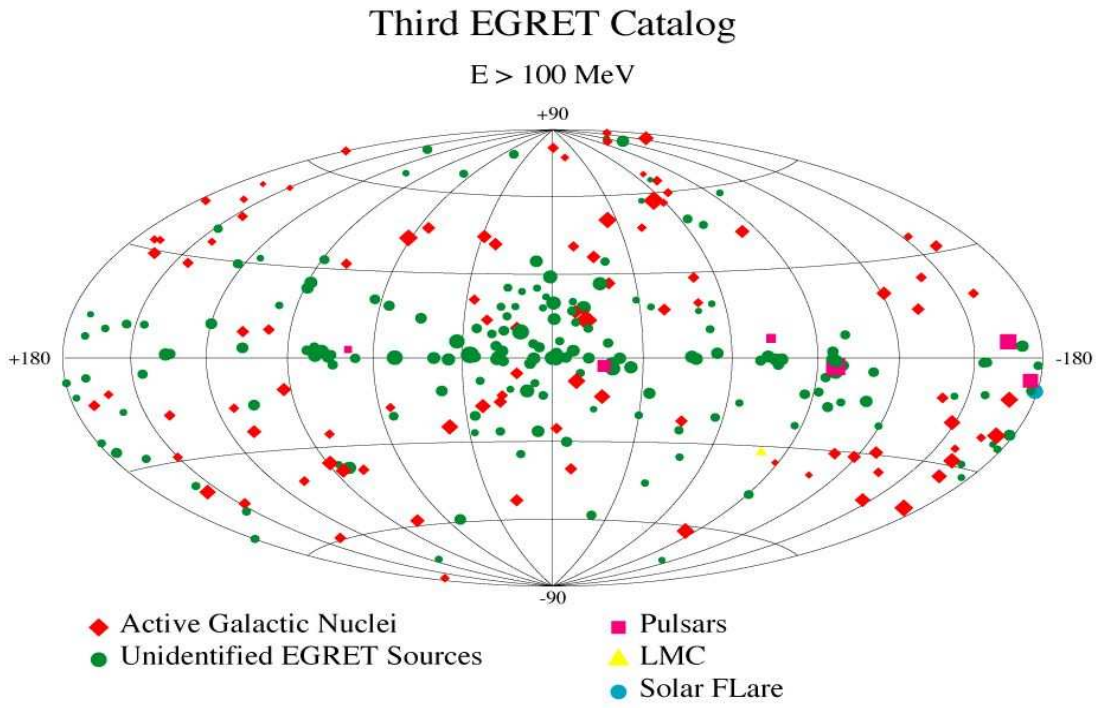

Figure 1.11: The point sources from the EGRET 3rd Catalog. EGRET was a satellite gamma-ray detector sensitive to photons with energies from 100 MeV to a few GeV. This plot shows the gamma-ray point sources detected by EGRET. The different symbols represent the astrophysical objects associated to these gamma-ray emitters. One can see that the majority of these point sources are unidentified, i.e. there is no firm association to other known astrophysical object. Figure taken from [68].

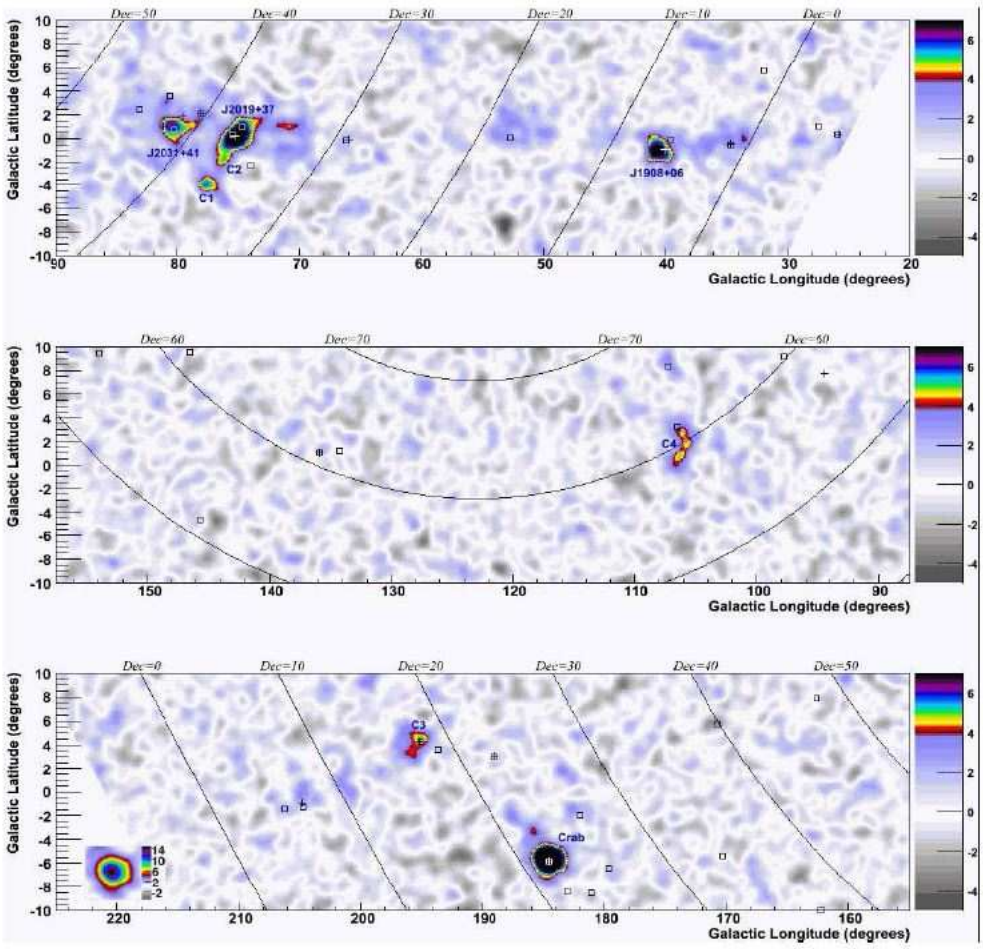

Figure 1.12: Milagro was an air shower particle detector that operated at ~ 10 TeV. This plot shows the significance map, in Galactic coordinate, from their 2001-2007 Galactic plane survey. Three new sources were discovered at the ~ 10 TeV energy regime and their locations are shown in the top panel. In the bottom panel, one can see the well known VHE source, the Crab Nebula. Figure taken from [61].

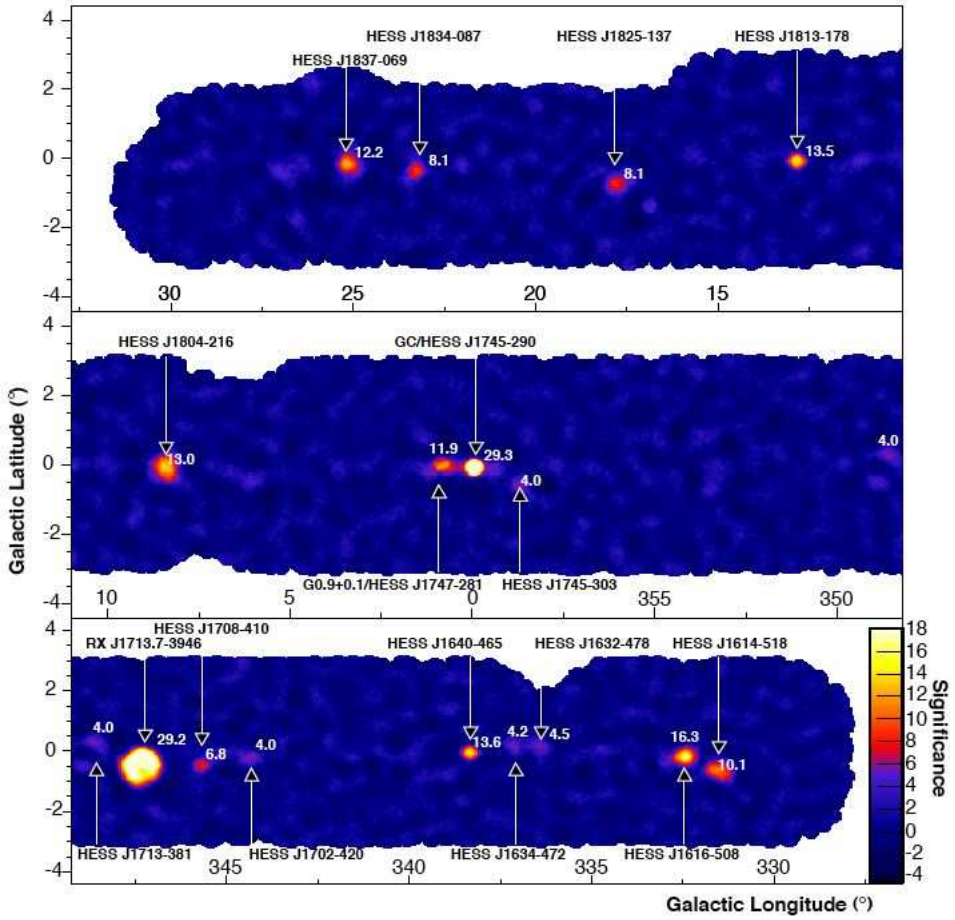

Figure 1.13: HESS is a third generation IACT located in Namibia. The plot shows the significance map, in Galactic coordinates, from their Galactic center survey at $\geq$ 200GeV. The survey was very successful and they have discovered 17 new VHE gamma-ray sources. Many of these sources are unidentified which mean they have no known counterparts in other wavebands. Figure taken from [62].

CHAPTER 2

Ground-based VHE Gamma-ray Detection

An important property of gamma rays is that they are electrically neutral and therefore they do not get deflected by magnetic fields in space. This means that, unlike charged comic rays, gamma rays can be traced back directly to their origin and thus provide important information regarding their sources.

Since the Earth's atmosphere is opaque to gamma rays, it is impossible to detect them directly on the ground. There are currently two types of high energy gamma-ray detectors. The first type is the space-based satellite instrument. However since it is prohibitively expensive to launch a large object into orbit, gamma-ray satellites can only have a small collection area (of order of magnitude $\sim 1\text{m}^2$). The fast falling energy spectra of gamma-ray sources and the small collection area of satellite experiments means that they have a practical energy limit of about 100 GeV for most sources. The second type of gamma-ray experiment is the ground-based imaging atmospheric Cherenkov telescope which observes the Cherenkov radiation emitted from secondary particles produced by the interaction of very high energy (VHE) gamma rays with the atmosphere. The current generation of IACTs are sensitive to the energy range of approximately 50 GeV - 50 TeV.

In this chapter, the physical processes involved in the development of air showers will be discussed in section 2.1; the production mechanism of Cherenkov radiation in the air shower will be presented in section 2.2; finally, a general

introduction to the imaging atmospheric Cherenkov technique is presented in Section 2.3.

2.1 Production of Air Showers

When a gamma ray or a charged cosmic-ray particle enters the atmosphere, it interacts with the atmospheric molecules to produce secondary particles. The secondary particles in turn interact with more atmospheric molecules which leads to the development of a cascade of particles called an air shower. The physical processes governing the interactions are briefly discussed below.

Bremsstrahlung Bremsstrahlung radiation, or "braking radiation", is produced when a charged particle is deflected, i.e. accelerated, by an electric field, for example, of an atomic nucleus in the atmosphere. The interaction probability is inversely proportional to the particle mass and hence this radiation process is dominated by electrons and positrons. The radiation length, the distance traveled by a particle when it loses on average e^{-1} of its energy, of an electron in the atmosphere is 37.7 $\mathrm{g \cdot cm^{-2}}$. The photons are emitted in the bremsstrahlung process within an opening angle given by $\frac{\mu c^2}{E}$ where μ, E are the mass and energy of the particle and c is the speed of light in vacuum [69].

Pair Production Pair production is the production of an electron/positron pair from the interaction of a high energy photon and a molecule. The photon energy must exceed the combined rest mass energy of the electron/positron pair.

Strong Interactions When a hadron, a proton for example, collides with a nucleus in the atmosphere, it will produce other hadrons or nuclear fragments,

akin to what would happen in a particle accelerator experiment.

Coulomb Scattering Coulomb scattering, or Rutherford Scattering, is the elastic scattering of a charged particle by the electric field of another charged particle.

Compton Scattering Compton Scattering is the inelastic scattering of a photon on a free electron. The photon loses some energy in this process and thus its wavelength is shifted. The shift in wavelength is given by $\lambda' - \lambda = \frac{h}{m_e c}(1 - \cos\theta)$, where λ', λ are the wavelengths of the photon after and before the scattering respectively, m_e is the mass of an electron, c is the speed of light and θ is the angle of scattering.

Ionization Ionization is the removal of an electron from an atom or molecule due to the inelastic collision of an incoming particle. Ionization is the main process by which the air shower loses its energy.

2.1.1 Gamma-ray Initiated Air Showers

When a high energy gamma ray enters the atmosphere, it interacts with the atmospheric molecules and is converted into a relativistic electron/positron pair via the pair production mechanism. The electron and positron then interact with other air molecules to produce high energy photons via the bremsstrahlung process. These photons then produce more electron/positron pairs which, in turn, produce more photons by bremsstrahlung. The process repeats itself, producing a cascade of electromagnetic particles at an exponential rate until the energy of the particles falls below the critical energy, i.e. when the energy loss per unit length due to bremsstrahlung is equal to the energy loss per unit length due to ionization ($\sim$ 81 MeV) (figure 2.1). At this point, called the shower maximum,

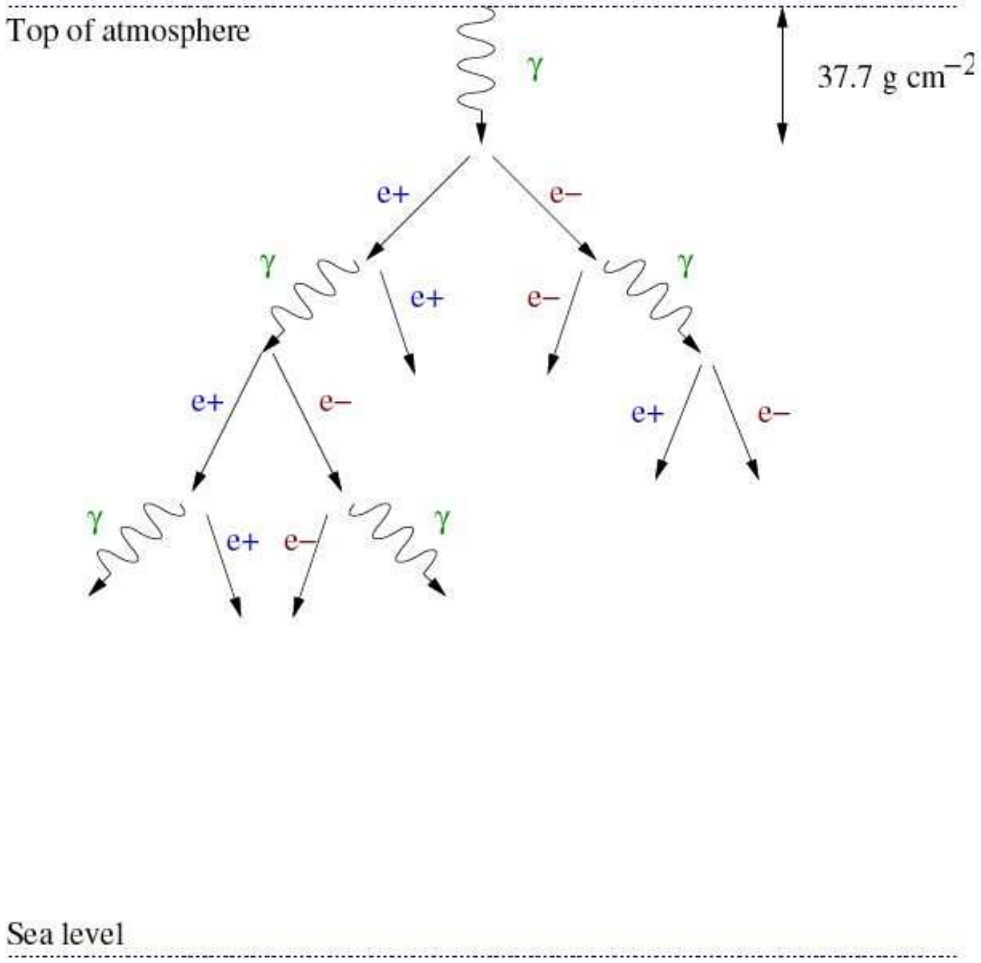

Figure 2.1: A schematic representation of the development of a gamma ray initiated air shower. After the first radiation length, 37.7 g $\cdot$ cm^2 (the total depth to sea level is $\sim$ 1000 g $\cdot$ cm^2), the primary gamma ray interacts to produce an electron/positron pair. The electron and positron both radiate photons through the bremsstrahlung process which results in a cascade of electromagnetic particles. Figure taken from [70].

the air shower reaches the maximum number of particles it will have. This number is proportional to the energy of the original gamma ray. For a 1 TeV gamma ray, the typical height for the first interaction is ~ 25 km above sea level, the shower maximum occurs at ~ 8 km above sea level and the number of secondary particles produced is on the order of 10^4.

After the shower maximum, the air shower loses its energy by various processes. The electrons lose energy mainly through ionization and Coulomb scattering whereas the photons lose energy through the Compton scattering process.

2.1.2 Cosmic-Ray Initiated Air Showers

When cosmic-ray hadrons, mostly protons and a small contribution of helium nuclei, enter the atmosphere, they collide and interact with air molecules through the strong nuclear force. There are three components to a cosmic-ray induced air shower. The first is the hadronic component: after a collision with an air molecule, some of the particles that are produced include nuclear fragments of the target molecules, more protons and neutrons, hyperons and also mesons like pions and kaons. These hadrons can further interact with other air molecules producing a cascade of hadronic particles.

The second component is the electromagnetic component of the shower. The neutral pions (π^0) produced by the strong interaction decay into two photons via the process $\pi^0 \rightarrow \gamma + \gamma$. Given sufficient energy, the photons pair-produce an electron/positron pair which can then produce more photons via bremsstrahlung and the process repeats itself to produce an electromagnetic shower the same way as described in the previous section.

The final component is the muonic shower component. The charged pions ($\pi^{\pm}$) produced from the strong interactions decay into muons via the processes,

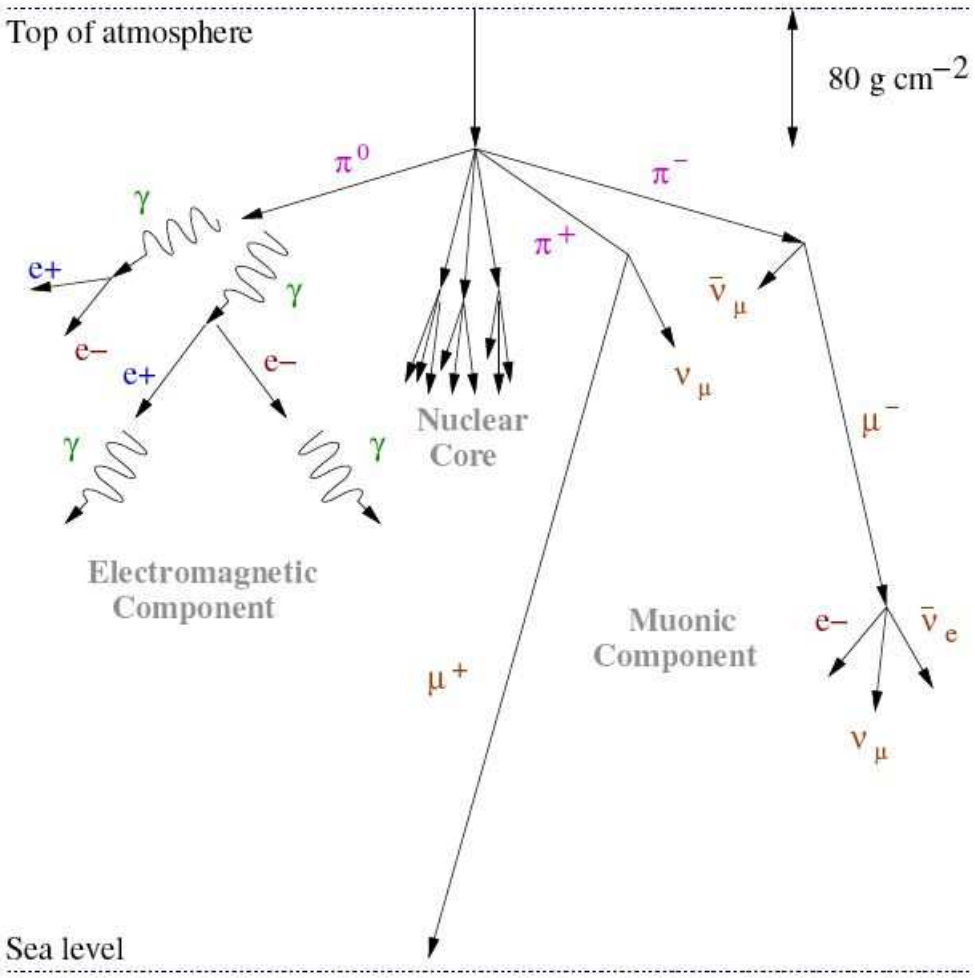

Figure 2.2: A schematic representation of the development of a hadron initiated air shower. The primary hadron enters the atmosphere and after the first absorption length of 80 g $\cdot$ cm^2 (the total depth to sea level is $\sim$ 1000 g $\cdot$ cm^2). It produces more hadronic fragments through the strong interaction. Different types of hadrons lead to the development of different types of particle cascades. The neutral pions lead to electromagnetic showers similar to the gamma-ray shower. Charged pions produces muonic showers and other nuclear fragments and hadrons produce a cascade of hadronic particles. Figure taken from [70].

$\pi^+ \rightarrow \mu^+ + \nu_\mu$ and $\pi^- \rightarrow \mu^- + \nu_\mu$. The muons have a life time of 2.2μs and, given sufficient energy, they can reach ground level, or else they can decay into electrons which then produce yet another electromagnetic shower component. The production mechanism of a cosmic-ray air shower is depicted in figure 2.2.

2.2 Cherenkov Radiation

Although most of the air shower particles will be absorbed by the atmosphere or will decay before they reach the ground, they travel at relativistic speeds higher than the phase velocity of light in the Earth's atmosphere. This induces a burst of light, called Cherenkov radiation, emitted in a cone along the traveling direction of the charged particle. This burst of radiation can be detected on the ground. The emission mechanism of Cherenkov radiation, which is analogous to the production of a sonic boom by a jet traveling faster than the speed of sound in air, is outlined below.

2.2.1 Production Mechanism

When a charged particle travels in a dielectric medium, it polarizes the molecules of the medium and causes them to oscillate and hence radiate briefly when they return to their original state [71]. When the speed of the charged particle exceeds the phase velocity of light in the medium, this electromagnetic radiation interferes constructively and causes a coherent burst of radiation, called Cherenkov radiation, that is emitted in the forward direction of the charged particle (figure 2.3). The Cherenkov light is emitted within an emission angle, θ, given by the following formula [71]:

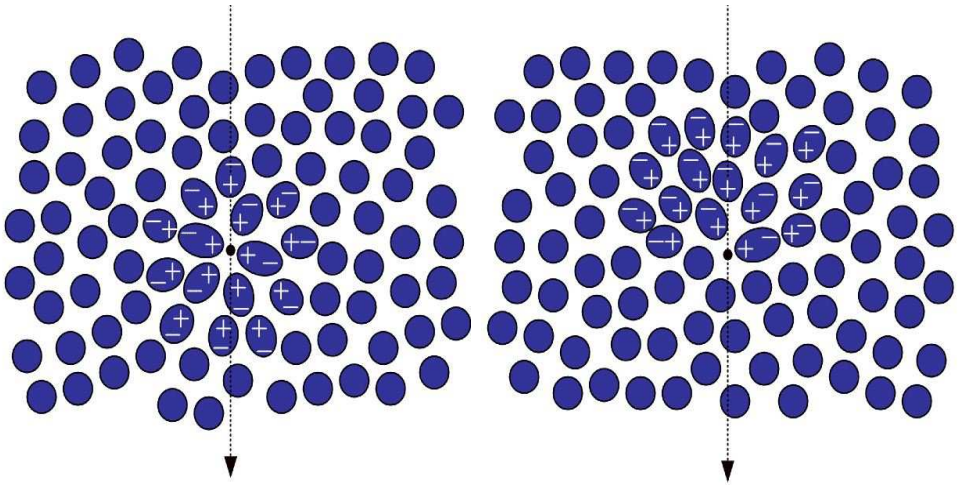

(a) Slow Moving particle. (b) Fast Moving particle.

Figure 2.3: This figure shows the polarization of a dielectric medium when a charged particle passes through it. Left: A slow moving charged particle produces a symmetric polarization which results in destructive interference of the radiation at large distance. Right: A fast relativistic charged particle polarizes the molecules asymmetrically, aligning the molecules into an effective dipole. The resulting radiation constructively interferes and Cherenkov radiation is emitted. Figure taken from [72].

$$\cos\theta = \frac{c}{nv} = \frac{1}{\beta n} \tag{2.1}$$

where n is the refractive index of the medium, v is the speed of the particle, c is the speed of light in vacuum and $\beta = \frac{v}{c}$. It is clear from Equation 2.1 that the condition for which Cherenkov radiation can occur is $\beta > \frac{1}{n}$. The same condition can be derived from the classical Huygens construction of wave superposition [74].

Substituting this condition into the energy expression for a particle, the minimum energy, E_{min} required for a particle to emit Cherenkov radiation is

$$E_{min} = \frac{m_0 c^2}{\sqrt{1 - n^{-2}}} \tag{2.2}$$

where m_0 is the rest mass of the particle, c is the speed of light in vacuum and n is the refractive index of the medium. The number of photons emitted per unit length, l, per unit wavelength, λ is given by the following formula [71]:

$$\frac{dN}{dld\lambda} = \frac{2\pi\alpha Z^2}{\lambda^2}\left(1 - \frac{1}{\beta^2 n^2(\lambda)}\right) \tag{2.3}$$

where Z is the charge of the particle in units of electron charge, α is the fine structure constant and the refractive index n is allowed to be wavelength dependent. The $\frac{1}{\lambda^2}$ dependence means that the majority of the photons are emitted in the UV region. However, higher energy photons are readily absorbed by the atmosphere and the result is that most of the Cherenkov photons lie in the blue region of the spectrum. The peak in the Cherenkov radiation that is transmitted to the ground is ~ 330 nm. The emitted and transmitted spectra of Cherenkov radiation are shown in figure 2.5.

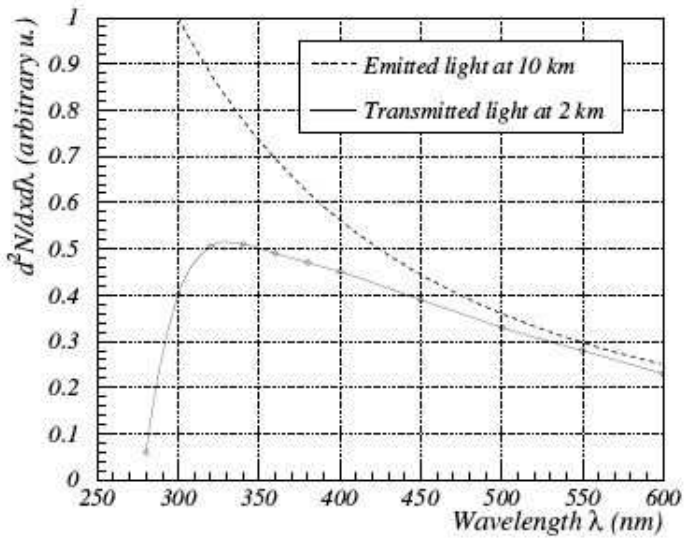

Figure 2.4: Cherenkov radiation emission spectrum and the transmitted spectrum after propagation through the atmosphere. The plot shows the number of photons emitted per unit length, per unit wavelength, versus the wavelength. Figure taken from [73].

2.3 Differences between Electromagnetic and Hadronic Showers

Due to the differences between the types of particles and physical processes involved in gamma-ray induced electromagnetic showers and cosmic-ray hadronic showers, the structure of these two types of air showers and their associated Cherenkov radiation have very different properties.

The radiation length for an electromagnetic shower is approximately 37.7 $\mathrm{g \cdot cm^{-2}}$ whereas the absorption length is approximately 80 $\mathrm{g \cdot cm^{-2}}$ for a hadronic shower. This means the hadronic shower can penetrate much deeper into the atmosphere and its shower maximum occurs closer to the ground than the electromagnetic shower maximum from the same energy primary. In a hadronic shower,

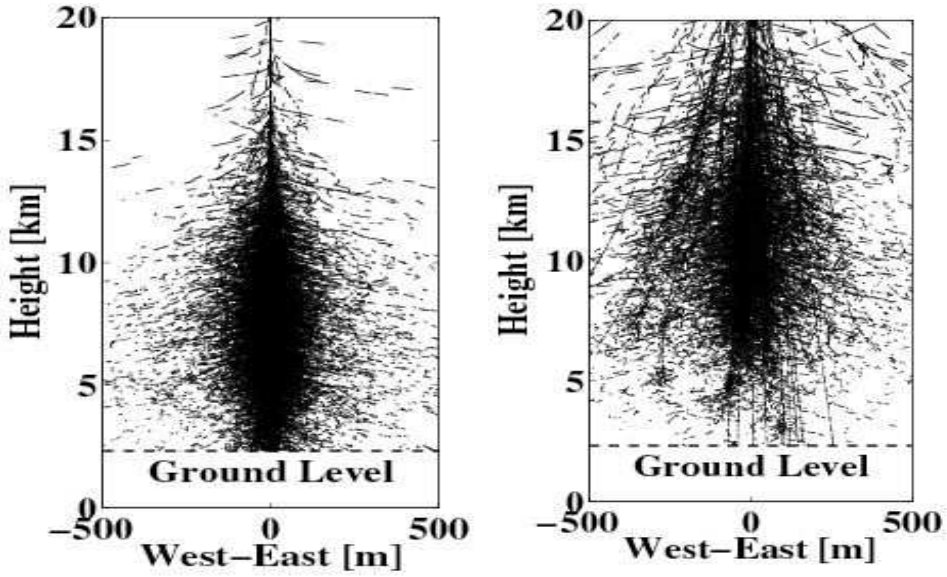

Figure 2.5: Monte Carlo simulations of the development of the air shower cascades. Left: Longitudinal view of the charged particles in an extensive air shower produced by a 1 TeV gamma ray. Right: Same information from an extensive air shower produced from by 1 TeV proton. The ground level is set to be the height of Mount Hopkins at 2320 m above sea level. Figures taken from [75].

a non-trivial fraction of the energy of the primary hadron is lost in the production of lighter muons. These particles are heavier than electrons and they have a relatively long lifetime which means that they can carry energy to the ground without producing much Cherenkov radiation. In an electromagnetic shower, the processes of pair production and bremsstrahlung mean that a significant fraction of the primary gamma-ray energy can be converted into Cherenkov radiation. As a result, the Cherenkov radiation from gamma-ray showers have higher intensity than those produced by cosmic-ray showers.

Since the emission angles of pair production and bremsstrahlung are small, the resulting gamma-ray shower is very compact and is bunched along the original

direction of the primary gamma ray. For the hadronic shower, the secondary particles produced from the strong interaction acquire transverse momentum which means the lateral extent of a hadronic shower is relatively bigger than that of a gamma-ray shower. The strong interaction produces many more hadrons in cosmic-ray showers, each of which can produce its own sub-shower. The complicated nature of the processes involved in cosmic-ray interactions means that cosmic rays produce multi-cored Cherenkov showers that are irregularly shaped and of non-uniform density. On the other hand, the simpler bremsstrahlung and pair production processes in a gamma-ray shower means the initial energy of the primary gamma ray is evenly distributed among all secondary particles, and the resulting Cherenkov light pool is therefore circular and is evenly and uniformly distributed around the shower core. Figure 2.6 shows the simulated profile of the charged particles produced in both gamma-ray and cosmic-ray air showers. Figure 2.7 shows a simulation of the Cherenkov photon distribution on the ground from the two types of showers.

2.4 Imaging Atmospheric Cherenkov Technique

The application of Cherenkov radiation detection to gamma-ray astronomy was proposed back in 1963 by Jelley and Porter [77] but it was not until 1989 that the first VHE gamma-ray source was firmly established by the pioneering imaging atmospheric Cherenkov telescope (IACT), the 10 meter Whipple telescope located in southern Arizona. After the success of Whipple, other experiments have sprung up around the globe, for example the CANGAROO experiment in Australia [25] and the HEGRA experiment on the Canary Islands [18]. The HEGRA experiment was also the first to introduce the stereoscopic technique, where Cherenkov shower images are taken simultaneously by multiple telescopes.

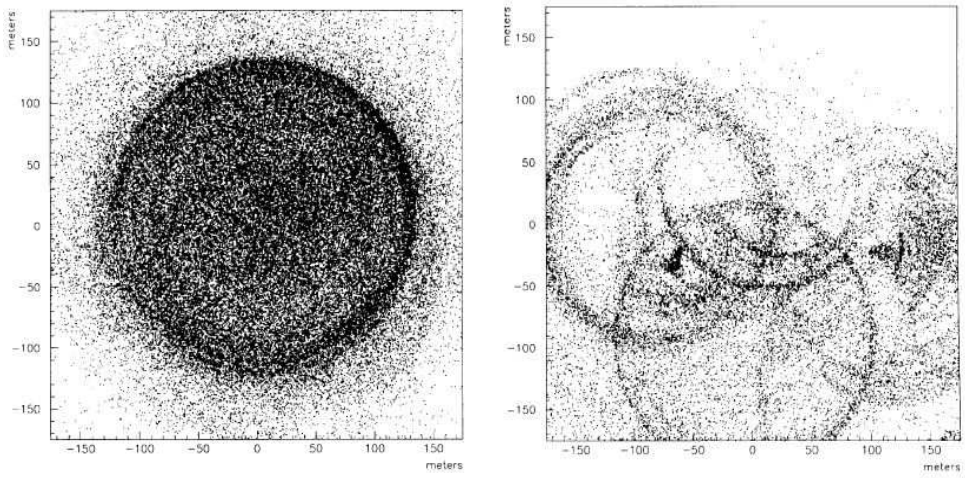

Figure 2.6: Monte Carlo simulations of the lateral distribution of Cherenkov light at an observation depth of 830 g·cm^2. Left: Arrival positions of all the Cherenkov photons from an extensive air shower initiated by a 50 GeV gamma-ray primary. Right: Same distribution from an extensive air shower initiated from a 200 GeV proton. Figures taken from [76].

In the 2000's, a new generation of IACTs came into operation in different parts of the world. These new IACTs all employ the stereoscopic technique and have much improved sensitivity and energy threshold over the previous instruments. The new generation of IACTs includes the VERITAS experiment in the U.S. [78], HESS in Namibia [23], MAGIC I and II on the Canary Islands [24] and CANGAROO III [25] in Australia. In this chapter, the principle behind the IACT will be presented.

2.4.1 Cherenkov Telescope

The idea behind IACTs is simple. Just take a picture of the Cherenkov shower with a high resolution camera. However since the Cherenkov radiation is extremely faint and the burst lasts only a few nanoseconds, many technical chal-

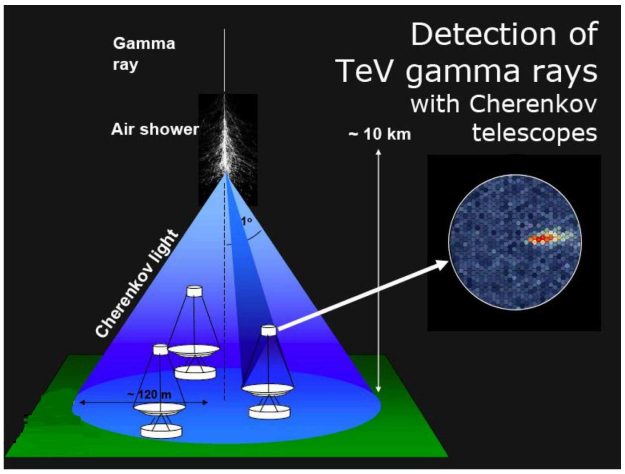

Figure 2.7: The figure shows an gamma-ray initiated air shower and the Cherenkov light pool. The Cherenkov light pool has a diameter of approximately 120 m. A Cherenkov telescope array can observe the air shower anywhere within the light pool. The image of the air shower taken from a camera is shown on the right-hand side.

lenges must be overcome before detection is possible. An outline of the features required by an IACT is discussed briefly here.

One of the advantages of ground based IACTs over satellite gamma-ray experiments is its large collection area. The Cherenkov light pool covers an area of approximately 50,000 m^2, and a Cherenkov telescope or array can lie anywhere within the light pool in order to observe the Cherenkov radiation (figure 2.8). However, since not all Cherenkov photons reach sea level due to Rayleigh and Mie scattering and ozone absorption, the performance of an IACT improves at higher altitude.

Due to the low brightness of the atmospheric Cherenkov radiation, a large reflector is advantageous in collecting and reflecting photons onto the camera. Instead of a big single mirror, modern reflectors of IACTs are made of many

smaller mirror facets. This has the advantage of significant cost reduction in the construction and transportation of the mirror; smaller mirrors are also easier to maintain and can be replaced if needed.

The most important part of a telescope is its camera. With the invention of the photomultiplier tube (PMT), Cherenkov radiation detection became possible. In fact, it was not until the invention of PMTs that the first successful detection of Cherenkov radiation from extensive air showers was made in 1953 [13]. PMTs have a bi-alkali photo-cathode which is sensitive to the UV and blue band of the optical spectrum which is exactly where the peak of the Cherenkov burst is located, as discussed previously. By using a large number of PMTs in the camera, a high angular resolution can be achieved. The angular extent of the air shower is approximately 1° across and hence the field of view of an IACT should be large enough to contain the entire air shower.

The duration of a Cherenkov burst is on the order of a few nanoseconds, so in order to pick out this signal from the night sky background photons, the response time of the detector must be comparable. With the advances in high speed electronics, reliable detection of Cherenkov radiation has become relatively straightforward.

All current generation of VHE gamma-ray experiments are designed as multi-telescope array systems. The use of multiple telescopes to image the Cherenkov burst has many advantages over a single IACT. An array has a better angular resolution, a lower energy threshold and much improved sensitivity.

A more detailed description of the technical aspects outlined in this section will be presented in chapter 3, specifically in the context of the VERITAS experiment.

2.4.2 Imaging Technique

Cherenkov images taken from gamma-ray showers and cosmic-ray showers have different properties as explained earlier. The discrimination technique used to identify gamma-ray events from the background cosmic ray events exploit the intrinsic differences between these two types of showers.

The first major difference is the reconstructed source positions of the images; the cosmic-ray background is isotropic and hence the arrival directions should be uniformly distributed across the camera. Gamma-ray events, on the other hand, tend to point back to the source position of the primary gamma ray, and, therefore, the reconstructed source positions of gamma-ray events should accumulate at the source position. The second major difference is the geometry of the images themselves. Cosmic-ray events tend to be wider and shorter due to the way hadronic showers develop in the atmosphere. Similarly gamma-ray events tend to be compact, narrow and elongated towards the arrival direction (figure 2.9). Hillas [76] was the first to propose a set of parameters, called Hillas parameters, to characterize Cherenkov images. The parameters are calculated from the moments of the light distribution in the image. They characterize the geometry of the image in terms of its size, width, length and orientation.

Originally, simulations were heavily used to identify the regions of the parameter phase space where the gamma-ray and cosmic-ray events are likely to be located in order to develop a set of event selection criteria (called cut values). However after the detection of the Crab Nebula, real data on the Crab are used instead to tune up the cut values. This method has been shown to be very effective, this technique can reject 99.99% of background showers while retaining more than 30% of gamma-ray events [76].

A more detailed description of the analysis technique and the background

discrimination method will be presented in Chapter 4.

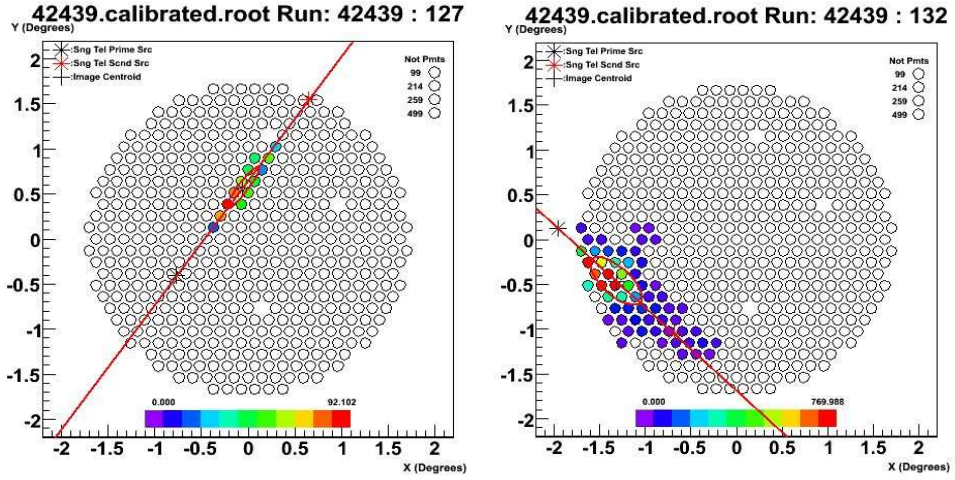

(a) Gamma-ray Event (b) Cosmic-ray Event

Figure 2.8: Left: Image of gamma-ray-like event. Right: Image of a cosmic-ray-like event. Both images are recorded with a single VERITAS camera. Each circle represents an individual PMT. The color scale denotes the intensity of light detected in the individual PMT. The lines are extended from the semi-major axis of the parametrized images. The intrinsic geometrical differences between the two types of images are evident from the figures.

CHAPTER 3

The VERITAS Experiment

The VERITAS experiment consists of four 12-meter diameter imaging atmospheric Cherenkov telescopes, located at the Fred Lawrence Whipple Observatory at elevation 1270 meters on Mount Hopkins in southern Arizona, USA. The telescope design is based on the very successful 10-meter Whipple Cherenkov telescope but with significant improvements in all the hardware components and a with larger field of view. The complete 4-telescope array began full scientific observations in September 2007.

Individual telescopes are identified by telescope ID: T1, T2, T3 and T4, with the numerical values representing the chronological order in which each telescope was constructed. The locations of the telescopes form the vertices of an irregular quadrilateral with distances of each side being 85, 35, 85 and 109 meters (figure 3.1). A detailed description of the telescope structure, hardware and electronic components are given in this chapter.

I worked on the data archiving system for the VERITAS collaboration. I have developed the software that is used to transfer $\sim$ 100 GB of data per night to UCLA and on scripts and other utilities to distribute data to memebers of the collaboration. I also played the role of a system administrator for the archive, to ensure smooth day to day operations of the system from 2006-2009.

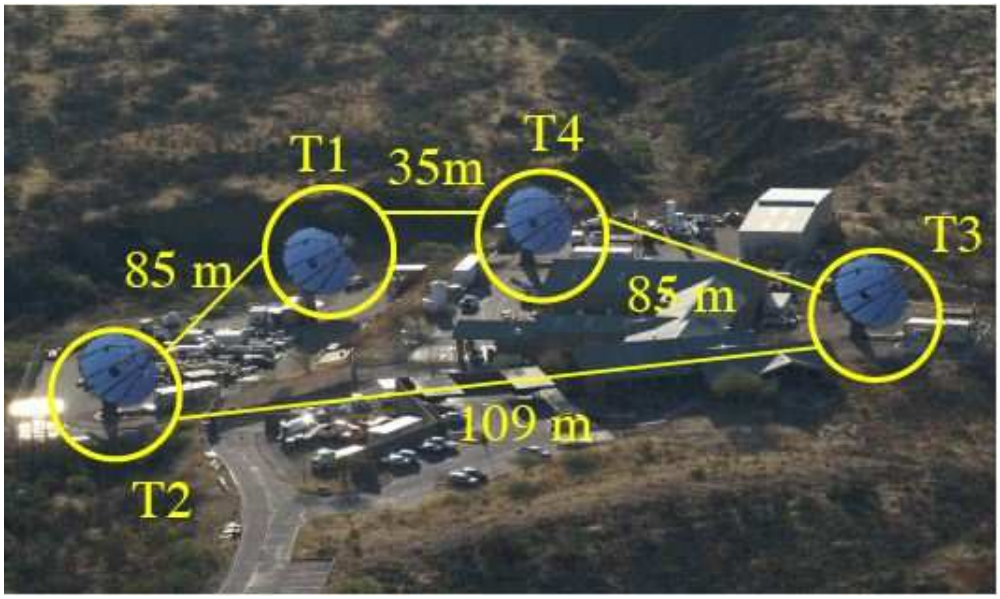

Figure 3.1: An aerial photo of the VERITAS array showing the positions and the distances between each telescope.

3.1 Telescope Structure

Each telescope consists of a tubular steel space-frame optical supporting structure (OSS) attached to an altitude-azimuth positioner. The diameter, D, of the OSS is 12 m and 350 hexagonal shaped spherical facet mirror are mounted on it to form a reflector with focal length, F, of 12 m. Four steel arm structures extend out from the OSS forming a quadrapod to hold the 499-pixel camera at the focal point. The weight of the camera is balanced by a counterweight attached behind the OSS (figure 3.3).

3.1.1 Optical Support Structure

The OSS is based on the Davies-Cotton (DC) [26] telescope design which uses a large number of small identical spherical mirror facets instead of a single giant

spherical reflector (figure 3.2). This reduces the cost of construction and maintenance since smaller mirrors can be easily fabricated and replaced, if needed. The main drawback of the Davies-Cotton design is its non-isochronous nature, i.e. due to the configuration of the mirror, a planar wavefront arriving perpendicular to the axis of the reflector will reflect and reach the focus with a spread in the arrival times. However, simulation studies [79] have shown that 90% of the Cherenkov light reflected off the reflector arrives at the camera within 2 ns, which is within the digitization time scale of the FADC (section 3.4.1), and hence the arrival time spread does not significantly impact the performance of the experiment.

The combined weight of the camera, mirrors, counterweight and the OSS itself causes varying level of flexure depending on the elevation of the observation target. The flexure causes a widening in the point spread function (PSF) of the telescope, defined as the width of a Gaussian fit to a bright star image, leading to a "blurring" of the image. Another problem due to the flexure is the mismatch of the observing target and the center of the field of view. These optical distortions can be corrected by applying mirror alignment and tracking corrections (section 3.1.4).

3.1.2 Positioner

The OSS is mounted on an altitude-azimuth positioner (figure 3.2). The positioner has a maximum slewing speed of $1^{\circ}/s$ moving in either the altitudinal or azimuthal direction, but for safety reasons, the maximum slew speed is set to 0.5°/s. The tracking error is less than 0.01°. The positioner is controlled by custom built software on the tracking computer through an Ethernet interface. The positioner is designed to operate safely at wind speeds up to 20 MPH and can withstand wind speeds up to 100 MPH when the telescope is parked and in

Figure 3.2: Picture of an OSS before it was mounted on to a positioner.

locked mode.

3.1.3 Mirrors

Each mirror facet is hexagonally shaped and has an area of 0.333 m^2. Each telescope is equipped with 345 mirrors arranged in such a way that they form a spherical surface of 12 m radius. The total mirror area is approximately 110 m^2. The hexagonal design allows close packing on the OSS in order to maximize the total mirror area (figure 3.5).

Once the mirrors are delivered by the manufacturer to the Whipple Observatory, they are cleaned and then placed in a vacuum chamber at 10^{-4} atm. An aluminum layer coating is applied to each mirror until a thickness of approximately 135 nm is achieved. Finally, anodization is done by passing a current through the alumimun to produce aluminum oxide which adjusts the peak reflectivity of the mirror to coincide with the peak of the Cherenkov light spectrum. Anodizing the mirrors also increases their durability.

Figure 3.3: A photo of an OSS and its positioner.

For quality control purposes, each mirror is carefully tested to ensure that the the radius of curvature is within $24\text{m} \pm 1\%$. The reflectivity of the mirrors has been measured to exceed 90% at 320 nm and to exceed 85% between 280 and 350 nm [80]. Note that the reflectivity of the mirrors changes $\sim 3\%$/year due to the impact of the environment and they are recoated every year to maintain a steady performance level.

3.1.4 Mirror Alignment and Optical Corrections

Proper mirror alignment is essential to ensure that the reflector achieves the optimal PSF and pointing accuracy. The Davies-Cotton design has the characteristics that light originating from the center of a sphere, at twice the distance ($2F$ point) of the focal length, will be reflected directly back to the center. By using this property, a helium-neon laser is fired from the $2F$ point to each mirror facet and the mirror is adjusted until the return laser beam coincides with the outgoing beam.

The widening of the PSF due to the OSS flexure is corrected for by using the bias alignment technique. The mirrors are deliberately mis-aligned in the stow position in such a way that when the OSS is moved to a different elevation, the flexure will cause the mirrors to return to their properly aligned positions [81].

The mismatch of the observing target and the center of the field of view is corrected for by using tracking corrections. A list of known bright stars at different elevation and azimuthal angles is chosen. Then the telescopes are pointed to each star and the offsets from the center of the field of view are recorded by the tracking program. These corrections are subsequently applied by the tracking program during normal observations.

Figure 3.4: A front view of the T2 reflector. The reflector is made by close packing the 345 small hexagonal mirrors.

3.2 Camera

Each telescope is equipped with a 499-pixel camera made of photomultiplier tubes (PMTs) and has a total field of view of 3.5° (figure 3.5). The camera is housed inside a light-tight, waterproof focus box 12 m away from the OSS at the focal point of the reflector. The focus box has a shutter that can be operated by a remote control. The shutter is closed during the day to protect the PMTs from UV exposure and is only opened during observations.

The focus box also hosts other important electronic components, including the preamplifiers, the current monitor boards and charge injection (QI) boards. The PMTs are powered by a high voltage (HV) system; the voltage to each PMT can be controlled individually.

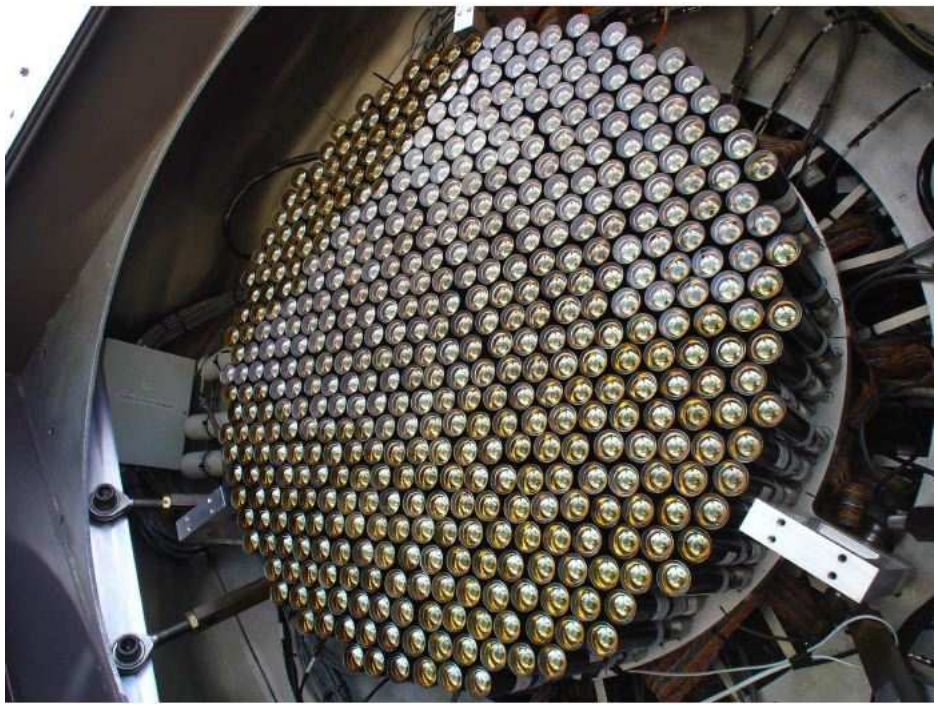

Figure 3.5: A photo of the 499-pixel camera of T1 with the lightcone plate removed.

3.2.1 Lightcone

Since the light sensitive area of a PMT is actually smaller than its cross-sectional area and space exists between the PMTs, a significant amount of light reflected on the camera is not collected. To increase the amount of collected light, a lightcone plate is mounted onto the camera to act as a light concentrator (figure 3.6). Each PMT is covered with a hexagonal cone that leads to an opening on top of the light sensitive area of the PMT. The lightcone is coated with an aluminum layer that gives a reflectivity above 260 nm of more than 85%. Light hitting the cones will be reflected along the inner surface down to the opening onto the PMT. The lightcone increases the collection efficiency of the camera from 55% to 75%. In addition to increasing the camera collection efficiency, the lightcones also reduce the acceptance angle of the PMT and thus reduce the amount of night sky background light reaching the PMT [83].

3.2.2 Photomultiplier Tubes

The basic structure of a PMT consists of a photo-cathode, followed by a series of dynodes at increasing potential, and an anode. When a photon of sufficient energy hits the photo-cathode in the front of the PMT, an electron (referred to as a photoelectron) is released from the metal surface due to the photoelectric effect. The ejected electron is accelerated by the potential difference within the PMT until it strikes the first dynode which is coated with a secondary emissive material that releases more electrons. These newly released electrons will then strike the second dynode releasing more electrons, resulting in an electron cascade when more dynodes are hit. All the electrons released from the dynodes are collected at the anode inducing a current which is then recorded. The gain of a PMT is the average number of electrons produced from a single photoelectron. The average

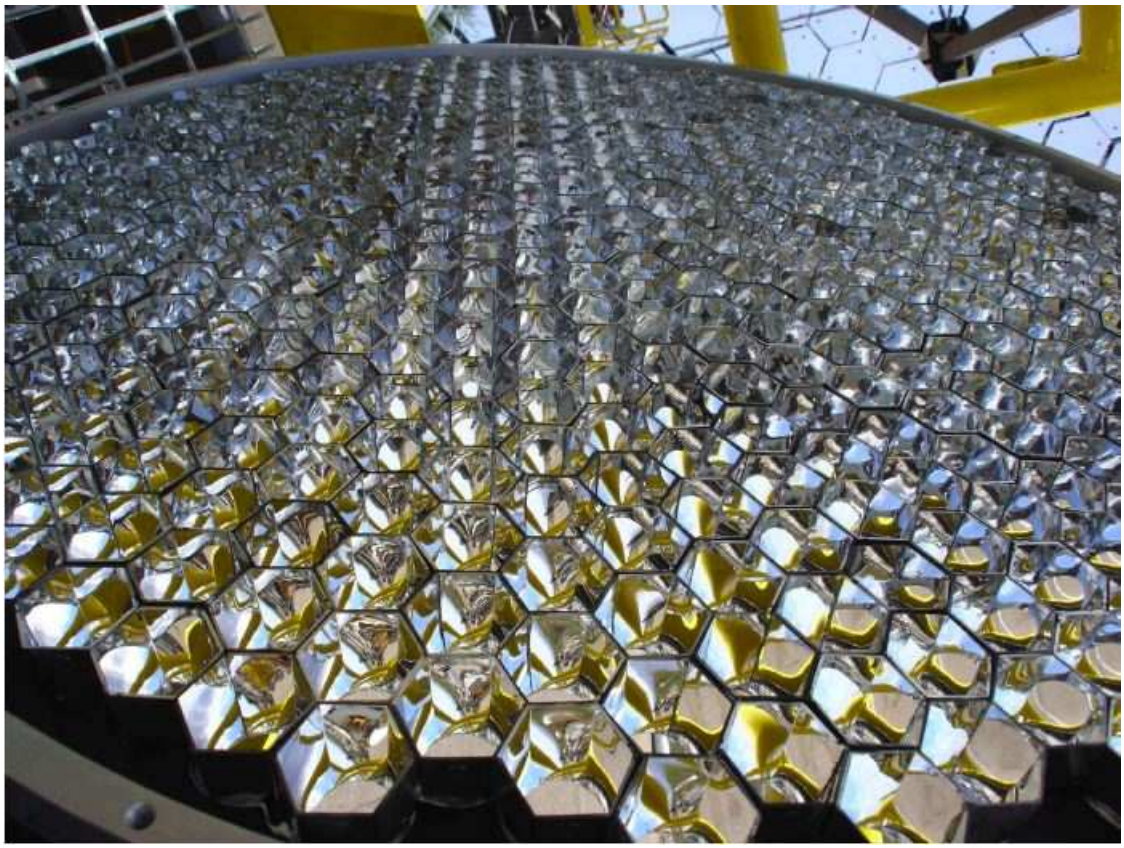

Figure 3.6: Picture of a lightcone lying on the platform of T3.

gain of the PMTs used in VERITAS is 2×10^5.

An important characteristics of a PMT is its quantum efficiency (QE), which is the probability of releasing a photoelectron when the photo-cathode is struck by a photon. The QE depends on the wavelength of the incoming photon and also on the photocathode material. The PMTs used in VERITAS are chosen so that they have the maximum QE in the regime relevant to Cherenkov showers (300 nm). The QE curve for the PMTs used in VERITAS is shown in figure 3.7.

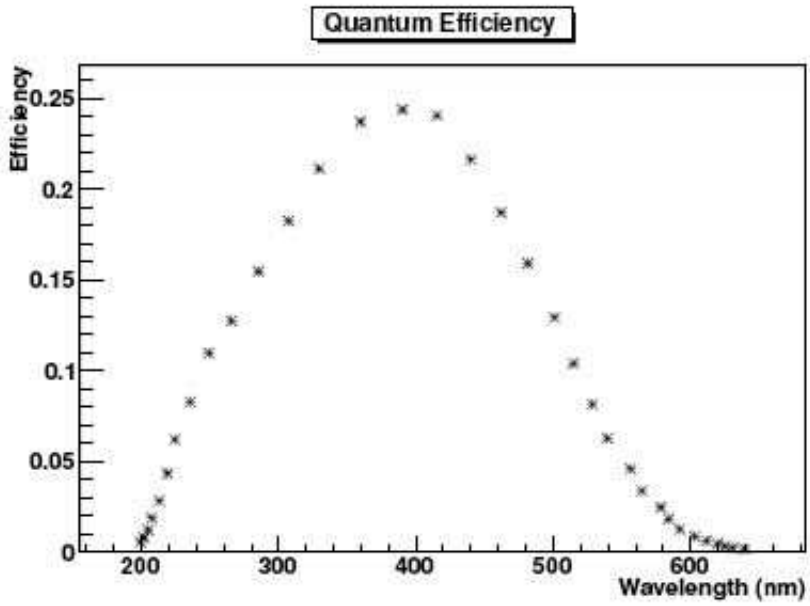

Figure 3.7: A plot of the quantum efficiency versus wavelength for the PMTs used in VERITAS. Figure taken from [82].

3.2.3 High Voltage

The high voltage (HV) supply to each telescope is provided by two multi-channel HV crates. The PMTs in the camera are divided into sectors where each sector consists of eight PMTs and every six sectors constitute a module. Furthermore,

when the power is switched on, the voltage of each individual PMT (channel) in the camera can be adjusted independently. Each channel has a maximum allowed current and voltage of 1 mA and 1500 V, respectively. The HV also allows accurate voltage setting to within ±1 V.

The HV supply to each PMT is controlled through the graphical user interface of a custom built HV program. A predetermined set of voltages is applied to the PMTs when the program is executed but these values can be changed manually by the user, if needed. Auto-suppression of channels is built into the HV program to ensure that the currents do not exceed the safety limit; this can occur when a very bright star or stray background light falls on to the field of view which then induces a rapid rise in current in the affected channel. The HV program also automatically logs the voltage of each channel every minute into the database; these data are used for data analysis and also for the diagnosis of any PMT problem which might occur during observations.

3.2.4 Preamplifier

The base of each PMT is equipped with a preamplifier which amplifies the electrical signal registered at the anode. The input range of the data acquisition system (DAQ) (section 3.4) is between 0 to -1.6 V, and there is a 25% attenuation factor when the signal is transmitted from the preamplifier to the DAQ over a 50 m long cable. Thus the preamplifier output signal is in the range between 0 and -2.2 V.

3.2.5 Current Monitor and Environment Sensors

To ensure that the PMTs are operating below the maximum allowed current level, each camera is equipped with two current monitoring systems (CMS). The

anode current of each PMT is proportional to the number of photons hitting the photo-cathode. The fluctuation of the night sky background (NSB) and starlight can cause a rapid increase in the level of the anode current in the PMTs. The current monitor reports the anode current level to the observer and also to the HV program which will suppress any PMTs (channels) that have abnormally high current levels. The current monitoring system used in VERITAS has a 10 Hz readout capability and is accurate to within 0.1 μA.

Beside its main duty of monitoring the anode current, the CMS also provide power to the preamplifiers and are connected to other environment sensors that provide important information on the observing conditions. The environment sensors employed are temperature and humidity sensors inside the camera focus box; these two environment variables are important indicators of whether the camera is operating under normal conditions.

3.2.6 Charge Injection System

The charge injection (QI) system is integrated within the camera and it can send signals directly into the bases of the PMTs. These signals can be programmed to mimic Cherenkov induced signals in the PMTs and hence the QI system is a vital tool for testing and calibrating the instrument. The main component of the QI system is a programmable pulse generator (PPG) which can produce pulses of variable frequencies from 1 Hz to 1 MHz, pulse widths from 1 ns to 10 ms and a maximum amplitude of 5 V. Unfortunately, the QI system is not as reliable as it needs to be and it is not used for detailed studies of the cameras and the electronics.

3.3 Trigger System

Since any data acquisition system has only a finite readout rate, a real-time background rejection system is needed to keep the data rate manageable. VERITAS uses a three-level trigger system to efficiently select Cherenkov shower events. The level 1 (L1) trigger is an individual pixel level trigger system, level 2 (L2) is a camera level pattern selection trigger system and level 3 (L3) is an array level event trigger system [84].

3.3.1 Level 1 Trigger

The L1 trigger is a pixel-level system which essentially triggers when the signal from a PMT exceeds a certain pre-programmed threshold. However, since the precise timing information of the trigger is an important input to the level 2 trigger, a more sophisticated system, the constant fraction discriminator (CFD) [85] is used instead of a simple threshold trigger. When a signal pulse from the PMT is sent into L1, it is split into three copies. The first copy enters a simple threshold discriminator which outputs a trigger signal when the incoming pulse exceeds a predetermined level. One of the other two copies is attenuated by some factor and the other one is inverted and delayed. Both of these copies are then sent into a zero crossing discriminator (ZCD) where the two pulses are added. The trigger time of the L1 trigger is defined as the point when the two pulses sum to zero (figure 3.8).

The ZCD can suffer from timing jitter due to fluctuation of the night sky background (NSB) and electronic noise within the ZCD. An offset can be applied to the ZCD to reduce the timing jitter by preventing small fluctuations from triggering. Since the optimum level of offset to be applied to the ZCD depends

on the variable NSB and noise level, a circuit called a rate feed-back (RFB) loop was employed. The RFB can adjust the level of offset to be applied to the ZCD depending on the level of NSB, i.e. when the NSB is high, the offset to be applied is automatically increased by the RFB and vice versa. The RFB can respond to changes in the noise within 1 s and was found to reduce the timing jitter by 10% near the threshold [85].

3.3.2 Level 2 Trigger

The L2 trigger (also called the pattern selection trigger (PST)) is a camera level pattern trigger which is based on the principle that gamma-ray initiated Cherenkov showers should produce compact images in the camera. Thus a few adjacent pixels should trigger at about the same time for a gamma-ray event, whereas NSB should trigger random pixels [87].

The PST takes the signals from the inner 463 pixels of the camera (the outermost pixels do not participate) and divides these into 19 overlapping patches of 59 pixels each via a signal splitter. These signals are then fed into 19 pattern selection modules programmed to recognize patterns that have been preloaded into the module memory. If a group of signals matches one of the pre-stored patterns, a L2 trigger signal is sent to the level 3 trigger system.

Ideally one would like to set the CFD threshold as low as possible to decrease the array energy threshold. The suitable CFD level can be found by recording the L2 rate at different CFD levels. As the CFD threshold is decreased the L2 rate increases steadily until a point where the L2 rate jumps up significantly. This is the point when the L2 is dominated by NSB. The CFD threshold is chosen as low as possible, but away from the NSB region (figure 3.9).

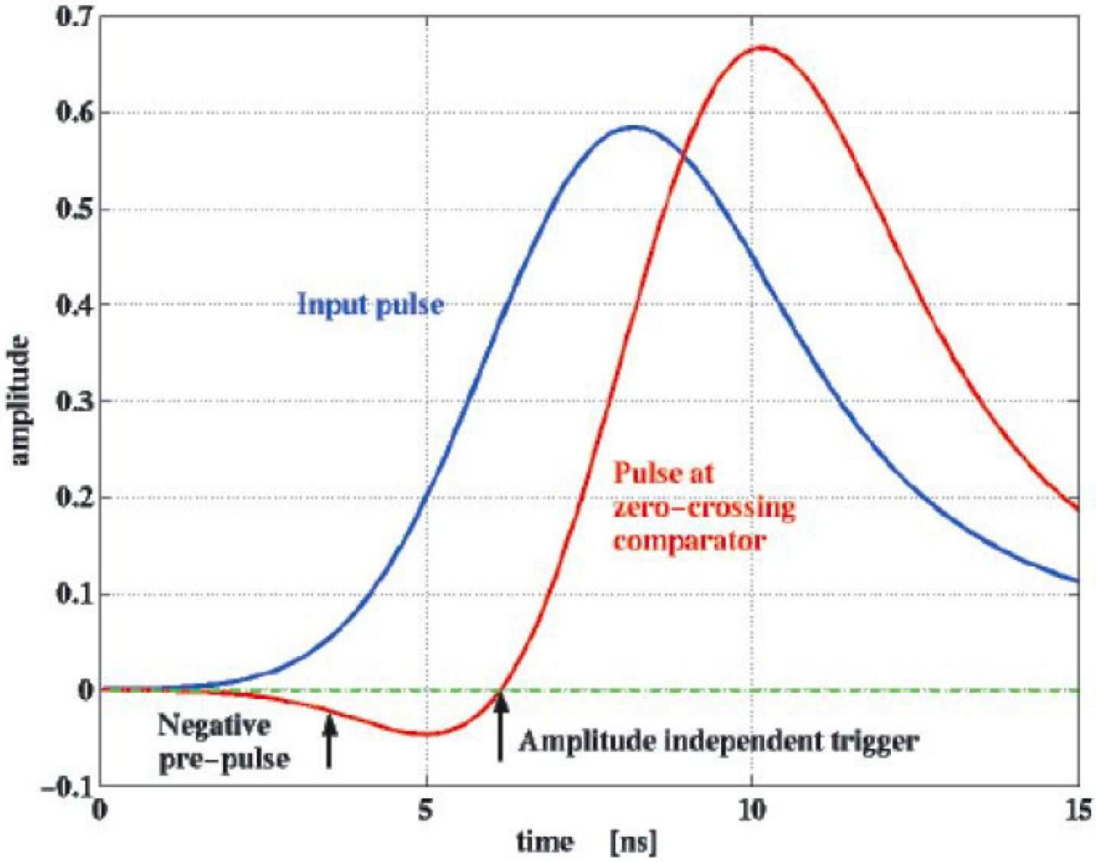

Figure 3.8: Figure showing the working principle of the CFD. An input pulse is attenuated and added to an inverted and delayed copy of itself. This results in a pulse that has a positive and negative part and the trigger time is defined to be the zero-crossing point of the new pulse. The blue curve shows an input pulse and the red curve shows a magnified summed pulse. The arrow indicates the location of the amplitude independent trigger time. Figure taken from [86].

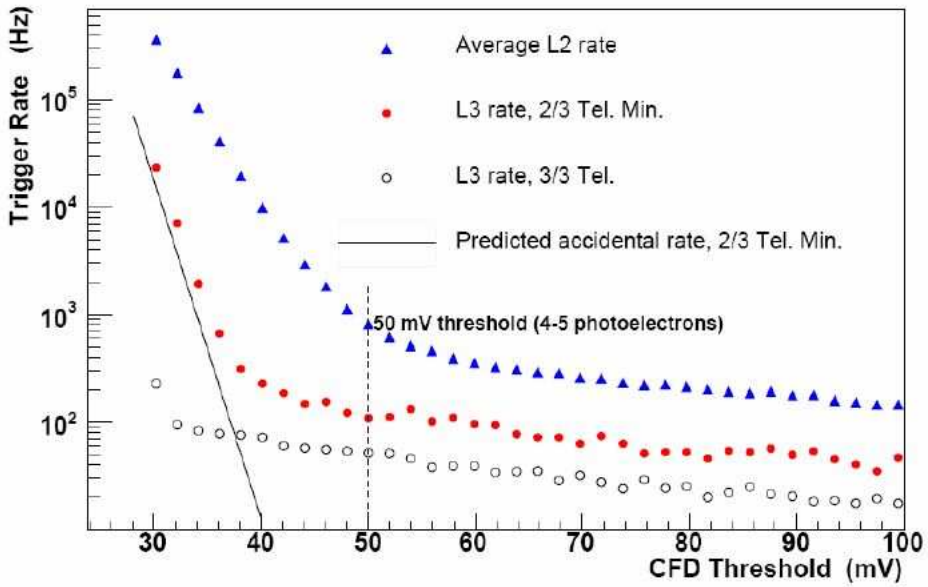

Figure 3.9: The 3-telescope configuration bias curves for the L2 and L3 rates. The bias curve was taken with a 50 ns coincidence window and the array was pointing to a dark patch of the sky near zenith. The triangles show the average L2 rate of the array versus different CFD thresholds. The red dots represent the average L3 rate versus different CFD thresholds in the configuration where two out of three telescopes participate in the L3 trigger. The open dots represent the average L3 rate versus different CFD thresholds in the configuration where three out of three telescopes participates in the L3 trigger. The rapid increase in the trigger rate at low values of the CFD threshold is due to the onset of the NSB. The trigger rate above the CFD threshold is largely due to cosmic-ray events. The CFD threshold, as indicated by the dashed vertical line, is chosen to be well above the NSB. Figure taken from [84].

3.3.3 Level 3 Trigger

The L1 and L2 triggers are very efficient in rejecting the random fluctuations of the night sky background (NSB), but they are unable to distinguish local muons from gamma-ray showers since muons often produce images on the camera that are identical to images from gamma-ray initiated showers. One of the main advantages of a multi-telescope array system is that it can efficiently reject the muon background since the ring-shaped images from muons are only big enough to cover the area of one telescope. The L3 trigger system exploits this property of the muon rings by requiring that L2 signals from two or more telescopes arrive within a coincidence window which is typically between 40-100 ns.

When L2 signals are sent from each telescope to the L3 system, appropriate time delays are applied to the L2 signals in order to equalize the time required by the L2 signals to travel through different cable lengths. Furthermore since the Cherenkov shower wavefront does not hit each camera at the same time, shower time delays are applied to compensate. The L3 then looks for the coincidence of time-corrected L2 signals from two or more telescopes within the coincidence window, currently set at 100 ns, and it sends a L3 signal to the data acquisition system when such a coincidence is found. The 100 ns coincidence window is a conservative estimate in order to allow for electronic jitter and different geometric shapes of the Cherenkov shower; it has been shown that the L3 rate remains stable even when the coincidence window is reduced to 25 ns [84].

In addition to efficiently rejecting muon background, the L3 also suppresses NSB triggers further, thus reducing the minimum CFD threshold. The L3 system has led to a reduction of energy threshold and an improved background rejection which substantially increase the array's sensitivity.

3.4 Data Acquisition System

The VERITAS data acquisition (DAQ) system has a similar structure to the trigger system: a pixel-level DAQ, a telescope-level DAQ and an array-level DAQ. When the L3 triggers, a signal is sent to each telescope to halt the digitization of the PMT signals and to begin readout from the FADC boards (section 3.4.1). This process is controlled by the VME data acquisition system (section 3.4.2). The readout from the FADC boards is then processed by the event builder (section 3.4.3) to form a telescope-level data. Finally, the harvester (section 3.4.4) collects all these data and merges them into an array-level event [88].

3.4.1 FADC Boards

The DAQ for each telescope is comprised of 50 custom built flash analog-digital converter (FADC) boards distributed in four VME (virtual machine environment) crates. The PMT signal are connected directly to the front end of the FADC Boards. The PMT output signals are split into two copies, one copy is continuously being digitized by the FADC boards at a 500 MS/s rate into a circular memory which has a depth of 64 ns, and the other copy is sent to the L1 trigger. When a L3 signal arrives, the digitization stops and 24 samples, where each sample has a width of 2 ns, and 48 ns of data are read out from the FADCs.

The FADCs have an 8-bit dynamic range which corresponds to 0-255 digital counts. This dynamic range is further extended by a HiLo gain switch. When the signal exceeds the default dynamic range, an alternate copy of the signal which was delayed and passed through a different channel with lower gain is digitized instead and a scaled digitized bit is tagged after the truncated saturated sample so that it can be analyzed appropriately later. This process extends the dynamic

range of the FADCs to about 1500 digital counts.

3.4.2 VME Data Acquisition

The VME data acquisition (VDAQ) program initializes the various configuration parameters for the FADCs and the CFDs, such as the CFD threshold, the FADC look-back time and the buffer of the FADC to be read out. Once the initialization is complete, VDAQ begins waiting for a readout instruction from L3.

When a L3 signal is received, VDAQ begins readout and during that time, the system will not accept any further L3 triggers. The FADCs read out the appropriate portion of the circular memory by chain block transfer (CBLT), a procedure designed to handle data distributed over different FADC boards in the VME crate, and store it in the VDAQ buffer until it is sent to the event builder. When the CBLT is completed, VDAQ is ready to receive the next L3 trigger. VDAQ also encodes the unique event number and the trigger type it received into the event fragments from each crate. This additional information is needed by the event builder to synchronize the data fragments.

3.4.3 Event Builder

The event builder is responsible for collecting data fragments from the VME crates via VDAQ to form telescope level data event. The event builder is connected to VDAQ with a 50 Mb/s scalable coherent interface (SCI), a high speed computer bus, and it continuously checks for new data buffers in VDAQ. When the data fragments from VME crates are received from VDAQ, the event builder merges the data fragments that have the same event number together to produce a telescope level data event. These events are buffered in memory until approximately 160 kb of telescope data are accumulated, at which point one copy is

written to the local disk and the other copy is sent to the harvester via a gigabit Ethernet connection.

3.4.4 Harvester

The harvester program collects telescope level data sent from the event builders in each telescope and integrates them into an array-level data event. The final data product is written to disk in a custom built format called the VERITAS bank format (VBF). VBF contains all the telescope events and all trigger information indexed by the event number. The harvester also compresses the data using a custom designed algorithm for VBF. A typical compressed VBF data file for 20 mins of full array data is approximately 5 Gb in size. A schematic outlining the trigger and data acquisition processes is shown figure 3.10.

3.5 Observing Strategy

Since the Cherenkov shower is very faint, it is necessary to minimize the influence of NSB and, therefore, the ideal observation conditions are clear moonless nights. With its increased sensitivity and sophisticated trigger system, VERITAS has been able to take some data under moonlight, typically when the moon is less than half-full and at least 90° from the field of view. This has greatly increased the amount of available observing time as compared to what was achieved with the previous generation of Cherenkov telescopes.

There are two main observing modes employed in VERITAS, the wobble mode (section 4.6.1) and survey mode (section 4.6.2), and usually data are taken in a 20 min long session. Most of the data are taken under wobble mode since it has the advantage that the background level can be estimated from the same data

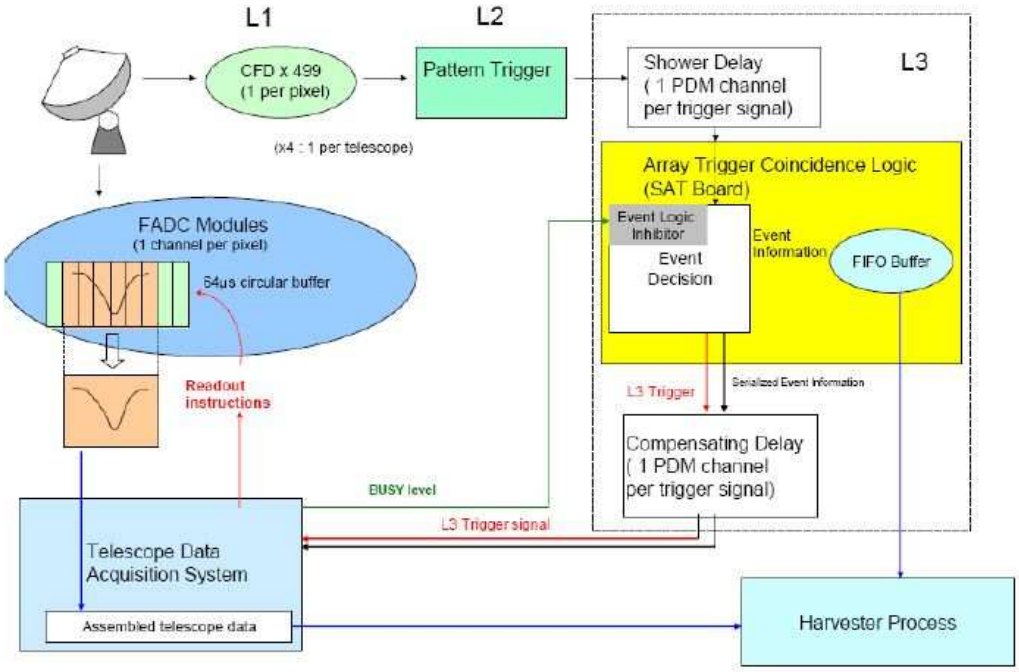

Figure 3.10: The flow chart shows triggering and data acquisition processes in VERITAS. The details of these processes are summarized in the text. Figure taken from [84].

run (see chapter 4 for more details on data analysis techniques), but for this dissertation work, the data were taken in survey mode which is more suitable for survey style investigation.

3.5.1 Wobble Mode

In wobble mode observation, the telescopes are pointed in such a way that the target is offset slightly from the center of the field of view. The size of the offset is usually 0.5° for a point-like source, since at this distance the collection efficiency of the array is not much degraded from the collection efficiency in the center of the field of view. However, if the target is known to be extended in size, a bigger offset is required to ensure that there will be no source photon contamination during the background estimation in the analysis stage (see chapter 4). To avoid any bias that may be introduced in a particular direction of the offset, wobble runs of the same offset distance but different directions, north/south/east/west, are taken.

3.5.2 Survey Mode

In survey mode observations, the center of the field of view is pointed to the target and it is tracked for the entire duration of the run. In the previous generation of instruments, data taken under the survey mode was called an ON run and a corresponding OFF run, which was also taken under the survey mode but pointed to a different patch of sky, had to be taken for background estimation [89]. With the increase sensitivity of the new generation of instruments like VERITAS, the OFF runs are no longer needed. This effectively increases for amount of available observation time since no dedicated time is needed to take the background OFF runs.

CHAPTER 4

Data Analysis

The VERITAS collaboration has developed several analysis packages to analyze the VHE gamma-ray data. Even though the implementations of the analysis algorithms vary among different packages, they share more or less the same sequence of steps in the analysis chain. The analysis procedure consists of the cleaning and calibration of the data (section 4.1), telescope level camera image reconstruction (section 4.2), shower reconstruction (section 4.3), event selection (section 4.4), background estimation and result extraction (section 4.5). All analysis results in this dissertation were produced using the official VERITAS analysis package, the VEritas Gamma-ray Analysis Suite, VEGAS. VEGAS is a highly customizable modular analysis package that was built on top of ROOT, CERN's open source data analysis framework [90]. The stages, or modules, of VEGAS correspond to the steps in the common analysis chain so that the output from each stage can be fed into the following stage of analysis [91]. A detailed discussion of each stage of the analysis is presented in this chapter.

I have worked on the shower reconstruction stage and the result extraction stage of VEGAS as part of my work for this dissertation. Highlights includes a revisions to the shower reconstruction code to make it compatible with survey simulations and the development of the wobble mode data analysis class.

4.1 Data Calibration

The first stage of the analysis is to calculate all of the hardware dependent quantities so that any systematic biases can be corrected for. Otherwise a uniform light front impinging on the camera will look distorted since each pixel can respond differently to the same amount of light. The calibrations consist of removing the FADC-injected pedestal, equalizing the gains in each PMT and determining the correct trace arrival times in the FADCs.

4.1.1 Pedestal Removal

The main source of noise in each PMT is the fluctuating night sky background (NSB). In order to determine whether the detected photons are due to Cherenkov light and not background, it is necessary to quantify the fluctuations of the NSB.

The output of a PMT is AC coupled with a preamplifier to remove the steady current produced by the NSB and by any other dark currents. Since the FADCs cannot digitize positive voltage fluctuations, a constant negative offset of approximately 16 digital counts (DCs), called the pedestal, is injected into the PMT output so that the NSB fluctuations can be measured relative to this offset.

During each observation, the VERITAS telescopes are artificially triggered at a constant rate (1 Hz) so that a special type of data, called the pedestal events, can be recorded in the data stream in the absence of a Cherenkov shower. These pedestal events allow the charge deposited due to the NSB to be measured and they are tagged differently from normal shower events in the data file so that they can be treated separately.

The mean pedestal and its standard deviation, called the pedvar, which quantifies the NSB fluctuation, are calculated for each camera pixel in each data run.

For the mean pedestal of a pixel, the entire FADC trace for each pedestal event is integrated to obtain the charge deposited, in units of digital counts, and the average is taken over all pedestal events accumulated throughout the run. For the pedvar, since the NSB fluctuation in each pixel is not constant over the duration of a data run as the observing condition can change over time, it is calculated for each pixel every three minutes. This time scale was chosen as a compromise between the need to accumulate enough pedestal events for the pedvar calculation and the requirement to have a time frame that is sensitive enough to measure the changing NSB rate. Figure 4.1 shows example distributions of the pedvar values in the cameras for one run, 45055, taken on 23rd March, 2009.

4.1.2 FADC Timing Calibration

The arrival time, called T_0, of an FADC trace is defined as the time position of the location of the half maximum value of the leading edge of the trace. These arrival times can vary from pixel to pixel; this is because the arrival times depend on the cable lengths and other delays in the electronics system. To determine the arrival times accurately, a special "laser run" is taken every night where every pixel of the cameras is uniformly illuminated by laser pulses. The average timing difference in the ith channel, $T_{\text{offset}i}$, can then be calculated from these laser events. Let T_{event} be the average of arrival time of an event from all the channels:

$$T_{event} = \frac{1}{n}\sum_{k=1}^{n} T_{0k} \tag{4.1}$$

where n is the total number of channels and T_{0k} is the arrival time of the event in the kth channel. The time difference Δt_i between the arrival time of the event and the ith channel is then

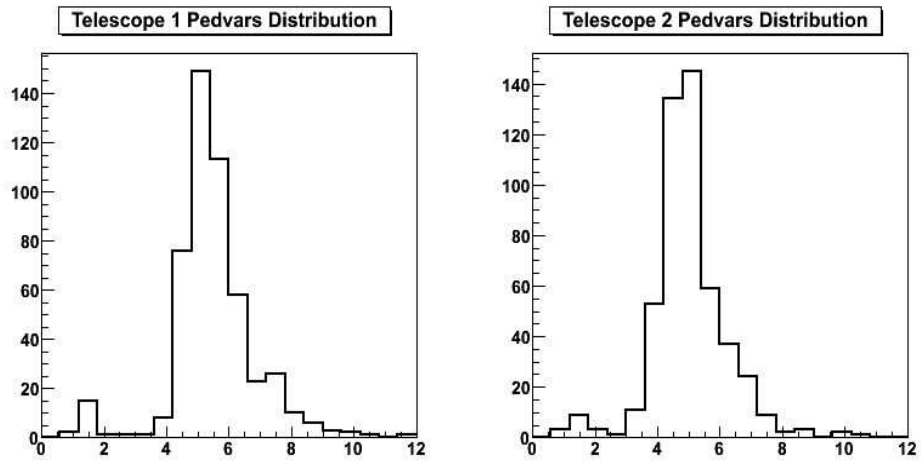

(a) Pedvar distribution in T1

(b) Pedvar distribution in T2

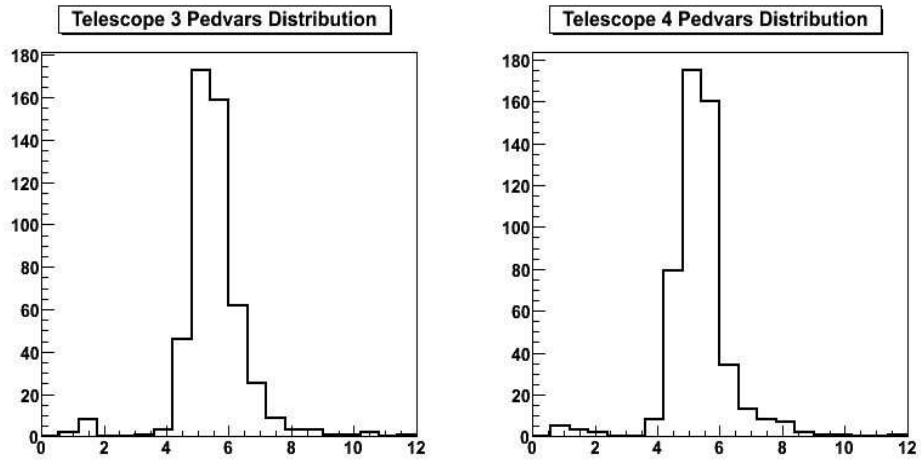

(c) Pedvar distribution in T3

(d) Pedvar distribution in T4

Figure 4.1: Distribution of the mean pedvar values in the individual cameras.

$$\Delta t_i = T_{0i} - T_{event}. \tag{4.2}$$

Averaging over large number of events, N, the average time offset for channel i is then given by

$$T_{\text{offset}i} = \frac{1}{N}\sum_{j=0}^{N} \Delta t_j. \tag{4.3}$$

The $T_{\text{offset}i}$ is then subtracted from the arrival times of the FADC traces for the ith channel in the data to get the the corrected arrival time of the signal. Figure 4.2 shows the T_0 distributions in the cameras for one run, 45055, taken on 23rd March, 2009.

4.1.3 Relative Gain Calibration

The charge deposited by a PMT depends on its quantum efficiency, collection efficiency and gain. To ensure that the FADC trace produced by each PMT for the same intensity of light will give an equivalent integrated charge, the laser runs (section 4.1.2), in which the cameras are uniformly illuminated, are used to calibrate the relative gain of the channels.

Let $\langle Q_i \rangle$ be the average charge produced by the ith laser event in a camera which is given by,

$$\langle Q_i \rangle = \frac{1}{M}\sum_{j=1}^{N} Q_{ij} \tag{4.4}$$

where M is the total number of channels on the camera, Q_{ij} is the charge produced by the jth channel from the ith laser event. The relative charge R_{Qij} of the jth channel from the ith event is then the ratio of Q_{ij} to $\langle Q_i \rangle$ i.e.

$$R_{Qij} = \frac{Q_{ij}}{\langle Q_i \rangle}. \tag{4.5}$$

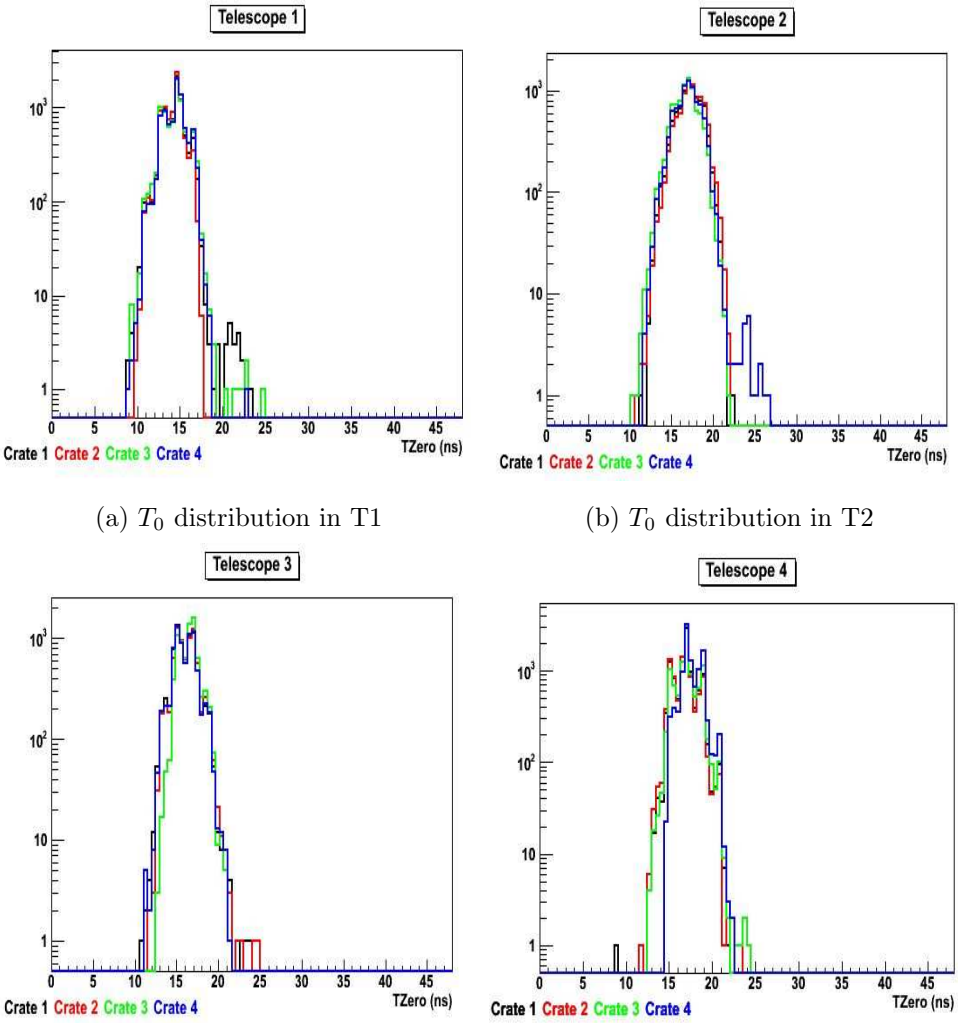

(a) T_0 distribution in T1

(b) T_0 distribution in T2

(c) T_0 distribution in T3

(d) T_0 distribution in T4

Figure 4.2: The T_0 distributions for every events in a run in each camera. The arrival time of the signal for individual pixels is different. Timing correction as described in the text is needed for accurate reconstructions of shower events.

The relative gain, G_j of the jth channel is then obtained by averaging the R_{Qij} over a large number, N, of laser events.

$$G_j = \frac{1}{N} \sum_{i=1}^{N} R_{Qij}. \tag{4.6}$$

4.1.4 Pixel Status Check

Pixels are disabled routinely in the presence of a bright star in the field of view or if they are broken or missing. The list of disabled pixels in each run is stored in the VERITAS database; these pixels can be removed in the analysis stage. However some faulty and noisy pixels are not identified during observation and therefore no information of them will be stored in the database; they have to be identified during the calibration stage. Since noisy pixels tend to have a very high pedvar, this value can be helpful in identifying bad pixels. Instead of cutting on the pedvar value, the scaled pedvar, p_{scaled} is used, given by

$$p_{scaled} = \frac{pedvar - \langle pedvar \rangle}{\sigma_{pedvar}} \tag{4.7}$$

where $pedvar$ is the pedvar value of the pixel, $\langle pedvar \rangle$ is the average pedvar value of all pixels and σ_{pedvar} is the standard deviation of the pedvar distribution. Note also that for a disabled pixel, the scaled pedvar has a very small value, hence p_{scaled} can also used to identify disabled pixels.

Bad pixels are defined as have a value outside the range of $-1.5 < p_{scaled} < 2.0$. Any pixels whose p_{scaled} values lie outside this range are excluded from participating in further data analysis.

4.1.5 Charge Integration

After all the hardware dependent quantities discussed above are collected, the charge deposited by each PMT is calculated. The pedestal level is subtracted from the FADC trace and the timing offset is used to determine the correct window to integrate the charge. The charge is then corrected for by multiplying it by the relative gain value.

4.2 Image Reconstruction

After calculating the calibrated integrated charges, the signals collected from the pixels are used for image reconstruction for each telescope. The image reconstruction involves first an image cleaning procedure followed by the parameterization of the light distribution of the shower.

4.2.1 Image Cleaning

Image cleaning is the process by which a subset of pixels belonging to the image are selected. A simple two-step cleaning procedure is used to identify pixels that contain Cherenkov light to remove those that are dominated by background photons. In the first step, also called the first pass, pixels with an integrated charge exceeding the picture threshold, defined as at least 5 times greater than their pedvar value, are selected as the picture pixels. In the second step, pixels that are adjacent to the picture pixels and whose integrated charge exceeds the boundary threshold, defined as at least 2.5 times greater than their pedvar value, are selected as the boundary pixels. The picture and boundary pixels together are called the image pixels and they define the Cherenkov shower image in the camera (figure 4.3).

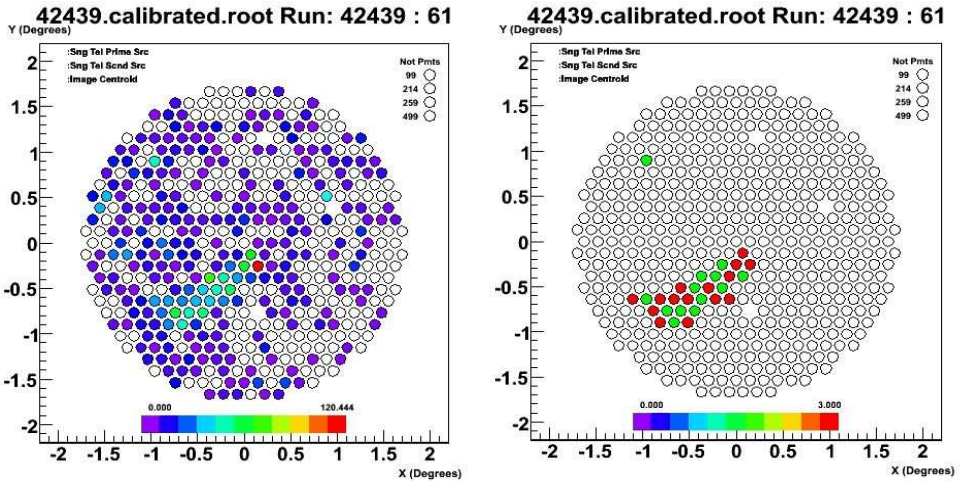

(a) An Image before Cleaning. (b) A cleaned Image

Figure 4.3: Left: A camera image before the cleaning process. Right: The same image after cleaning. The green pixels denote the picture pixels and the red pixels denote the boundary pixels.

4.2.2 Image Parameterization

After the shower images are cleaned, they are then parameterized based on the moments of their light distributions. The set of parameters employed in VERITAS was first proposed by Hillas [76]. A schematic representation of the Hillas parameters is shown in figure 4.4 and their definitions are given here :

Length: Angular size of the semi-major axis of the image.

Width: Angular size of the semi-minor axis of the image.

Distance: Distance between the centroid of the image to the center of the field of view.

Azwidth: The width of the light distribution that is perpendicular to the line connecting the centroid to the center of the field of view.

Alpha: The angle between the semi-major axis of the image and the line connecting the centroid to the center of the field of view.

Size: The sum of the total integrated charges in the image pixels. This measures the total light content of the image.

The Hillas parameters are used to identify good-quality images from each telescope which can then be used in reconstructing the shower parameters. They can also be used for single-telescope data analysis.

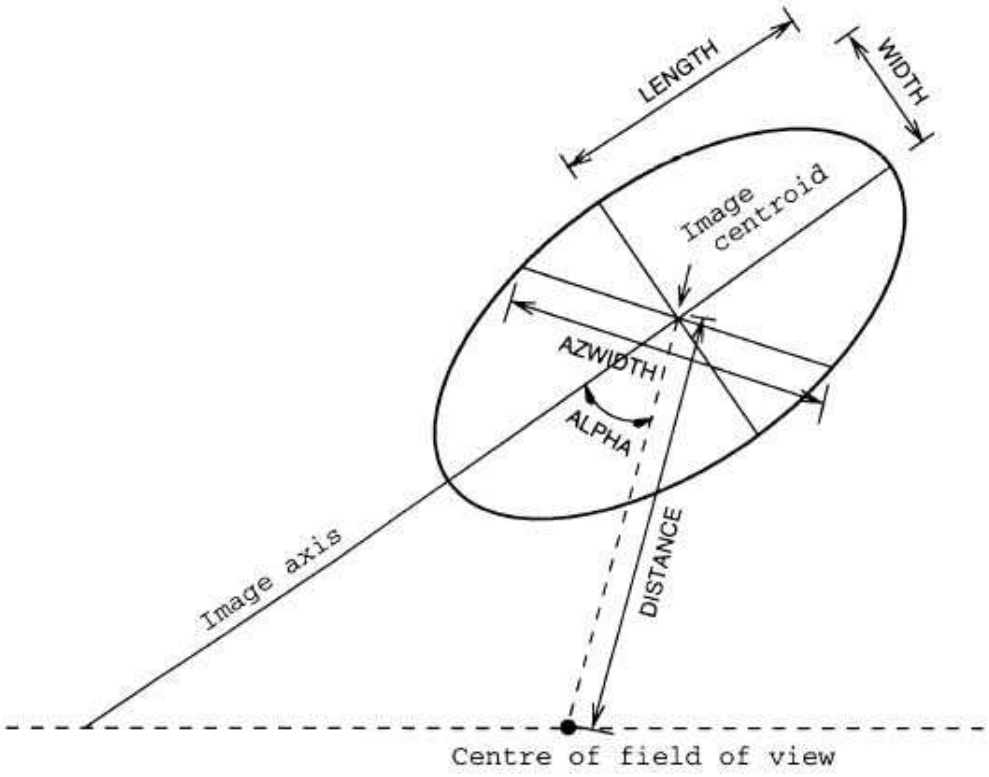

Figure 4.4: A schematic representation of the definitions of the different Hillas parameters described in the text. Figure taken from [76].

4.3 Shower Reconstruction

The parameterized images from each telescope are combined and used to reconstruct the Cherenkov shower through the stereoscopic reconstruction technique. Simple geometrical techniques are used to determine the source position and the shower core location. Shower simulations are used to determine the energy of the gamma ray and to estimate the stereo parameters, the mean scaled length (MSL) and the mean scaled width (MSW) (section 4.3.4). In VERITAS simulations, the pointing direction of the array is commonly parametrized by the local coordinate system, i.e. zenith and azimuth. Zenith is defined to be the angle from vertical and azimuth is defined to be the angle from the North direction.

4.3.1 Image and event selection

The Hillas parameters introduced in section 4.2.2 are used to select good camera images which will be used for shower reconstruction. At this stage, the parameters that are employed are the number of pixels of an image, N_{tubes}, the *size*, and *distance*. These parameters are helpful in throwing out images that may cause inaccurate shower reconstruction, for example: images that are too faint, characterized by a small *size*, have no clear shape, characterized by small N_{tubes} and are truncated, and characterized by large *distance*. These are called quality cuts, and for this work, an event is excluded from analysis if $N_{tubes} < 5$, $distance > 1.43$ and $size < 600$ or $size < 1000$ depending on the situation (see chapter 5 for more details).

Once the images pass through the quality cuts, they are further subjected to the event selection cut. The requirements are that at least two camera images from two telescopes are available for shower reconstruction and that the angle

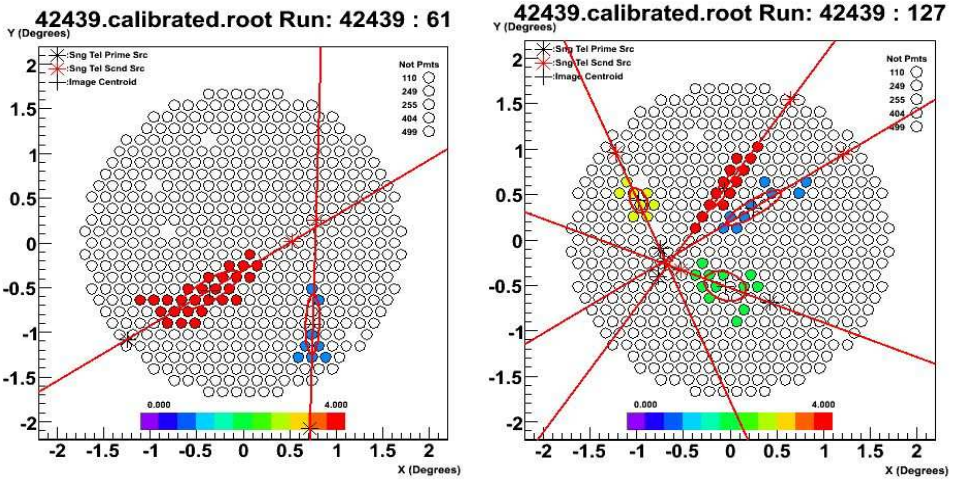

(a) Reconstruction of source position using two images.

(b) Reconstruction of source position using four images.

Figure 4.5: Left: Source position reconstruction using two images. Right: Source position reconstruction using four images. The lines extended from each semi-major axis of the parametrized images do not intersect at a point; hence a weighted centroid is used in such cases.

between the lines extending from each telescope along the semi-major axes is greater than 10°. Also note that events that are only triggered by T1 and T4 are rejected since the two telescopes are physically close to each other and these events are dominated by small showers and muons.

4.3.2 Shower Source Position

With multiple images from different telescopes, the source position of the shower can be reconstructed by finding the intersection of the lines extended from the semi-major axis of the images in the field of view (figure 4.5). If more than two images are available, the point which minimizes the perpendicular distance squared to the centroid of each image is defined to be the shower direction. Note

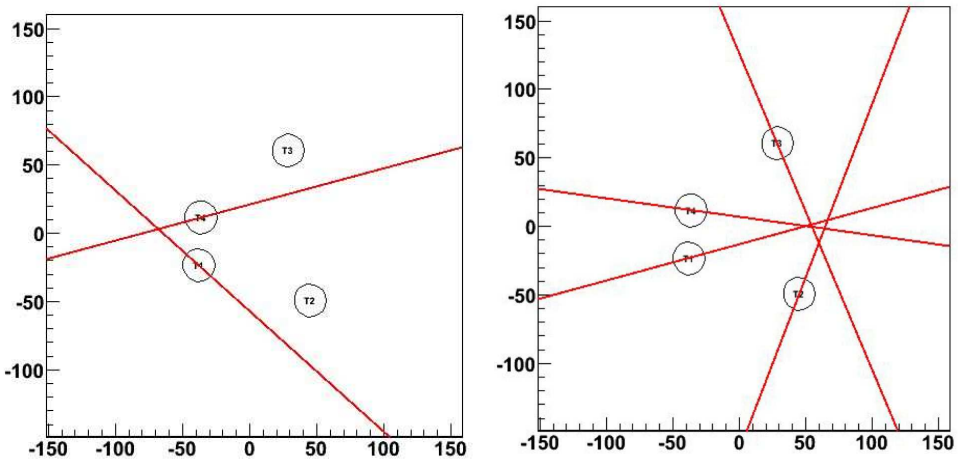

(a) Reconstruction of shower core position using two images.

(b) Reconstruction of shower core position using four images.

Figure 4.6: Left: Shower core location reconstruction using two images. Right: Shower core location reconstruction using four images. A weighted centroid is found when multiple images are used.

that in this calculation the distance is weighted by the *size* parameter [93]. The *size* parameter is used as the weighing factor since a brighter image should have a more well defined semi-major axis than a fainter image.

4.3.3 Shower Core Reconstruction

The shower core location is also found by a simple geometrical reconstruction. The core location is the position where the shower would have hit the ground. The lines extended from semi-major axes of the images are used to find this point, by projecting the lines from the individual cameras onto the mirror plane [94]. The intersection of the lines then gives the core location (see figure 4.6). The distance between the core location and a telescope is called the impact distance for that telescope.

4.3.4 Shower Parameters Reconstruction

In VERITAS, two shower level parameters are commonly used to discriminate gamma-ray events from the much more numerous cosmic-ray events. They are the mean scaled length (MSL) and the mean scaled width (MSW). These two mean scaled parameters (MSP) are obtained by combining Hillas parameters with the predictions from Cherenkov shower simulations. The MSPs are given by [95]

$$MSP = \frac{1}{n_{tel}} \sum_{i=1}^{n_{tel}} \frac{p_i}{\bar{p}_{sim}(b, size)} \tag{4.8}$$

where n_{tel} is the number of telescopes that contain a shower image, p_i is the parameter ($width$ or $length$) in the ith camera and $\bar{p}_{sim}(b, size)$ is the expected value of p_i given the impact parameter, b, and the $size$ of the image. The values of $\bar{p}_{sim}$ are obtained from a database, called a lookup table, which store a computed parameter values derived from a large number of Monte Carlo simulations of gamma rays of different image sizes and impact parameters. Example of lookup tables for MSL and MSW are shown in figure 4.7 and 4.8.

4.3.5 Energy Reconstruction

The energy of the primary particle, like the MSPs, is obtained from simulation-generated lookup tables. Estimates of the energy are first obtained for individual telescopes based on the $size$ of the image and the impact parameter with respect to the telescope. Then an average weighted by the $size$, is computed and the result is the estimated energy. An example of an energy lookup table is shown in figure 4.9.

The fractional error of a given event in the reconstructed energy can be obtained from simulated events given by

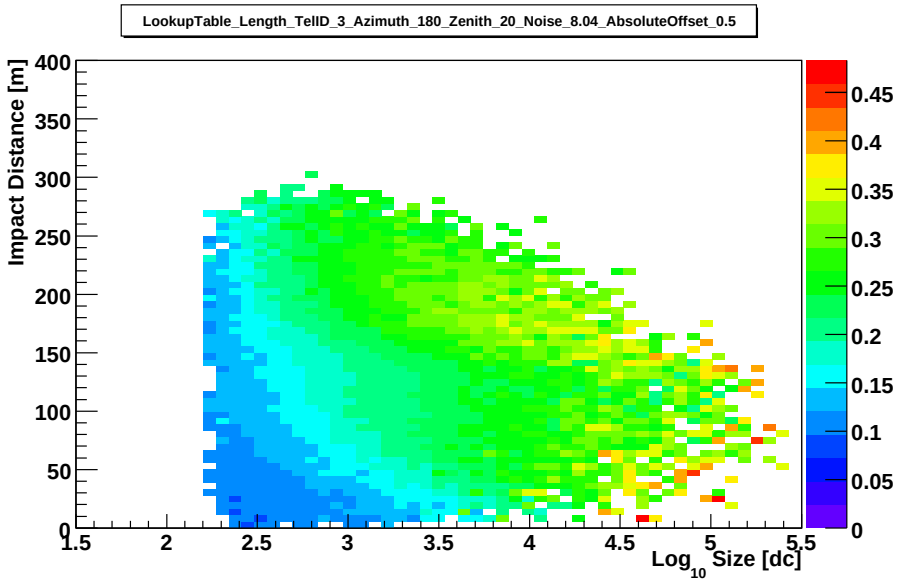

Figure 4.7: A 2D histogram showing the data in a MSL lookup table for Telescope 3. This lookup table was generated for simulated events from zenith= 20°, azimuth=180° and the wobble offset is 0.5°. The camera noise level was set to 8.04 digital counts. The MSL values are represented by the color scale and they are parametrized by impact distance and *size*.

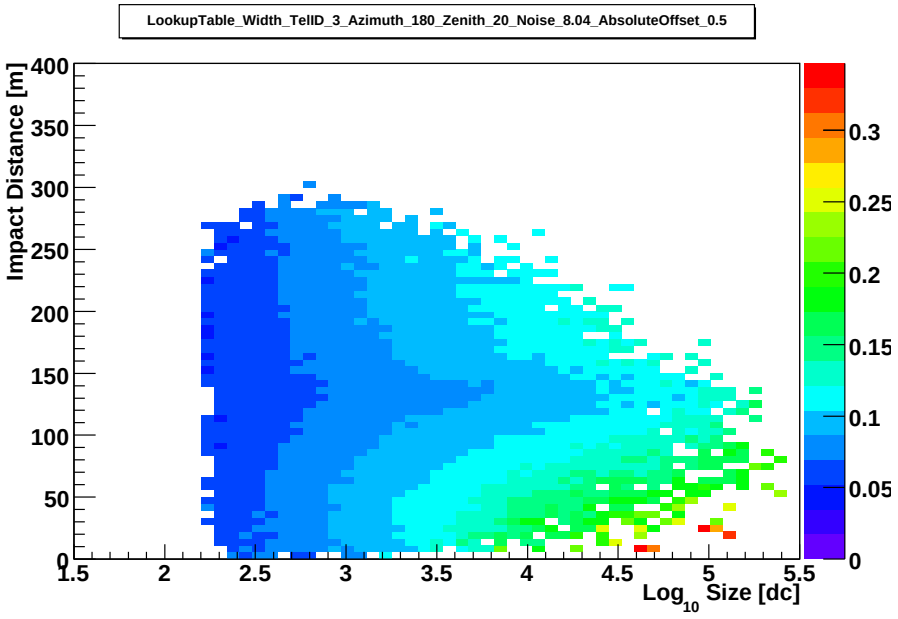

Figure 4.8: A 2D histogram showing the data in a MSW lookup table for Telescope 3. This lookup table was generated for simulated events from zenith= 20°, azimuth=180° and the wobble offset is 0.5°. The camera noise level was set to 8.04 digital counts. The MSW values are represented by the color scale and they are parametrized by impact distance and *size*.

$$\Delta E = \frac{E_{rec} - E_{true}}{E_{true}}. \tag{4.9}$$

where E_{true} is the true energy of the simulated event and E_{rec} is the reconstructed energy of the simulated event. The energy bias, E_{bias}, is defined as the mean value of the fractional error. E_{bias} is a good measure of whether the energy estimation be trusted (i.e. when the fractional error is less than 10%). Figure 4.10 shows an example of an energy bias curve. More detailed discussion of the spectrum reconstruction is in section 4.6.2.

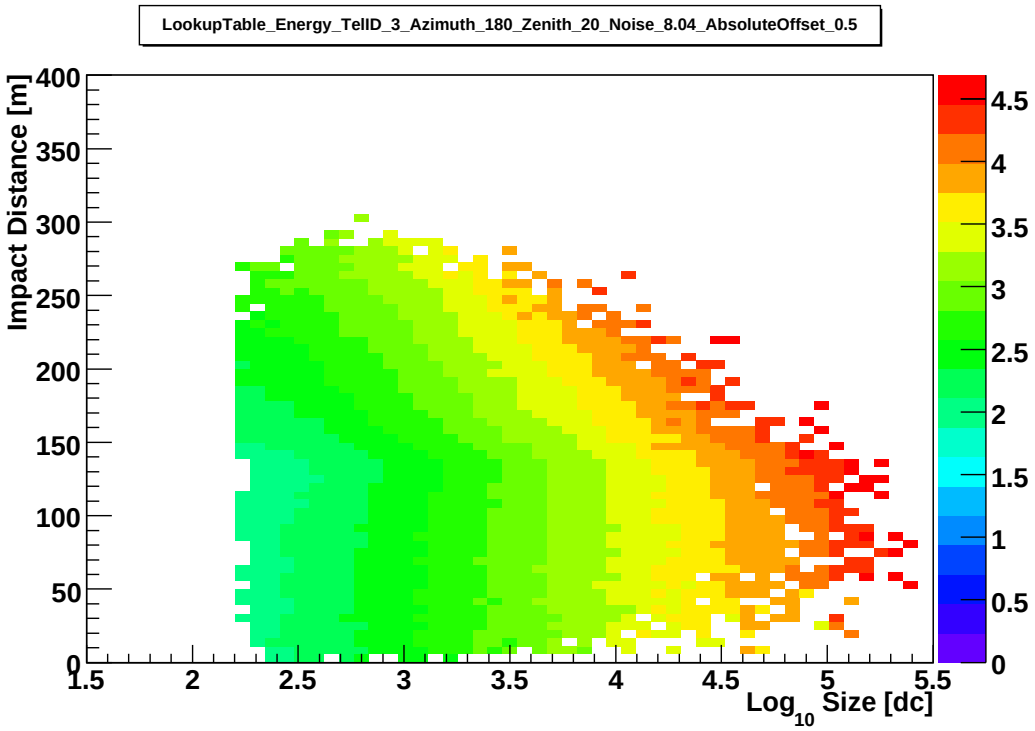

Figure 4.9: A 2D histogram showing the data in an energy lookup table for Telescope 3. The color scale gives the log(Energy(GeV)) value in each bin parametrized by impact distance and *size*. This lookup table was generated for simulated events from zenith=20°, azimuth=180° and the wobble offset is 0.5°. The camera noise level was set to 8.04 digital counts.

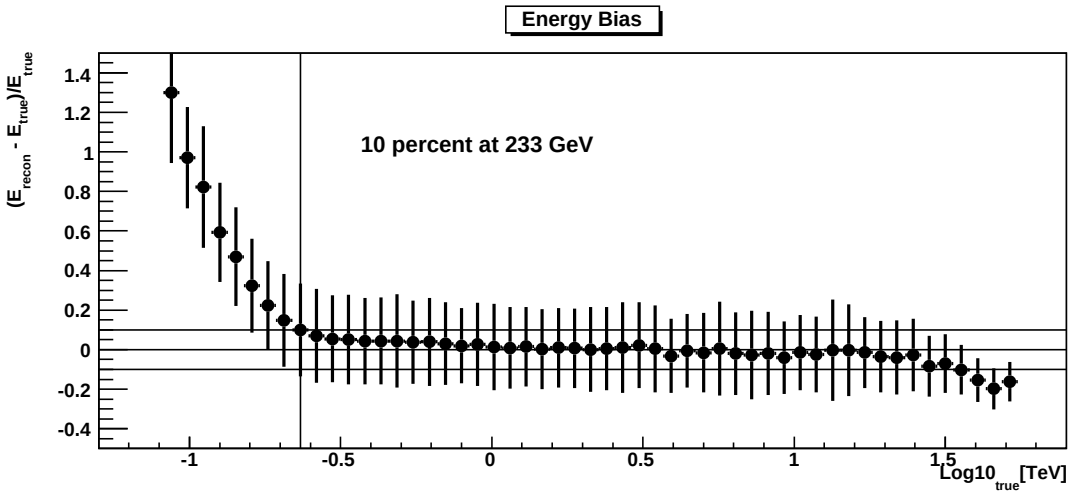

Figure 4.10: An example of an energy bias curve. This figure was generated for the full 4-telescope array. The simulated events are from zenith=20° and azimuth=180°. The vertical line shows the lower edge of the safe energy range above which the energy bias (fractional error) is lower than 10%. For this particular simulation set, the lower edge is at 233 GeV.

4.4 Event Selection

Depending on the type of the source under consideration, different sets of parameter cuts are used for gamma-hadron separation. The most commonly used parameters are mean scaled length, mean scaled width, and θ^2 (the distance between the reconstructed position of an event and the source position squared). To find the most suitable range of values for event selection, optimizations on a set of 4-telescope Crab data were done as required, e.g. when major hardware changes occurred and for new analysis software. Since in general one is interested in detecting faint sources, a useful parameter for optimization is the ratio $\frac{R_{bg}}{R_\gamma^2}$, where R_{bg} is the background event rate and R_γ^2 is the gamma-ray event rate. This ratio is proportional to the time required to detect a source in the limit $R_\gamma \ll R_{bg}$ [97]. The selection criterion used in this dissertation will be given in chapter 5.

4.5 Background Estimation

In order to determine the excess gamma-ray counts and whether a gamma-ray source is present, an estimation of the background level is needed. Two background estimation methods are commonly used in VHE gamma-ray astronomy; they are the reflected region method (section 4.5.1) and the ring background method (section 4.5.2) [96]. The number of excess gamma-ray events, N_γ, is given by,

$$N_\gamma = N_{on} - \alpha N_{off} \tag{4.10}$$

where N_{on} is the number of events in the source region (the *on* region), N_{off} is the number of events in the off regions and α is a normalization factor. The

α is the ratio of the background expectation value of the *on* and off regions and is given by

$$\alpha = \frac{\int_{on} \epsilon(x,y)dxdy}{\int_{off} \epsilon(x,y)dxdy} \tag{4.11}$$

where $\epsilon(x,y)$ is the acceptance function for gamma-ray like events which depends on the position in the camera, x and y. To first approximation, the acceptance function can be taken to be radially symmetric. The acceptance at a point on the camera is the relative probability for a gamma-ray-like event to be detected at that point.

4.5.1 Reflected Region Method

The reflected region method is normally used for data taken in wobble mode observation where the source position is offset, say by 0.5°, from the center of the field of view. In this method, the *on* region is defined to be a circle of radius θ around the target position and the offregions are chosen to be circles, with the same radius θ, that are also located r degrees from the center of the FOV. The off regions are located as far away from the *on* region as possible to avoid source gamma-ray contamination. To improve the estimation, multiple background regions can be used and an example is shown in figure 4.11. Assuming that the acceptance function is radially symmetric, the α factor simplifies to

$$\alpha = \frac{\int_{on} \epsilon(r)dxdy}{\int_{off} \epsilon(r)dxdy}. \tag{4.12}$$

Since the radial distances are the same for both *on* and off regions, $\alpha = \frac{1}{N}$ for the reflected region method, where N is the number of background regions.

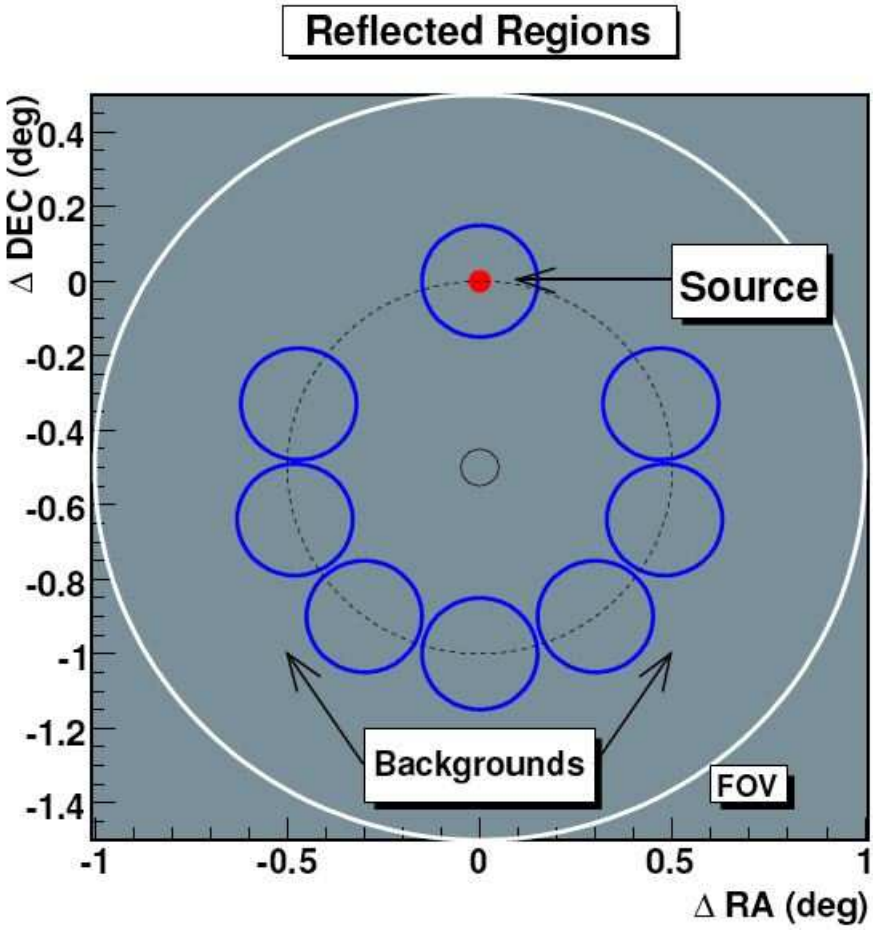

Figure 4.11: The reflected region method for background estimation. This figure shows the locations of the regions used as the source and background regions. The red dot indicates the location of the target and the circle around it denotes the region that is used as the *on* region. The other blue circles denote the regions that are used for background estimation. The broken circle denotes radius of the wobble offset. The small black circle denotes the center of the FOV and the big white circle denotes the FOV of VERITAS. Figure taken from [95].

4.5.2 Ring Background method

Another popular background estimation method is the ring background method (RBM). RBM has no *a priori* assumption on the location of a source, each point on the map is a trial source position; a small circular region around each trial source position is defined to be the *on* region and an annulus far enough away from the *on* region is used as the background region. See the diagram in figure 4.12.

Unlike the reflected region method, the α factor of RBM is not a simple expression, since the annulus used for the background covers a different part of the camera than the signal region. To take into account the nonuniform acceptance distribution, the α factor has to be calculated for each point in the dataset. α in this case is derived from the ratio of the integral acceptance of the *on* region to the integral acceptance of the off region. The expression for α is

$$\alpha_i = \frac{\int_{on} \epsilon(x,y)dxdy}{\int_{off} \epsilon(x,y)dxdy}. \tag{4.13}$$

where α_i is the normalization factor in the trial position i and $\epsilon(x,y)$ is the acceptance at the camera position x, y.

4.6 Signal Detection and Spectrum Reconstruction

Given an excess number of gamma rays for a putative source, a statistical test is needed to establish the significance level of the detection. A frequently used statistical test within the gamma-ray astronomy community was derived by Li and Ma [92]; more details follow in section 4.6.1. Once a source has been confirmed, its energy spectrum can be reconstructed. The energy spectrum is an important

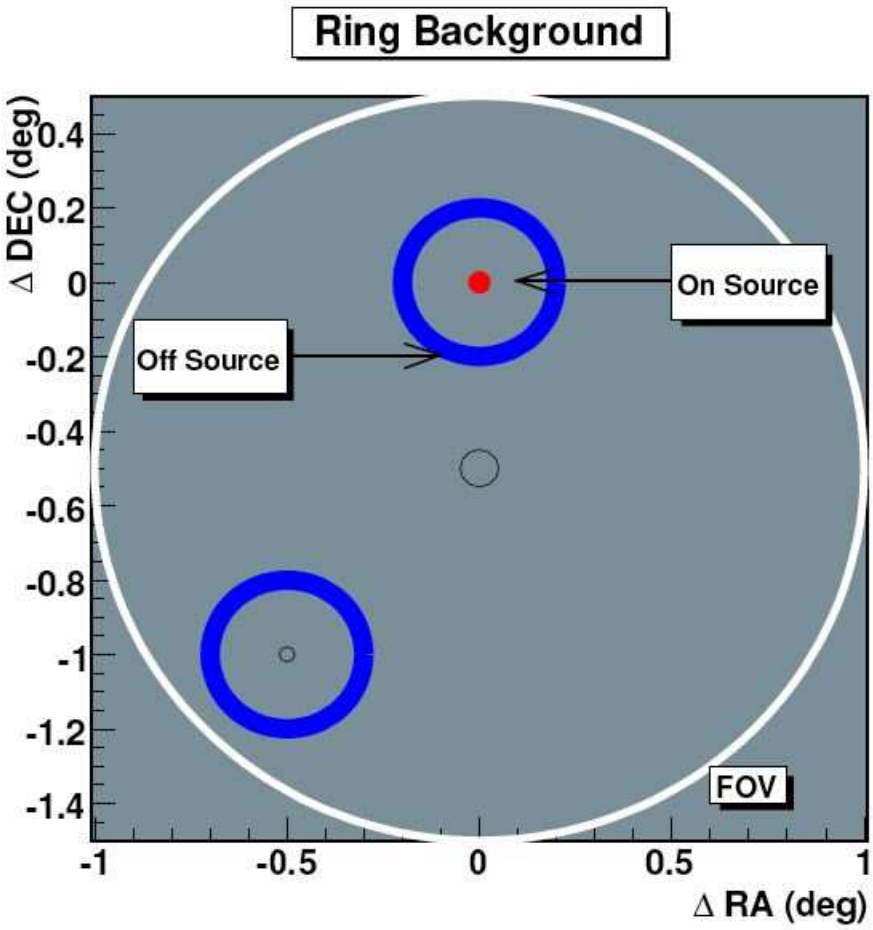

Figure 4.12: The ring background method for background estimation. This figure shows the different regions used. The red dot represents the *on* region. The solid blue annulus represents the off region that will be used for background estimation for the *on* region inside of it. In RBM there is no a priori defined source position; each location inside the FOV is treated as a trial source location with its corresponding background region. Figure taken from [95].

.

piece of information about the source, since the spectrum can reveal the nature of the physical process which enable the source to generate VHE gamma rays.

4.6.1 Signal Detection and Rate

The Li and Ma formula used in gamma-ray astronomy was derived from a maximum likelihood ratio test against the null hypothesis that the excess count of gamma ray detected is due entirely to background fluctuations [92]. The significance level, σ, from the Li and Ma formula is given by

$$\sigma = \sqrt{2}\left(N_{on} ln\left[\frac{(1+\alpha)\,N_{on}}{\alpha\,(N_{on}+N_{off})}\right] + N_{off} ln\left[\frac{(1+\alpha)\,N_{off}}{N_{on}+N_{off}}\right]\right)^{\frac{1}{2}} \tag{4.14}$$

where the N_{on} is the number of gamma-ray counts in the *on* region of the background model used, N_{off} is the number of gamma-ray counts in the off regions, and α is the normalization factor of the background model.

The gamma-ray rate of the source, r, is calculated by the following formula,

$$r = \frac{N_{on} - \alpha N_{off}}{T_{live}} \tag{4.15}$$

where T_{live} is the live time, the duration of the observation corrected for the dead time, and the other symbols have their usual meaning.

4.6.2 Spectrum Reconstruction

The differential energy spectrum, $\mathcal{F}(E)$, is defined as the number of particles emitted from the source per unit area, time and energy. It can be expressed as

$$\mathcal{F}(E) = \frac{1}{t_{live} A(E)} \frac{dN_\gamma}{dE} \tag{4.16}$$

where t_{live} is the live time of the observation, N_γ is the number of gamma rays detected, E denotes the energy of a gamma ray and $A(E)$ denotes the effective area of the instrument at energy level E.

The effective area, or collection area, $A(E)$, of a VHE gamma-ray telescope describes the collection capacity of the instrument. It is determined from Monte-Carlo simulations since there is no naturally occurring source which can produce constant stream of gamma rays at discrete energies. The effective area depends on the energy, E, of the gamma rays and the zenith angle, Θ, at which the data were taken. To determine $A(E)$, a large number, $N(E, \Theta)$, of simulated gamma rays are randomly distributed to arrive over a large area, A_0, where A_0 is defined to be the circular region centered around the telescopes. The number of simulated gamma-ray events, $n(E, \Theta)$, which are successfully reconstructed and which pass through all cuts are recorded. $A(E)$ is then given by

$$A(E, \Theta) = A_0 \frac{n(E, \Theta)}{N(E, \Theta)} \tag{4.17}$$

Since the amount of Cherenkov light produced depends on the energy of the incident gamma ray, it is expected that at lower energies the effective area will be smaller, whereas at higher energies, the effective area will be greater. Examples of effective area curves are shown in figure 4.13.

The energy spectrum is calculated from a binned vision of equation 4.16. To do this, the effective area curves need to be modified since the instrument has a finite energy resolution i.e. some events are unavoidably assigned to the wrong energy bin. For a rapidly falling power-law spectrum that is common for VHE gamma-ray sources, events are more likely to be assigned to a higher energy bin. The modified effective area curves, $A'(E, \Theta)$, are constructed to correct for this biases. A detailed description of $A'(E, \Theta)$ can be found in [98].

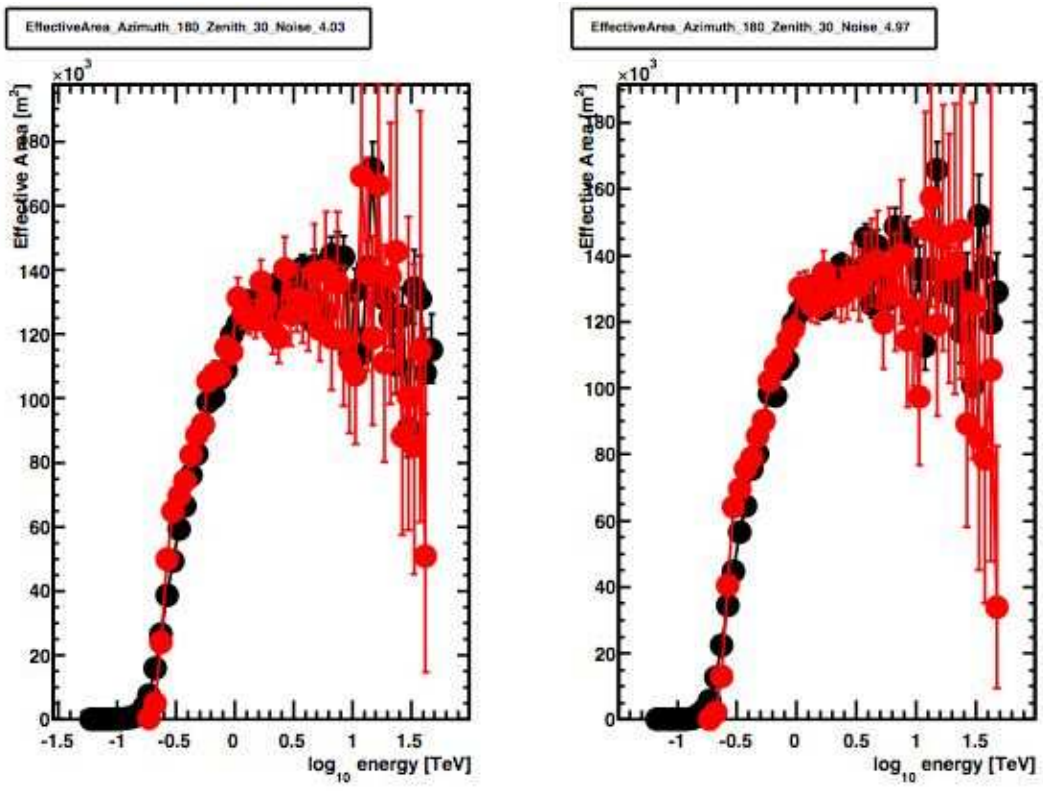

Figure 4.13: Plots of different effective area curves constructed from the simulation of gamma rays from zenith of 30° and azimuth of 180° at different background noise levels. The black dots denote the effective area values as a function of the true energy of the simulated gamma rays and the red dots represent the effective area values as a function of the reconstructed energy of the simulated gamma rays.

Once the modified effective area curves are obtained, one proceeds to determine the spectrum. The flux per energy bin of width ΔE is given by

$$\mathcal{F}(\Delta E) = \frac{1}{t_{live}\Delta E}\left(\sum_{j=1,E_j\in\Delta E}^{N_{on}} \frac{1}{A'(E_j,\Theta)} - \alpha \sum_{j=1,E_j\in\Delta E}^{N_{off}} \frac{1}{A'(E_j,\Theta)}\right) \tag{4.18}$$

where E_j is the energy of the jth particle, N_{on} is the number of events in the *on* region, N_{off} is the number of events in the off region, α is the normalization factor and t_{live} is the live time of the data set. As mentioned in section 4.5.3, only the part of the spectrum where the energy bias is less than 10% can be safely reconstructed. Once the the flux per energy bin has been calculated over the safe energy range, the differential energy spectrum is obtained from a minimum χ^2 fit to the flux data points, assuming a power-law form

$$\mathcal{F}(E) = \frac{1}{t_{live}A(E)}\frac{dN_\gamma}{dE} = F_0 E^{-\Gamma} \tag{4.19}$$

where F_0 is called the flux constant and Γ is called the photon index, or spectral index, of the source. Besides the statistical error inherent to the power law fit, there is also the component of systematic error due to the uncertainties in the assumptions used in the simulations of gamma-ray showers, the modeling of the detector and the different conditions in which the data were taken. All of these factors can affect the final result. An estimation of the systematic error in spectral reconstruction using VERITAS data was performed in [99] and was estimated to be 20%.

CHAPTER 5

VERITAS Sky Survey

A deep survey of the Cygnus arm region was designated as one of the four key science projects in the first two years of operation of VERITAS. The survey region is bounded by $67^\circ < l < 82^\circ$ and $-1^\circ < b < 4^\circ$ where l and b are the Galactic longitude and latitude, respectively. The survey began in April 2007 and concluded in November 2009, including follow-up observations on promising candidate targets. The total time spent on the survey was approximately 168 hours of which 112 hours was devoted to the base survey (see section 5.1) and 56 hours for follow-up observation. For this dissertation, only data taken before July 2009 was used, the total observing time for this data set is $\sim$143 hours (430 20-minute long data runs). The average sensitivity (5 σ detection) of the survey is estimated using simulation (section 5.2) to be approximately at the 5% Crab flux level.

I worked on many stages of the survey project, from scheduling the night by night observing program to sensitivity simulations and an independent analysis on all the survey data. In this chapter, a comprehensive review of the survey related work will be given. The observing strategy for the survey is described in section 5.1. Section 5.2 presents the analysis of survey-related simulations to evaluate and validate the survey strategy. The analysis procedure of the survey data is given in section 5.3. Preliminary survey results are presented in section 5.4

5.1 Observing strategy for the Survey

The survey region $67° < l < 82°$ and $-1° < b < 4°$, is divided into grid points that are separated by 0.8° in longitude and 1° in latitude. A total 1-hour exposure, equivalent to three 20-min runs, is taken at each grid point in the region (see figure 5.1). This exposure is defined as our base survey. Additional time for re-observations of promising candidates were added as needed. Here we define a promising candidate as a hot spot in the region that has a pre-trial significance of 4 σ or greater for a point source or 3.5 σ for an extended source. In section 5.3 we discuss how the analysis procedure is tuned to search for point and extended source.

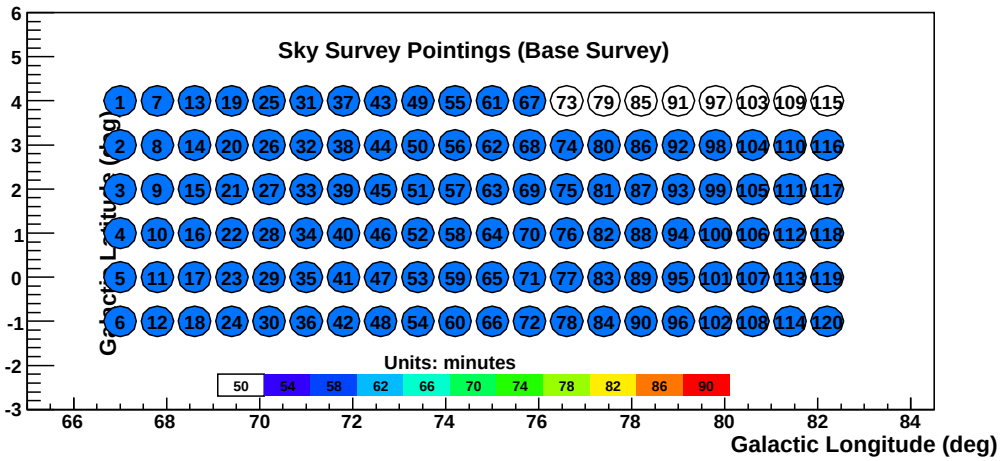

Figure 5.1: A schematic representation of the survey grid as described in the text. Each circle represents a pointing and, for each pointing, a minimum of 1 hour of exposure is required. Each circle is identified by a number from 1-120.

5.2 Survey-related Simulation results

5.2.1 Survey Simulations

The sensitivity of the survey was estimated for a "typical" survey point, i.e. a point that is well within the nominal boundaries of the survey (see figure 5.2), using a combination of actual survey data and simulated gamma-ray showers, which are produced using the ChiLa package. ChiLa consists of several subpackages which simulate extensive air showers and the associated Cherenkov light production and the optical and electronic systems of VERITAS. The outputs of the simulations are saved in a VBF file (chapter 3) which can then be analyzed with VEGAS (chapter 4). More technical details of ChiLa can be found in [100]. The procedure to estimate the sensitivity is described below.

1. A set of 30 sky survey data runs (appendix A) from an assumed empty region of the survey data set were selected as background for the simulations. The runs were arranged in a survey-pointing grid (figure 5.2). Each pointing has one hour of exposure which is equivalent to three data runs per grid point. To begin the process, these runs were processed through the analysis chain up to the shower reconstruction point with the VEGAS analysis package as described in chapter 4.

2. For each of the 30 data runs, a set of simulated gamma rays calibrated to match the observing conditions of that particular run was produced using the ChiLa simulation package [100] and processed with VEGAS.

3. The background data from step 1 and the simulated gamma-ray data produced from step 2 were then merged together to produce a single output file containing both types of data.

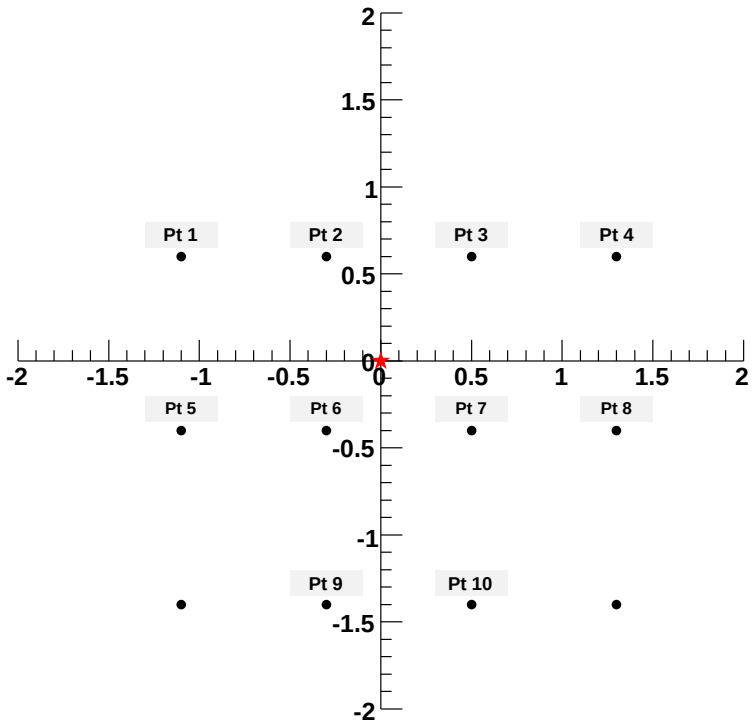

Figure 5.2: A schematic drawing of the grid used for the survey simulations as described in the text. Points 1-10 represent the center of the FOV of the ten survey background runs. The red star represents the location of the injected simulated gamma rays. The resulting data sample provides an estimate of the sensitivity of the survey.

4. The merged data from step 3 were then processed through the last stage of data analysis using VEGAS to extract the signal strength and rate.

A flowchart summarizing the procedures outlined above is shown in figure 5.3.

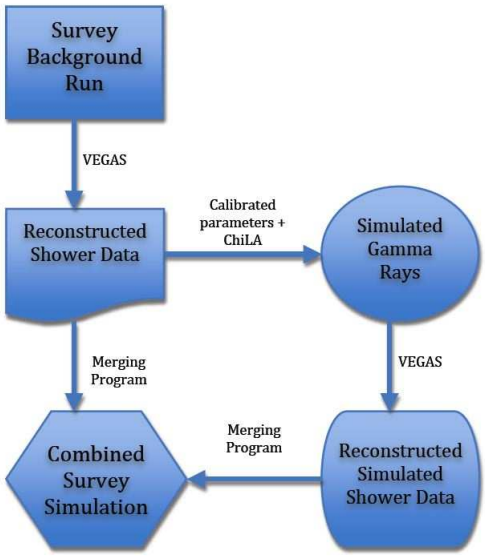

Figure 5.3: A flowchart representing the procedure used to create the survey simulations. The details are summarized in the text.

Simulation Results One of the great features of the ChiLa simulation package is its capability to easily generate gamma-ray sources with different spectral indices and observing conditions. The simulations described in the previous section were repeated to generate gamma rays of different spectral indices and angular extent in order to investigate the performance of the analysis software to different types of sources that we could expect to encounter in the Galactic plane survey data. The gamma/hadron separation cuts used were the same as those used in an optimization study in 2008 [101]. Table 5.1 shows the estimated sensitivity and the gamma/hadron separation cuts used for a typical point in the survey grid for

different flux levels of a point source with a Crab-like spectrum ($E^{-2.4}$). Additionally, extended source simulations were carried out for a hypothetical source that had a 0.2 degree Gaussian radius and a 10% Crab flux level with a spectral index of 2.0 (table 5.2). These parameters were chosen because it was expected that potential sources in the Cygnus region would have a hard spectrum, and the combination of the angular extent and the flux level represent the faintest such source that could be detected by VERITAS during the survey.

The estimated sensitivity for the survey grid style observations are very consistent to the normal sensitivity of VERITAS using wobble mode observations, for example, the sensitivities for 3% and 10% Crab point sources were estimated in the survey simulations to be $2.64\frac{\sigma}{\sqrt{(h)}}$ and $5.94\frac{\sigma}{\sqrt{(h)}}$ respectively whereas from the optimization study in Fall 2008, the sensitvities for the same source strengths were found to be $2.12\frac{\sigma}{\sqrt{(h)}}$ and $6.10\frac{\sigma}{\sqrt{(h)}}$ respectively [101].

5.3 VERITAS Survey Data and Analysis

Between April 2007 and July 2009, VERITAS took approximately 143 hours of survey data on the Cygnus arm region. The data include the base survey data and follow-up observations on promising candidates discovered after the first round of analysis. Note that additional follow-up observations were carried out in Fall 2009 but that data set was not included in the work of this dissertation. In this section, a full description of the survey data set taken between April 2007 and July 2009 and their analysis results are given. To facilitate the description of the analysis, the discussion is divided into three parts:

Part 1: This is the original survey data set taken between April 2007 and October 2008.

% Crab	Aperture	msl	msw	Sensitivity $[\sigma/\sqrt{(h)}]$	Rate [γ/min]
1%	0.112	(0.05, 1.24)	(0.05, 1.06)	0.66 ± 0.43	0.029 ± 0.019
3%	0.112	(0.05, 1.24)	(0.05, 1.06)	2.64 ± 0.49	0.123 ± 0.023
5%	0.112	(0.05, 1.24)	(0.05, 1.06)	3.14 ± 0.50	0.153 ± 0.024
10%	0.112	(0.05, 1.24)	(0.05, 1.06)	5.94 ± 0.55	0.337 ± 0.031

Table 5.1: This table shows the sensitivity of VERITAS using survey style grid observations for different flux levels of a point source of gamma rays with spectral index 2.0. Aperture is the radius used for the *on* region. Msl and msw are the mean scaled length and width parameters introduced in chapter 4; the bracketed values are the accepted range for the cuts on these parameters. The sensitivity values need to be multiplied by the effective exposure of $\sim$ 6 hours to get the expected significance values.

Part 2: Follow-up observations between October 2008 and December 2008.

Part 3: Follow-up observations in May/June 2009.

5.3.1 Part 1: The First Survey Data set

The first part of the sky survey project began in April 2007 and ended around October 2008. The objective was to scan as much of the Cygnus arm region as possible using the strategy described in section 5.1. Since the region is in the part of the sky that is difficult to observe from the VERITAS location (mainly due to the monsoon season during the months of July and August), a scheduling program was written to assist the observers in planning an efficient way of observing the targets. To ensure good data quality, several members of the sky survey group

% Crab	Aperture	msl	msw	Sensitivity $[\sigma/\sqrt{(h)}]$	Rate [γ/min]
10%	0.224	(0.05, 1.29)	(0.05, 1.06)	2.58 ± 0.49	0.122 ± 0.023

Table 5.2: This table shows the sensitivity of VERITAS using survey style grid observations for an extended source with a 0.2 degree Gaussian radius, a 10% Crab flux level, and a spectral index of 2.0. Aperture is the radius used for the *on* region. Msl and msw are the mean scaled length and width parameters introduced in chapter 4; the bracketed values are the accepted range for the cuts on these parameters. The sensitivity values need to be multiplied by the effective exposure of ~ 6 hours to get the expected significance values.

were assigned the responsibility of next-day data quality monitoring to rapidly identify problematic runs caused by faulty hardware or undesirable observing conditions (e.g. bad weather) so that the observers could retake data, if necessary, for the same target. The strategy proved to be very successful and over 100 hours of high quality data were taken during this period. The complete list of usable runs can be found in appendix B.

The survey data were analyzed by different groups in the sky survey project using two major VERITAS analysis packages, eventdisplay and VEGAS (chapter 4). The results from this dissertation were derived using the VEGAS implementation of the ring background method (RBM) (section 4.5.2).

The quality and gamma/hadron separation cuts applied to this data set were obtained from optimization studies on a set of Crab data taken using a survey-style grid (figure 5.2) [102]. Four sets of cuts were used, each designed to be sensitive to the different types of sources that are expected to be in the Galactic plane: (1) soft spectrum point source, (2) soft spectrum extended source, (3)

Cut Type	Size (d.c.)	ntubes	dist
Soft/Point	≥ 600	≥ 4	(0.05, 1.43)
Soft/Extended	≥ 600	≥ 4	(0.05, 1.43)
Hard/Point	≥ 1000	≥ 4	(0.05, 1.43)
Hard/Extended	≥ 1000	≥ 4	(0.05, 1.43)

Table 5.3: Shower reconstruction quality cuts used in part 1 of the data set for the four separate analyzes. Size is the parameter that measures the brightness of an image (in digital counts), ntubes is the number of adjacent pixels in an image and dist is the distance of the centroid of an image to the center of the FOV.

hard spectrum point source and (4) hard spectrum extended source. The quality cuts used in the shower reconstruction stage are shown in table 5.3 and the gamma/hadron separation cuts are shown in table 5.4.

The resulting significance maps from the RBM analysis are shown in figure 5.4. There are no apparent hotspots ($> 4\sigma$ for a point source candidate and $> 3.5\sigma$ for an extended source candidate) in the 600 dc point analysis (figure 5.4a)) but in the other three analyzes four hotspots (HS) were found (figure 5.4 (b)-(d)). The regions around the four hotspots were reanalyzed and zoomed-in views of the hotspots are shown in figure 5.5 (a)-(d). The locations of the hotspots and their significance values are summarized in table 5.5.

The VEGAS results from other users showed consistent results and two additional hotspots were reported. The eventdisplay analysis revealed three hotspots that were close to the VEGAS hotspots and two that were not seen in VEGAS. A summary of all the hotspots and their correspondence between the two analysis packages are shown in table 5.6.

Cut Type	MSW	MSL	Aperture
Soft/Point	(0.05, 1.23)	(0.05, 1.35)	0.014
Soft/Extended	(0.05, 1.23)	(0.05, 1.35)	0.055
Hard/Point	(0.05, 1.23)	(0.05, 1.35)	0.014
Hard/Extended	(0.05, 1.23)	(0.05, 1.35)	0.055

Table 5.4: Gamma/hadron separation cuts used in part 1 of the data set. Msl and msw are the mean scaled length and width parameters introduced in chapter 4; the bracketed values are the accepted range for the cuts on these parameters. Aperture is the radius used for the *on* region.

Analysis Sets	Gal. Coords (l, b)	Equat. Coords (J2000) (α, δ)	Signif.
Soft/Extended	(76.0, 1.9)	(304.0, 38.5)	4.56 σ
Hard/Point	(79.8, -0.1)	(308.9, 40.5)	4.16 σ
Hard/Extended	(78.3, 2.8)	(304.9, 40.8)	4.11 σ
Hard/Extended	(68.0, 0.7)	(300.0, 31.1)	3.60 σ

Table 5.5: Summary of the locations of hotspots, in both Galactic and Equatorial coordinates, and their significance values (pre-trial) as determined by the analysis used for this dissertation.

Hotspot (HS)	l	b	Eventdisplay	l	b	VEGAS
1	68.4	1.1	4.6 σ			
2	75.4	1.9	4.8 σ	76.0	1.9	4.6 σ
3 (*)				72.0	2.8	4.00 σ
4 (*)				78.0	3.6	4.00 σ
5	78.1	2.8	4.2σ	78.3	2.8	4.11σ
6	67.7	0.5	4.2σ	68.0	0.7	3.6 σ
7	77.0	2.9	4.3σ			

Table 5.6: Summary of the hotspots collated from the sky survey group based on the initial part 1 data set. The starred (*) HS were seen by other VEGAS analyzers but not by this author. HS 1 and 7 were seen in eventdisplay only. HS 2, 5 and 6 were seen in both analysis packages and their positions were quite consistent. Note that the hotspot at $l = 79.8$ and $b = -0.1$ was not included because it was deemed by the group to be a marginal candidate at that time. More data were taken near this region and the hotspot disappeared in the complete dataset.

Based on the results from these analyses, the sky survey group decided to do follow-up observations in regions near the more promising hotspots that were seen in both analysis packages, namely HS 1, 2, 4, 5, and 6 (see figure 5.6).

5.3.2 Part 2: Followup observations

Between November 2008 and December 2008, more data were taken near the promising hotspots revealed in the initial survey data set. In addition to the hotspots from part 1, new independent analysis results from both VEGAS and

eventdisplay revealed two additional hotspots. Their locations in galactic coordinates (l, b), are HS8 (80.1, 1.2) and HS9 (75.3, 0.1). The total exposure on all the hotspots is shown in figure 5.7. In addition to the survey data, additional wobble-mode data taken independently on AGILE 2021+4024 and IGR J20187+4041 (these two gamma-ray sources discovered by the AGILE and Integral telescopes are positionally coincident with one another) were also included in the data set since it overlapped with the survey region. The complete list of data runs taken during this time period and the AGILE+IGR data can be found in appendix C.

The survey data from parts 1 and 2 were again analyzed independently by members of the sky survey group using VEGAS and eventdisplay. At about the same time, VEGAS had undergone major upgrade which included improvements to various algorithms, new options to display results in Galactic coordinates and numerous bug fixes [103]. As a result, new lookup tables were produced and the quality and gamma/hadron separation cuts were re-optimized [104]. The new set of cuts used in the improved version of VEGAS are in table 5.7 and 5.8.

Cut Type	Size (d.c.)	ntubes	dist
Soft/Point	≥ 600	≥ 5	(0.05, 1.43)
Soft/Extended	≥ 600	≥ 5	(0.05, 1.43)
Hard/Point	≥ 1000	≥ 5	(0.05, 1.43)
Hard/Extended	≥ 1000	≥ 5	(0.05, 1.43)

Table 5.7: Shower reconstruction quality cuts used in parts 1 and 2 of the data set for the four separate analyzes. Size is the parameter that measures the brightness of an image (in digital counts), ntubes is the number of adjacent pixels in an image and dist is the distance of the centroid of an image to the center of the FOV.

Cut Type	MSW	MSL	Aperture
Soft/Point	(0.05, 1.06)	(0.05, 1.23)	0.013
Soft/Extended	(0.05, 1.06)	(0.05, 1.23)	0.055
Hard/Point	(0.05, 1.06)	(0.05, 1.23)	0.013
Hard/Extended	(0.05, 1.06)	(0.05, 1.23)	0.055

Table 5.8: Gamma/hadron separation cuts used in part 1 and 2 of the data set. Msl and msw are the mean scaled length and width parameters introduced in chapter 4; the bracketed values are the accepted range for the cuts on these parameters. Aperture is the radius used for the *on* region.

The significance maps from the combined data set are shown in figure 5.8 and 5.9. Table 5.9 summarizes the new significances of the hotspots from this analysis. It is clear that besides hotspots 5 and 8, all of the other candidates' significance values have decreased to a non-significant level.

Since the observing season would end in June 2009, the sky survey group decided, based on the results from parts 1 and 2, to concentrate all the remaining available observing time on the HS 5 and 8 areas.

5.3.3 Part 3: More followup observations on HS 5 and 8

During May and June 2009, more data were taken around the regions near HS 5 and 8. A total of ~ 15 hours of good quality data were taken. The complete list of runs can be found in appendix C. The complete data set from part 1, 2 and 3 was analyzed independently by different members of the sky survey group. The quality and gamma/hadron separations cuts were identical to those used in part 2. The significance maps from the complete data set are shown in figure 5.10

Hotspot (HS)	(l, b)	Significance (Part 1) (σ)	Max signif. (σ)
1	(68.4, 1.1)	4.6	2.08, 2.26, 3.18, 3.02
2	(75.4, 1.9)	4.8	2.59, 2.63, 2.50, 2.13
3	(72.0, 2.8)	4.0	3.35, 2.32, 1.98, 2.76
4	(78.0, 3.6)	4.0	2.31, 1.52, 2.32, 1.73
5	(78.3, 2.8)	4.2	4.86, 5.04, 4.33, 5.21
6	(68.0, 0.7)	4.2	2.63, 2.38, 3.32, 3.18
7	(77.0, 2.9)	4.3	1.22, 1.35, 1.41, 1.84
8	(80.1, 1.2)		4.34, 4.09, 4.54, 4.16
9	(75.3, 0.1)		3.23, 3.86, 3.42, 3.27

Table 5.9: Summary of the locations, in Galactic coordinates, and the pre-trial significance values of the nine target hotspots. The 3rd column shows the significance from part 1 of the data set. The 4th column shows the significances from the combined parts 1 and 2 of the data set with different sets of cuts (soft/point, soft/extended, hard/point and hard/extended, see tables 5.7 and 5.8 for the explanations of the terms). HS 8 and 9 did not show up in the first pass of the analysis in part 1. It is clear that beside HS 5 and 8, all other candidate hotspots do not show a statistically significant excess of gamma rays.

Hotspot (HS)	Galactic Coordinates (l, b)	Max signif. (σ)
5	(78.3, 2.8)	6.52, 6.36, 5.16, 6.69
8	(80.1, 1.2)	4.32, 4.21, 4.92, 4.50

Table 5.10: Summary of the locations, in Galactic coordinates, and the pre-trial significance values of hotspots 5 and 8 from the four different sets of cuts (soft/point, soft/extended, hard/point and hard/extended) for parts 1-3 of the data set. It is clear that the significance levels increased between part 2 of the data set and part 3 of the survey data set. Hotspots 5 and 8 are the most promising candidate gamma-ray sources revealed from the entire survey data set.

and 5.11. Table 5.10 summarizes the results from this analysis. It is clear that the significance level of both HS 5 and 8 have increased throughout the survey campaign. They represent the best candidate gamma-ray sources from the entire survey data set.

5.4 Summary

The sky survey group successfully completed 95% of the intended target region between April 2007 and June 2009, including follow-up observations on a number of promising candidates. The top right pointings in figure 5.1 (pointings 79-115) were not completed since it was deemed that follow-up observations on the hot-pots were more important. Independent analysises had shown numerous hotspots initially, but further observations eliminated all but two of the candidates, HS 5 and 8. Further discussion on these two promising candidates including their possible counterparts in other wavebands will be given in chapter 6.

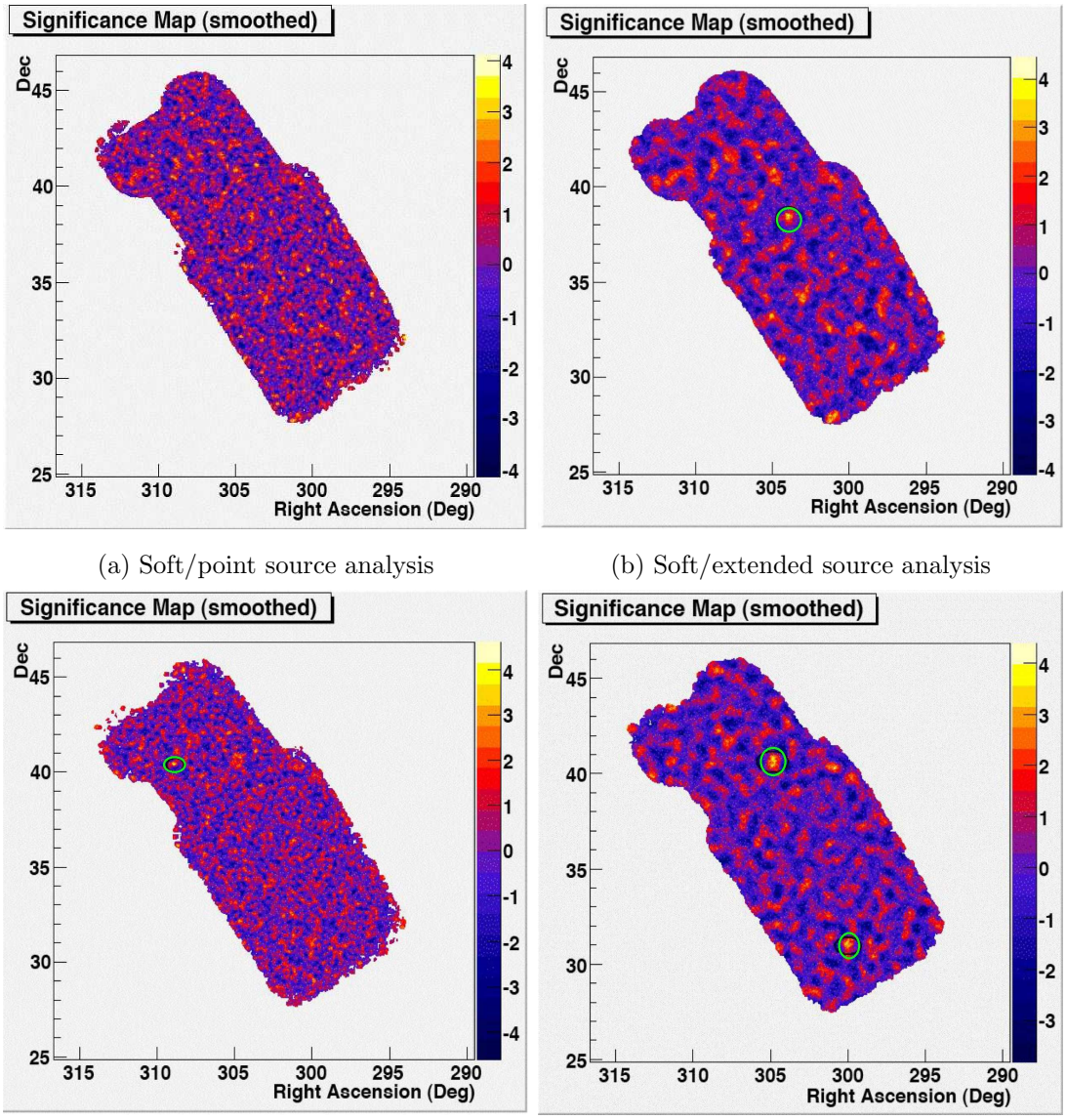

(a) Soft/point source analysis

(b) Soft/extended source analysis

(c) Hard/point source analysis

(d) Hard/extended source analysis

Figure 5.4: The significance maps in equatorial coordinates for the analysis of the part 1 data set for the four sets of cuts. There are no apparent hotspots in the soft point source analysis maps. The hotspots in other maps are green circled.

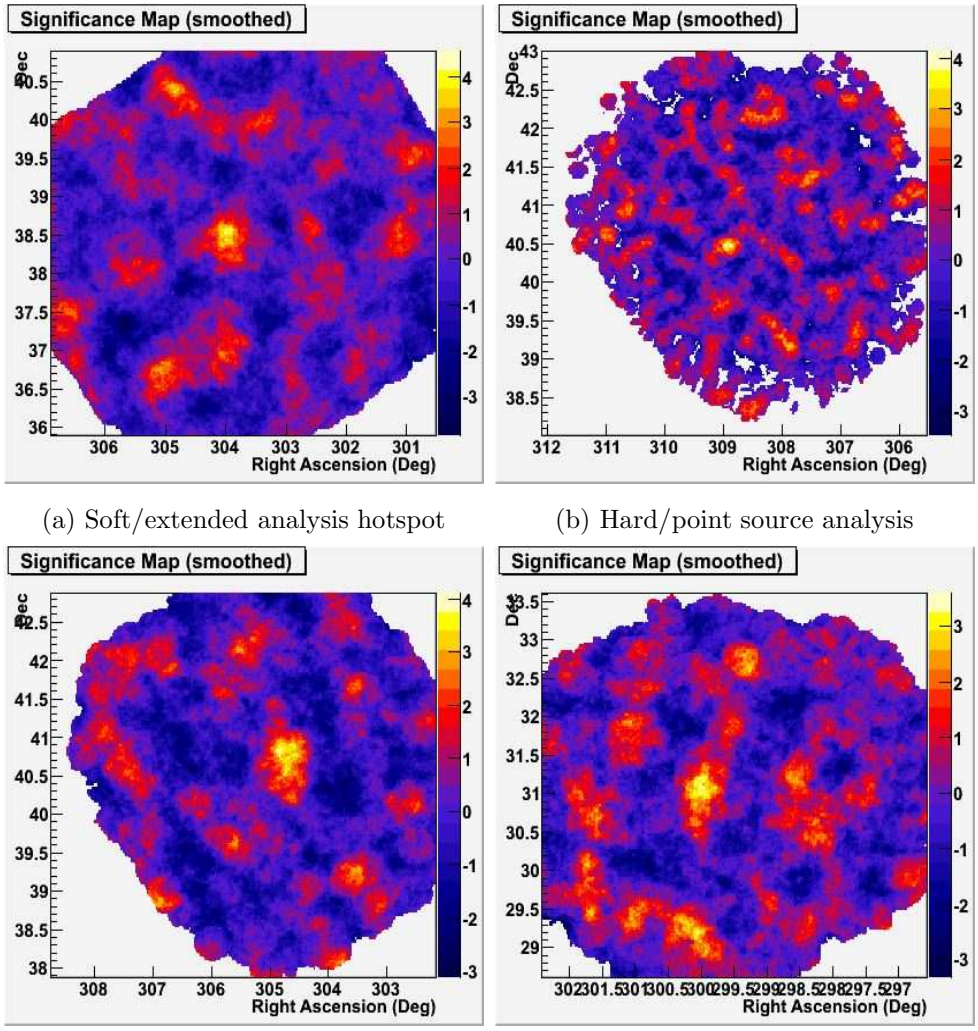

(a) Soft/extended analysis hotspot

(b) Hard/point source analysis

(c) Hard/extended source analysis hotspot 1

(d) Hard/extended source analysis hotspot 2

Figure 5.5: The blow up significance maps, in equatorial coordinates, of the four hotspots discovered in the soft/extended and the hard/point and hard/extended analysis maps of the part 1 data set.

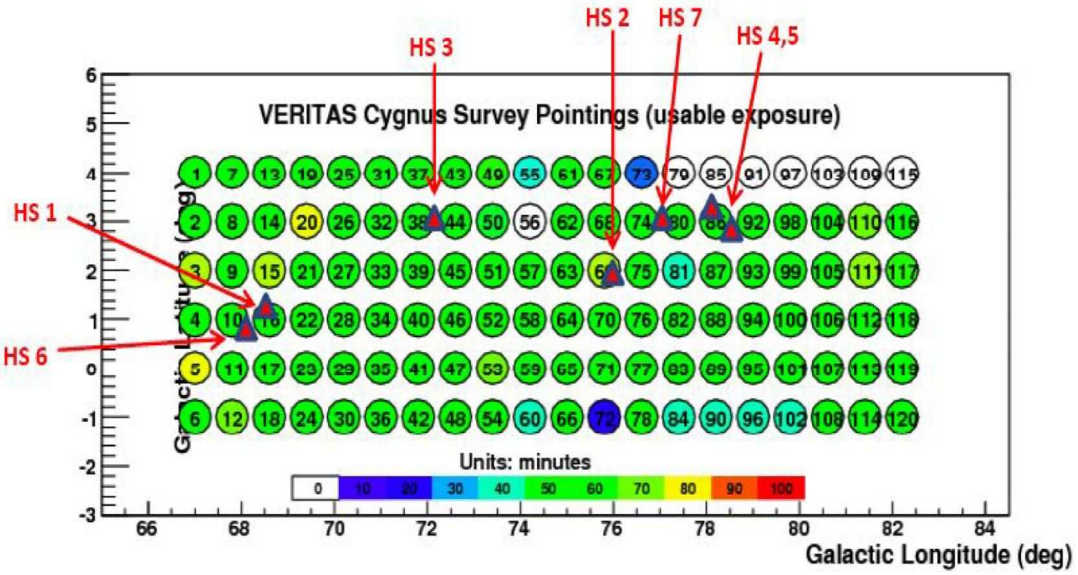

Figure 5.6: Plot showing the exposure for each grid point of the survey data taken from part 1 and the locations of the promising hotspots (in Galactic coordinates). The circles represent the positions of the pointing directions of the FOV of VERITAS. The color scale represents the total number of hours of good data taken on each pointing.

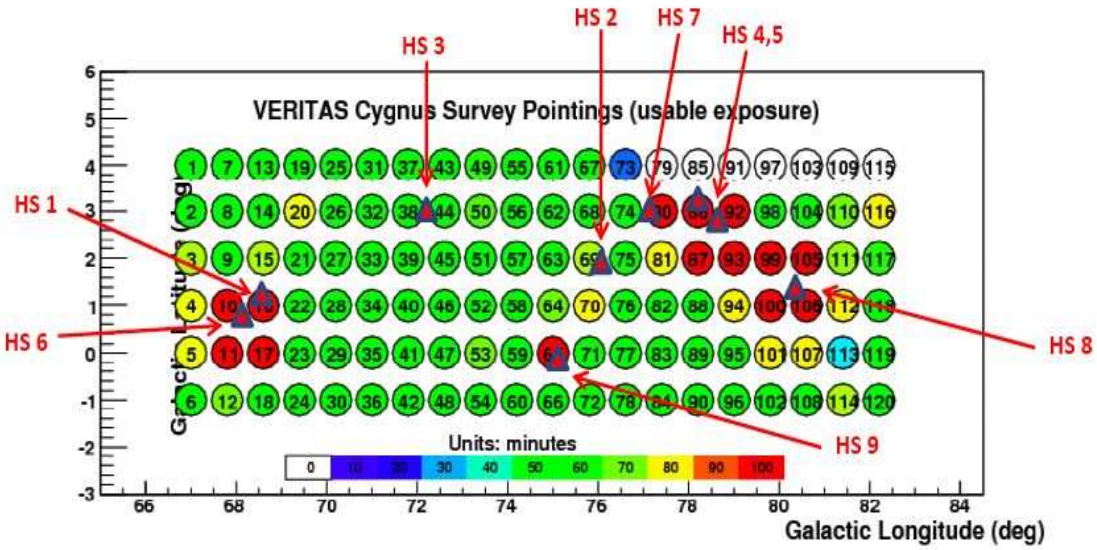

Figure 5.7: Plot showing the nine target hotspots and the total exposure for each grid point of the survey data based on parts 1 and 2 of the data set (in Galactic coordinates). The circles represents the positions of the pointing directions of the FOV of VERITAS. The color scale represents the total number of hours of good data taken on each pointing.

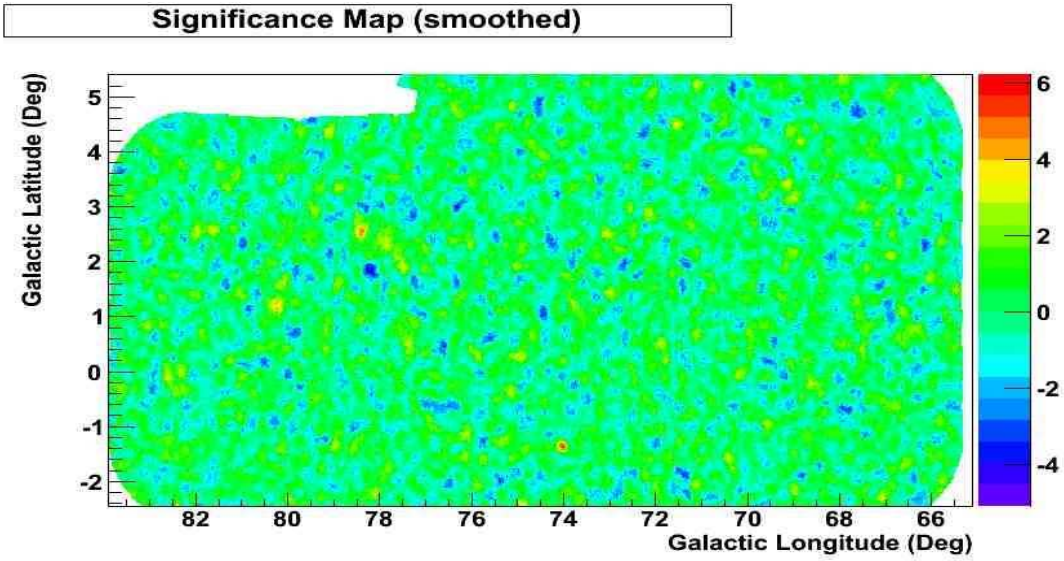

(a) Soft/point source

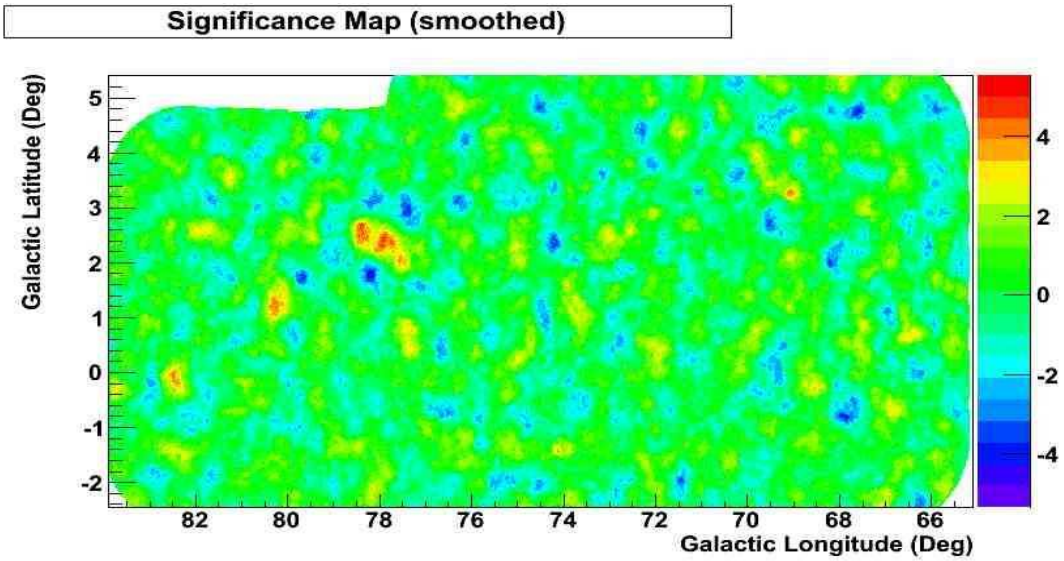

(b) Soft/extended source analysis

Figure 5.8: The significance maps of the soft (600 dc) point source and extended source analysis for parts 1 and 2 of the data set, in Galactic coordinates.

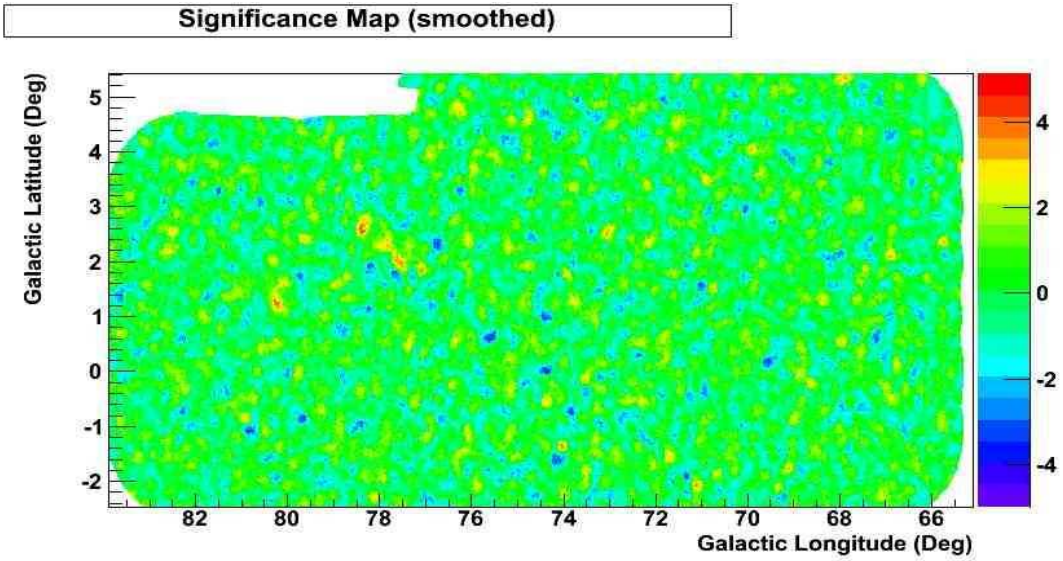

(a) Hard/point source analysis

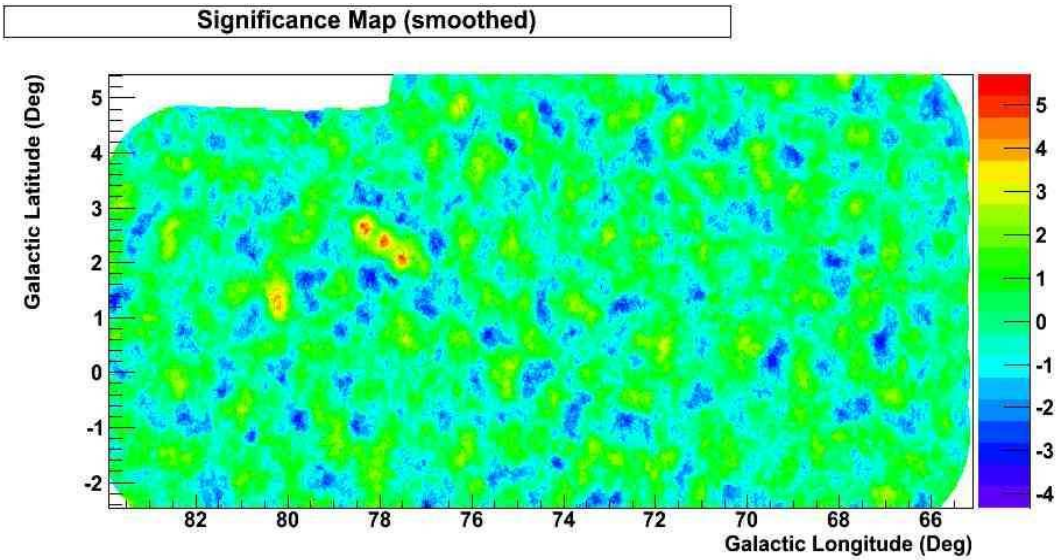

(b) Hard/extended source analysis

Figure 5.9: The significance maps of the hard (1000 dc) point source and extended source analysis for parts 1 and 2 of the data set, in Galactic coordinates.

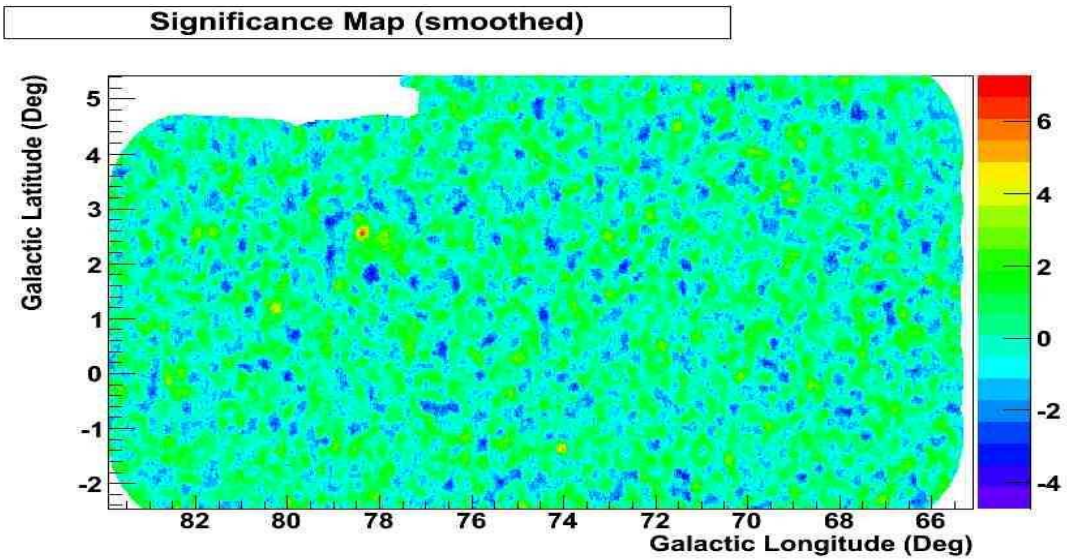

(a) Soft/point source analysis

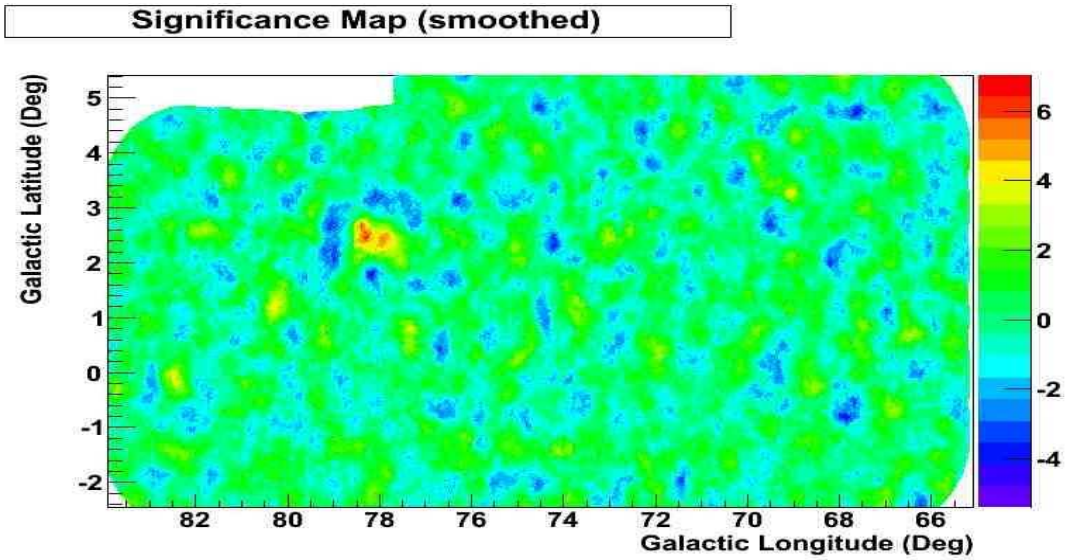

(b) Soft/extended source analysis

Figure 5.10: The significance maps of the soft (600 dc) point source and extended source analysis for the entire survey data set in Galactic coordinates.

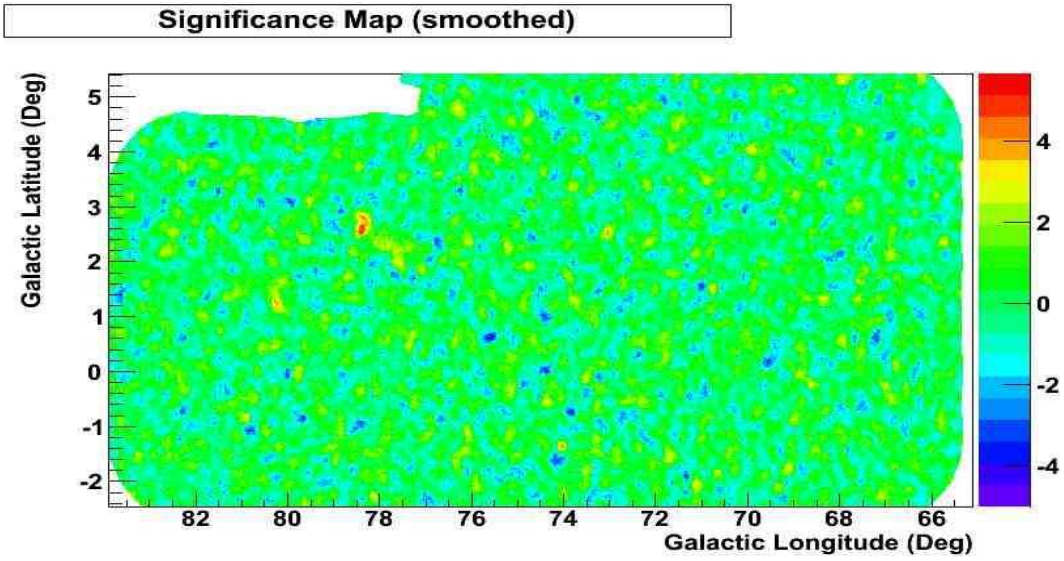

(a) Hard/point source analysis

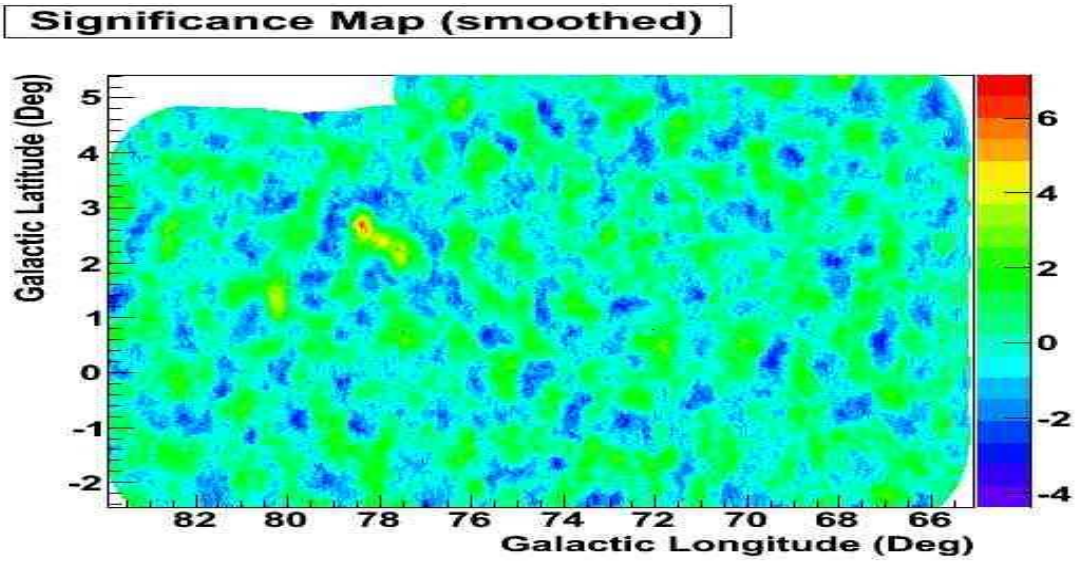

(b) Hard/extended source analysis

Figure 5.11: The significance maps of the soft (1000 dc) point source and extended source analysis for the entire survey data set in Galactic coordinates.

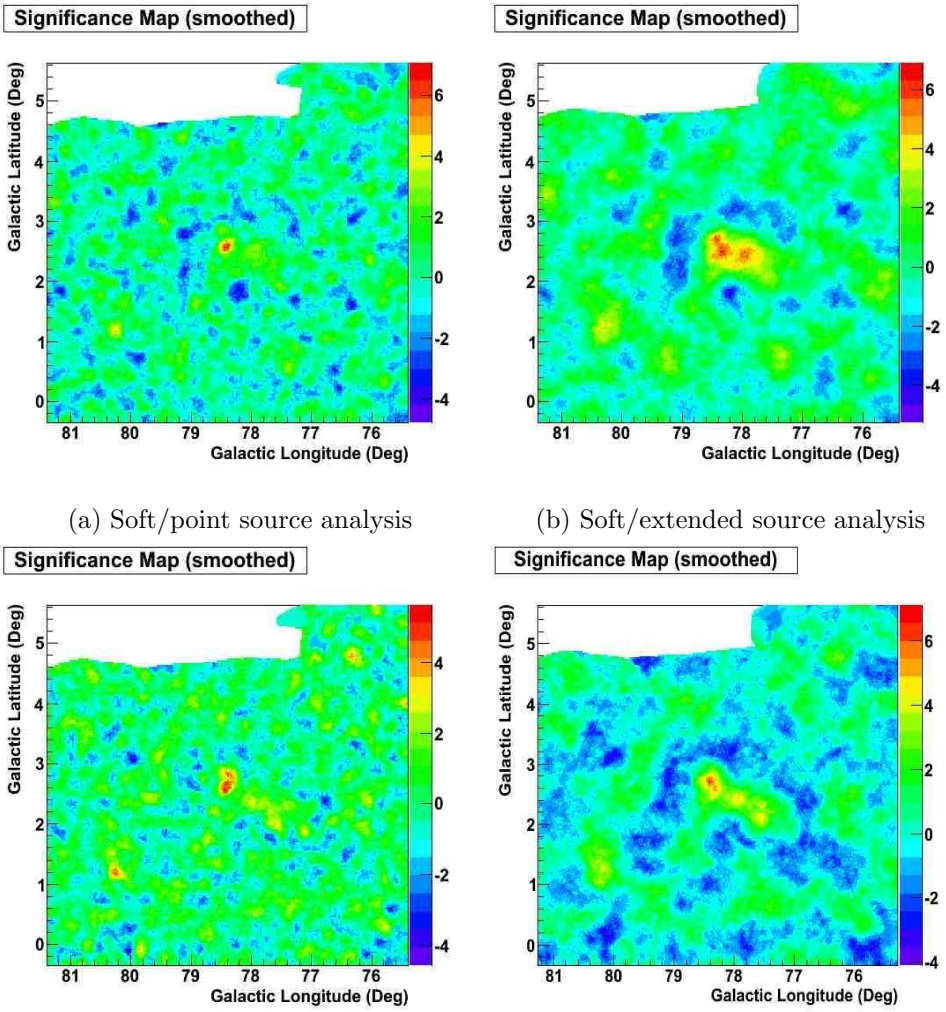

(a) Soft/point source analysis

(b) Soft/extended source analysis

(c) Hard/point source analysis

(d) Hard/extended source analysis

Figure 5.12: The significance maps for HS 5 with the four sets of cuts in Galactic coordinates. The location of the hotspot is around l=304.9, b=40.9 (l and b are Galactic longitude and latitude, respectively) and it is clear that HS 5 has an extended structure.

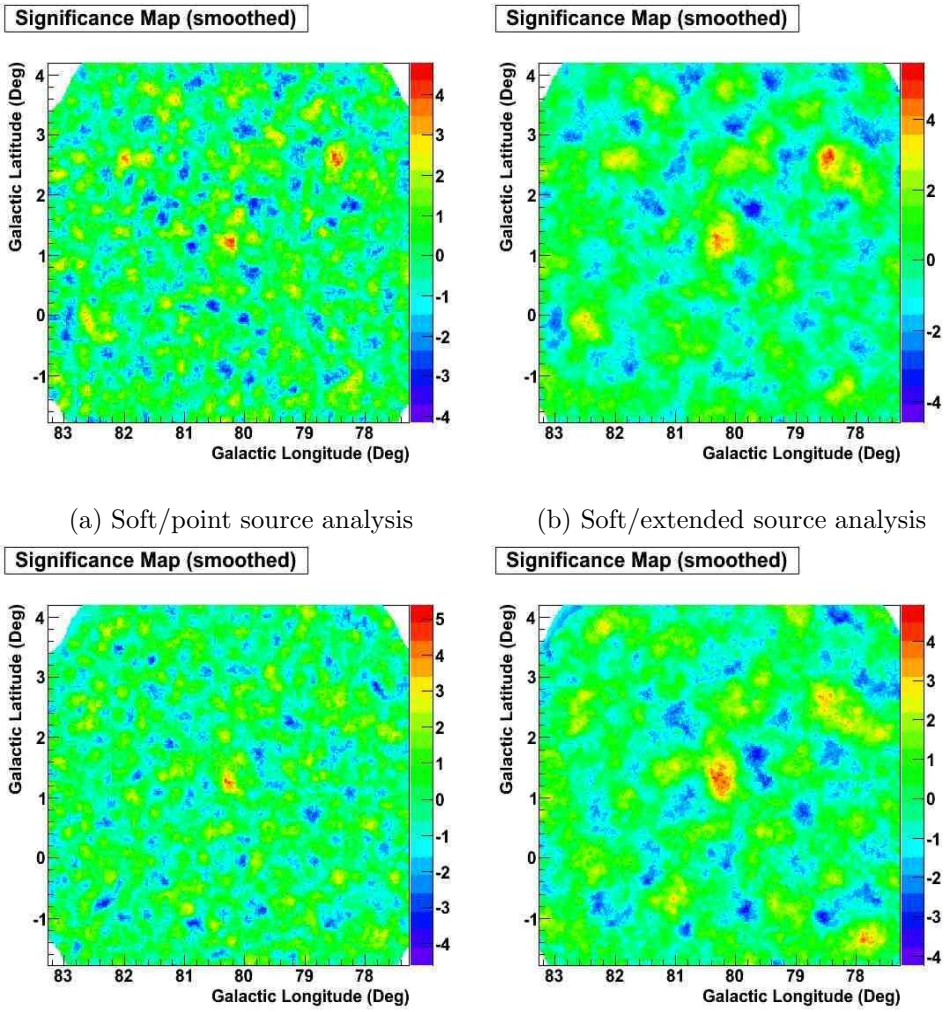

(a) Soft/point source analysis

(b) Soft/extended source analysis

(c) Hard/point source analysis

(d) Hard/extended source analysis

Figure 5.13: The significance maps for HS 8 with the four sets of cuts in Galactic coordinates. The location of the hotspot is near l=307.9, b=41.6 (l and b are Galactic longitude and latitude, respectively) and there is some evidence that HS 8 has an extended structure.

CHAPTER 6

Discussion

The two most promising hotspots that were found in the complete survey dataset are HS 5 and HS 8 (chapter 5). In this chapter, a preliminary estimate of the post-trial significance of the two hotspots will be given in section 6.1. In section 6.2, a detailed discussion of the two potential TeV sources will be given, especially their possible associations with other known astrophysical objects. Finally, a conclusion of this sky survey project and an outlook for the future is presented in section 6.3.

6.1 Trials Factor Estimation

The significance map produced by the ring background method from the survey data set contains a large number of test positions (the size of each bin is $0.025^\circ \times 0.025^\circ$ and the survey region extent is $15^\circ \times 5^\circ$, so trials positions are $\sim 140,000$). This large number of test positions increases the probability of finding a fake signal and hence the significance values of the hotspots must be corrected by a trials factor, N_{trial}. The post-trial probability, P_t, and the pre-trial probability, P, is given by the following relationship,

$$P_t = 1.0 - (1 - P)^{N_{trial}}. \tag{6.1}$$

If the bins in the significance map are uncorrelated, then the N_{trial} will be equal to the number of bins in the 2-D histogram ($\sim 140,000$). Since there exists a significant degree of correlation of bins in the *on* and off regions, the value of N_{trial} cannot be analytically determined. An estimation by Monte Carlo simulations is used instead. An outline of the procedure is as follows: (1) A 2D histogram with the same dimensions as the survey data is filled with Poisson-distributed random numbers that are consistent with a flat, no-source map. The mean of the Poisson distribution was derived from the acceptance map (see Chapter 4) of the survey data in order to accurately simulate the different exposures level within the region. (2) The histogram generated in part (1) was analyzed using the RBM like a normal data set to generate a significance map. (3) The significance map was examined to see if there was a TeV source-like signature. The process was repeated many times, (n). In step (3) above, a TeV-source like signal was taken to be ≥ 40 contiguous bins above a certain significance level (corresponding to the pre-trial probability P) , this definition is consistent with the extent of the hotspots seen in the data. Let n_{source} be the number of significance maps that contain an extended TeV source-like signal. Then the estimated post-trial probability, P_{sim}, is given by

$$P_{sim} = \frac{n_{source}}{n}. \tag{6.2}$$

Substituting P_{sim} for P_t in equation 6.1 gives the trials factor for the pre-trial probability P. We have so far managed to produce 5000 iterations of the simulations maps. The number of iterations produced is restricted by the computing time for generating and analyzing a map which roughly requires an hour per map using a 3 GHz Intel processor core. The results from the simulations are summarized in table 6.1 [104].

A naive scaling using the probability table suggest that both HS 5 and HS

Pre-trial Signi.	Single-sided Prob.	Post-trial Prob.	Post-Trial Signi.
3 σ	1.3×10^{-3}	7×10^{-2}	1.48 σ
4 σ	3.2×10^{-5}	6×10^{-3}	2.51 σ
5 σ	2.8×10^{-7}	$< 2 \times 10^{-4}$	3.35 σ

Table 6.1: Probability table showing the significance values, their corresponding single-sided Gaussian probabilities and the estimated post-trial probabilities and significance values from the simulations.

8 are at the 3 to 4 σ post-trial significance level. However the trials factor was probably over estimated since the number of simulation iterations was not large enough to produce an accurate estimate for the post-trial probability for a 5σ level source-like signal and so an upper bound was given instead. In any case, HS 5 and HS 8 are not claimed to be firm detections on the current data set.

It is important to understand if the number of hotspots that we detected in the analysis of the survey data set is consistent with what we would expect from fluctuations. If we look at the pre-trial probability of getting a 4 σ level fluctuation, then for a survey of the size that we did (140,000 bins), we would expect to see 4.5 bins that randomly exceed that threshold. In part 1 of the survey data, we reported seven hotspots, of which one (HS 5) is likely to be a true gamma-ray source. The number of hotspots is consistent with the expected number of 4 σ fluctuations, but there are difficulties with this simple comparison. First, the hotspots that we reported were not just a single bin above 4 σ, but rather a collection of bins that had excess counts. Second, the initial list of hotspots was collated from multiple independent analyses using two different analysis packages. As can be seen in table 5.6, not all hotspots were seen in

both packages and there were differences even within the same package. With the simulation work, we started to address these issues by defining what we mean by a hotspot (e.g. $\geq$40 contiguous bins above threshold) and this initial work indicates that we would expect to get at most *one* such hotspot in our survey at the 3 σ level. To fully understand the statistics of the survey, this work needs to be continued by refining and applying our definition of hotspot to the survey data itself.

6.2 Discussions of the HS5 and HS8

6.2.1 HS5

The significance map of HS 5 clearly indicates an extended structure. The core region is approximately 0.2° wide and there is a clear tail of approximate 0.5° in length (see figure 6.1 (a)). The location of HS 5 is approximately at a position $(\alpha, \delta) = (20^{\mathrm{h}}19^{\mathrm{m}}48^{\mathrm{s}}, 40°54'00'')$ or Galactic coordinates $l = 78.5°$, $b = 2.5°$, which is in the Gamma-Cygni region. The region contains the known Shell type SNR G 78.2+2.1, known as γ Cygni [106]. Radio observation has revealed the shell to be 60′ wide and the radio flux has been measured to be 340 Jy at 1 GHz which make it one of the brightest SNR in the sky at this frequency [107]. γ Cygni has long been an interesting object for gamma-ray astronomers because it is spatially consistent to the EGRET unidentified object 2EG 2020+4026/3EG 2020+4017[8]. Very recently, results from the Fermi Telescope has confirmed the EGRET source as a pulsar (0FGL J2021.5+4026/ LAT PSR J2021+4026)[108] [109].

The location of the strongest VERITAS signal is approximately 0.5° from the Fermi pulsar which suggests that the TeV emission does not likely originate from

the PWN associated with that pulsar. However the contour of the significance map overlaps with X-ray and radio contours in the region that were suggested as where the SNR shock front interacts with molecular cloudlets (figure 6.1 (b)) [107].

6.2.2 HS8

The location of HS8 is at $(\alpha, \delta) = (20^{\mathrm{h}}32^{\mathrm{m}}00^{\mathrm{s}}, 41°30'00'')$ or in Galactic coordinates $l = 80.3$, $b = 1.1$. This coincides with the location of the known VHE source TeV 2032+4130 (figure 6.2). TeV 2032 was first discovered serendipitously by the HEGRA collaboration in 2002, from their data set on the Cygnus X-3 region [34]. The source was detected later by the Whipple and MAGIC collaborations [110] [111]. The result from HEGRA indicated a source at approximately 5% Crab Nebula flux level with an angular extent of $\sim 6.2'$ and a spectral index of 1.9; MAGIC's result was consistent with these values within error. Whipple reported similar position and angular extent but a measured flux of $\sim 8\%$ Crab Nebula (see figure 6.2 (b)). The VERITAS survey also detected TeV 2032 at 6σ level pre-trial. The excess of TeV 2032 in the survey data set shows an asymmetric structure and an angular extent that is longer than that reported by HEGRA and MAGIC. A 2-dimensional Gaussian fit (assuming an asymmetric Gaussian profile) gives a fitted extent of $0.13° \pm 0.05$ in the compact direction and $0.28° \pm 0.09$ in the broader direction (figure 6.2 (a)). The position of the hotspot, either using the fitted centroid or point of maximum significance, appears to be offset by about $0.1° - 0.2°$ from the locations reported by HEGRA and MAGIC. However, given the limited data set on HS8 and the large systematic errors reported by HEGRA/MAGIC, the offset is not too significant, and it is anticipated that future follow up observations by VERITAS will resolve the true extent and location

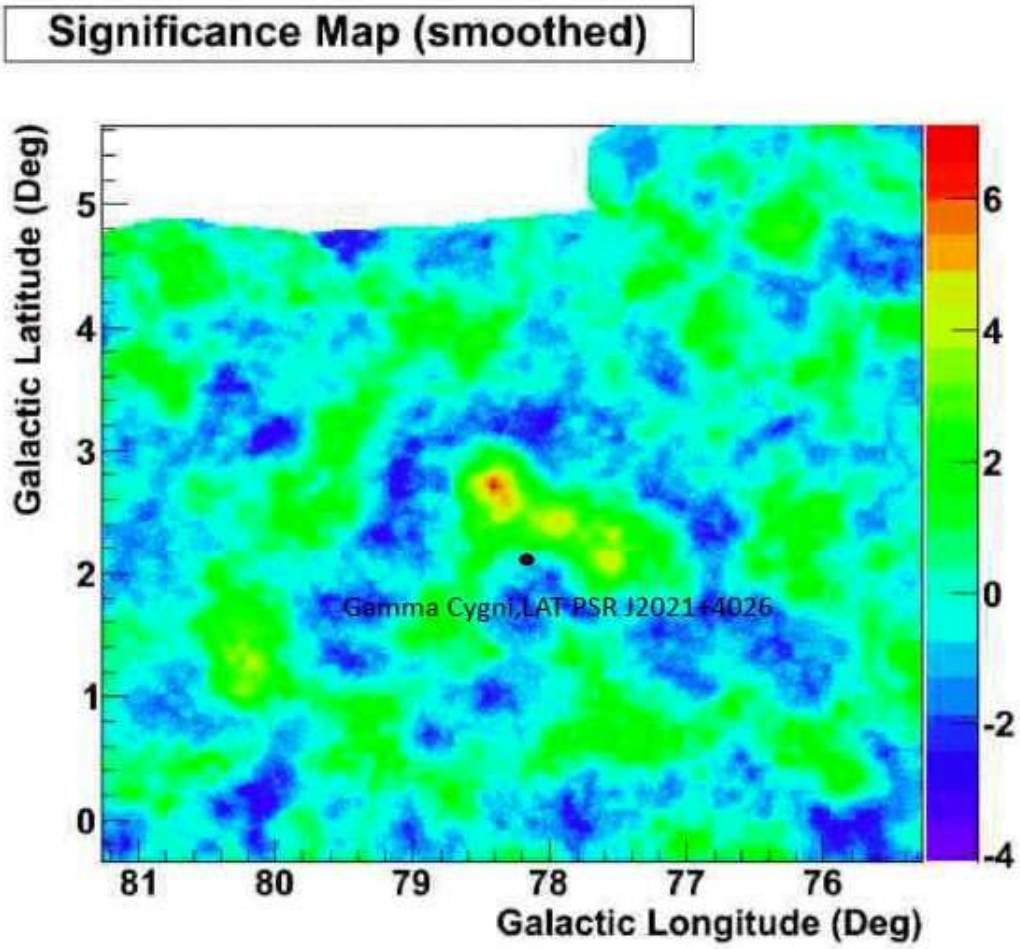

Figure 6.1: The significance map, in Galactic coordinates, of HS 5, near Gamma-Cygni from the hard/extended cut analysis. The location of the Gamma-Cygni SNR and the FERMI pulsar LAT PSR J2021+4026 (which are spatially coincident) is shown as a black dot. The hotspot has an extended structure and a visible tail.

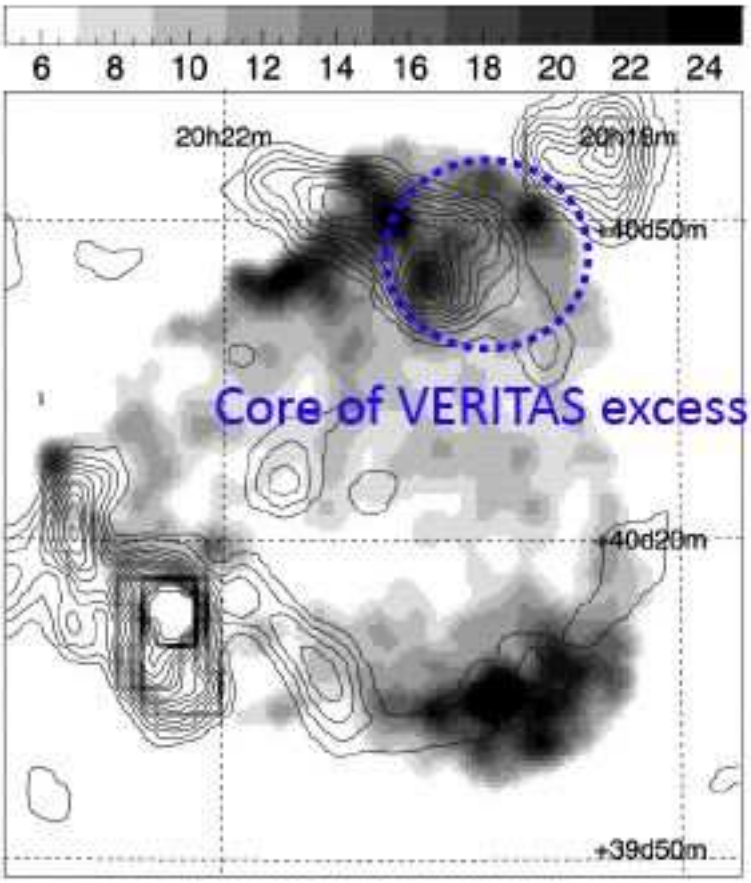

Figure 6.2: The location of the VERITAS excess overlaid on top of the X-ray emission map, adapted from [107]. The X-ray emission is represented by the gray scale with the radio contour from National Radio Astronomy Observatory (NRAO) overlaid on top of it. The VERITAS excess region is denoted by the broken blue line. the The X-ray emission has been speculated to be caused by the interaction of the SNR shock front with molecular cloudlets.

of HS 8.

TeV 2032 has long been an interesting VHE source since it is referred to as a dark accelerator, i.e. it has no known counterpart at other wavelengths. It is located in the Cygnus OB2 region, an active star-forming region, and an EGRET unidentified source 3EG J2033+4118 is located nearby (to the southwest). There has been much speculation on the acceleration mechanism of TeV 2032; for example, an unidentified microquasar counterpart has been suggested [112]. Another suggestion is that the TeV emissions comes from hadronic or leptonic interactions inside a PWN with the associated pulsar being the EGRET source [113]. This suggestion has gained support from the recent FERMI results which identified this EGRET source with a pulsar (0FGL J2032.2+4122/LAT PSR J2032+41) [108] [109].

6.3 Conclusion and outlook

The work carried out in this dissertation has shown that VERITAS is fully capable of carrying out a sky survey that is both wide field and moderately deep. The simulations and the analysis results have demonstrated that survey style data taken on many different nights can be successfully combined and that gamma-ray events can be accurately reconstructed. The survey data taken between 2007 and 2009 uncovered two very promising candidate TeV sources in the Cygnus region. Unfortunately, given the large and uncertain trials factor of the survey analysis, the two candidates are not claimed as unambiguous detections using the survey data set presented in this dissertation.

Comparing the VERITAS results to the expected number of detection extrapolated from the HESS survey (table 6.2), it can be seen that the VHE population

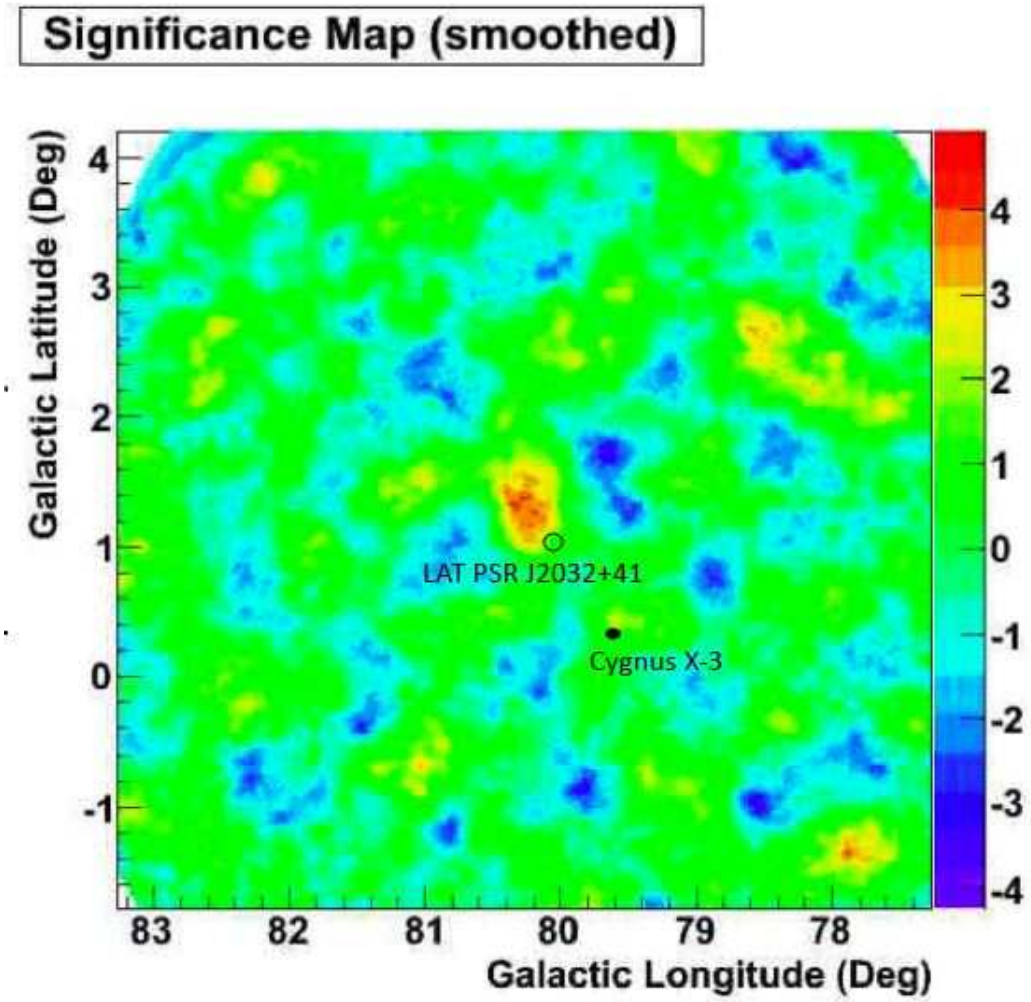

Figure 6.3: The significance map, in Galactic coordinates, of HS 8 near TeV 2032 from the hard/extended cut analysis. The locations of Cygnus X-3 and the FERMI pulsar are represented by a black dot and a black circle, respectively. The VERITAS emission has an asymmetric extended structure.

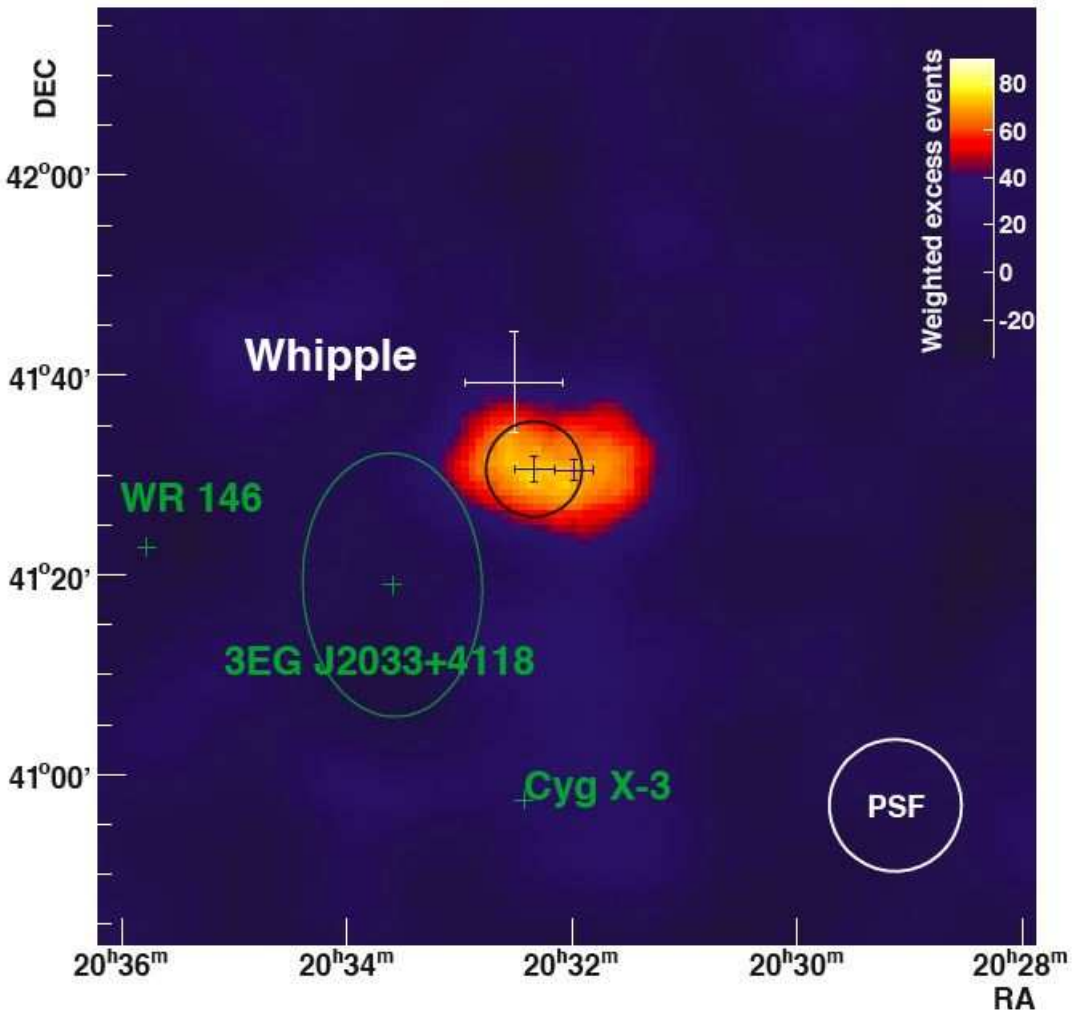

Figure 6.4: Smooth excess map of TeV 2032 [116]. The position reported by Whipple, MAGIC and HEGRA are indicated by the white cross, black cross (with 1σ width represented by the black circle) and blue cross (the one to the right inside the black circle), respectively. The green crosses indicate the positions of Cyg X-3, WR 146, and the EGRET source 3EG J2033 4118. The ellipse around the EGRET source marks the 95% confidence contour.

density in the Cygnus region is below our expectation. Additionally, the flux strengths of the VHE sources in the Cygnus region also appears to be lower than those in the inner region of the Galaxy [33]. It is not clear why the population density and the flux strengths are so different between these two regions. A possible explanation is that a different environment, e.g. density of the molecular clouds, in the inner region makes it a more favorable location for the production of VHE gamma rays than the Cygnus region.

Waveband	Catalog	HESS (discovered)	Cygnus (expected)
Radio	Green SNR	82 (25)	22 (7)
GeV γ-ray	EGRET (3EG)	14 (25)	8 (14)
X-ray	ROSAT	3932 (25)	2465 (16)
	Extrapolation		7-16

Table 6.2: Table showing an expected number of VHE gamma-ray sources in the Cygnus region, based on a comparison to the inner region of the Galaxy in three wavebands. The second column shows the catalog name: the Green SNR catalog, the EGRET 3rd catalog of GeV sources and the ROSAT catalog of X-ray sources. The third column shows the number of sources from the catalog in the inner region of the Galaxy and the bracketed number is the total number of VHE sources detected by HESS. The fourth column shows the number of sources in the VERITAS Cygnus region and the bracketed number is the expected number of VHE sources, scaled from the HESS column. The table is adapted from [117].

Given the importance of the Gamma-Cygni hotspot, 25 hours of the additional follow-up time were pre-approved for the Fall 2009 observing season. Given the extension of the hotspot, a search region of 0.25° by 0.25° around the position $20^{\mathrm{h}}19^{\mathrm{m}}48^{\mathrm{s}}, 40°54'00''$ was proposed. This region contains the location of the

strongest VERITAS signal and the entire extended structure of the hotspot. It is also the location where the hotspot contour overlaps with the X-ray and radio emission shown previously. It is expected that the additional observation time will be enough to unambiguously push the post-trial significance level above 5σ and allow the VERITAS collaboration to claim this important detection. Once the detection of this source is established, the entire data set on Gamma-Cygni hotspot can then be utilized to determine the source spectrum and morphology.

A proposal for additional observing time for the TeV 2032 hotspot was also submitted to the VERITAS time allocation committee. Given the limited data from the survey and the complicated nature of TeV 2032 where there is the possibility of multiple unresolved gamma-ray sources [115], it is important that a deep exposure on the region is achieved. Due to the extension of the source shown in the survey data set, a wobble offset of 0.7° (instead of the default 0.5° offset) is required for the observations. It is expected that an additional 20-25 hours of observing time will be sufficient to pin down the position and the morphology of the TeV 2032 hotspot and to increase the post-trial significance level to beyond the 5σ detection threshold.

Besides the proposed follow up observations on the hotspots, there are currently no plan with VERITAS to survey other Galactic regions. However, from the experience of the Cygnus region survey, there are several ways to potentially improve the results from a future survey. The first way to improve is the choice of the target region which could be chosen so that it is continuously observable by VERITAS during the normal observation season (September - June); an example is the Anti-Center region ($165^\circ \leq l \leq 195^\circ$ where l is Galactic latitude). Another improvement is to increase the area of the survey region. However, since this would increase substantially the amount of time needed, one possible com-

promise would be to decrease the exposure for each pointing and to focus on a uniform scan of the region, albeit at a lower sensitivity, and to follow up on any strong hotspots. A final alternative would be to carry out deeper survey (i.e. to $\sim$1% Crab Nebula flux level) over a smaller, but well-motivated field of view.

APPENDIX A

Survey Data Part 1

The following table shows all the data used in part 1 of the survey data set (section 5.3.1). It lists the basic information for each individual data run including the run number (run id), the survey pointing target number (see figure 5.6 or 5.7), the date the data were taken, the laser run used for calibration and the usable duration of the run.

Run Number	Pointing number	Date	Laser	Usable duration (mins)
35033	SS01	20070422	35065	20
35034	SS02	20070422	35065	20
35060	SS03	20070423	35065	18
35061	SS04	20070423	35065	20
35075	SS05	20070424	35065	18
35232	SS01	20070512	35222	20
35233	SS02	20070512	35222	20
35264	SS03	20070513	35222	20
35265	SS03	20070513	35222	17
35317	SS03	20070515	35304	20
35319	SS04	20070515	35304	20
35321	SS05	20070515	35304	20
35322	SS06	20070515	35304	19
35362	SS06	20070517	35349	20
35363	SS06	20070517	35349	20
35364	SS05	20070517	35349	20
35365	SS07	20070517	35349	20
35366	SS08	20070517	35349	20
35374	SS07	20070518	35368	20
35375	SS09	20070518	35368	20
35376	SS10	20070518	35368	20
35377	SS11	20070518	35368	20
35378	SS12	20070518	35368	10

Run Number	Pointing number	Date	Laser	Usable duration (mins)
35379	SS12	20070518	35368	20
35395	SS08	20070519	35368	19
35396	SS09	20070519	35368	20
35398	SS10	20070519	35368	20
35399	SS11	20070519	35368	20
35400	SS12	20070519	35368	20
35401	SS07	20070519	35368	20
35408	SS12	20070520	35405	20
35409	SS11	20070520	35405	20
35410	SS10	20070520	35405	20
35411	SS09	20070520	35405	20
35412	SS08	20070520	35405	20
35413	SS13	20070520	35405	20
35414	SS14	20070520	35405	20
35433	SS15	20070521	35430	15
35442	SS13	20070522	35441	20
35443	SS14	20070522	35441	20
35444	SS15	20070522	35441	20
35445	SS16	20070522	35441	20
35446	SS17	20070522	35441	20
35447	SS18	20070522	35441	20
35448	SS19	20070522	35441	20
35450	SS19	20070523	35449	20

Run Number	Pointing number	Date	Laser	Usable duration (mins)
35451	SS18	20070523	35449	20
35452	SS13	20070523	35449	20
35453	SS14	20070523	35449	20
35454	SS15	20070523	35449	20
35455	SS16	20070523	35449	20
35456	SS17	20070523	35449	20
35459	SS15	20070524	35458	20
35460	SS19	20070524	35458	20
35461	SS16	20070524	35458	20
35462	SS18	20070524	35458	20
35463	SS17	20070524	35458	20
35464	SS05	20070524	35458	20
35497	SS20	20070525	35495	20
35498	SS21	20070525	35495	20
35499	SS22	20070525	35495	20
35500	SS23	20070525	35495	20
35501	SS24	20070525	35495	20
35654	SS100	20070612	35622	20
35655	SS94	20070612	35622	20
35675	SS25	20070613	35666	20
35676	SS23	20070613	35666	20
35677	SS24	20070613	35666	20
35678	SS22	20070613	35666	20
35679	SS99	20070613	35666	19

Run Number	Pointing number	Date	Laser	Usable duration (mins)
35680	SS101	20070613	35666	20
35681	SS106	20070613	35666	20
35682	SS100	20070613	35666	20
35683	SS94	20070613	35666	20
35684	SS99	20070613	35666	20
35700	SS21	20070614	35693	20
35701	SS25	20070614	35693	20
35702	SS20	20070614	35693	19
35703	SS24	20070614	35693	20
35705	SS23	20070614	35693	20
35706	SS22	20070614	35693	20
35707	SS101	20070614	35693	20
35708	SS106	20070614	35693	20
35709	SS100	20070614	35693	20
35710	SS99	20070614	35693	19
35711	SS94	20070614	35693	20
35725	SS25	20070615	35842	12
35726	SS31	20070615	35842	20
35727	SS20	20070615	35842	20
35728	SS21	20070615	35842	20
35729	SS27	20070615	35842	20
35730	SS29	20070615	35842	20

Run Number	Pointing number	Date	Laser	Usable duration (mins)
35731	SS101	20070615	35842	20
35732	SS106	20070615	35842	20
35734	SS30	20070615	35842	20
35735	SS28	20070615	35842	20
35753	SS20	20070616	35842	20
35754	SS26	20070616	35842	13
35757	SS27	20070616	35842	20
35758	SS28	20070616	35842	19
35759	SS29	20070616	35842	20
35773	SS31	20070617	35842	20
35774	SS30	20070617	35842	20
35775	SS32	20070617	35842	20
35776	SS29	20070617	35842	20
35777	SS26	20070617	35842	20
35778	SS28	20070617	35842	20
35779	SS27	20070617	35842	20
35780	SS33	20070617	35842	20
35781	SS34	20070617	35842	20
35782	SS35	20070617	35842	20
35783	SS36	20070617	35842	20
35798	SS01	20070618	35842	20
35799	SS02	20070618	35842	20
35800	SS26	20070618	35842	20
35801	SS33	20070618	35842	20

Run Number	Pointing number	Date	Laser	Usable duration (mins)
35802	SS34	20070618	35842	20
35803	SS32	20070618	35842	20
35804	SS30	20070618	35842	20
35805	SS36	20070618	35842	20
35807	SS35	20070618	35842	20
35808	SS38	20070618	35842	20
35809	SS39	20070618	35842	20
35810	SS37	20070618	35842	20
35816	SS31	20070619	35842	20
35817	SS32	20070619	35842	20
35819	SS33	20070619	35842	20
35820	SS34	20070619	35842	20
35821	SS35	20070619	35842	20
35822	SS36	20070619	35842	20
35823	SS42	20070619	35842	20
35824	SS41	20070619	35842	20
35825	SS40	20070619	35842	20
35826	SS39	20070619	35842	19
35843	SS37	20070620	35842	12
35844	SS43	20070620	35842	20
35845	SS38	20070620	35842	20
35846	SS44	20070620	35842	20
35848	SS39	20070620	35842	20
35849	SS45	20070620	35842	20

Run Number	Pointing number	Date	Laser	Usable duration (mins)
35850	SS40	20070620	35842	20
35851	SS46	20070620	35842	20
35852	SS41	20070620	35842	20
35853	SS47	20070620	35842	20
35864	SS42	20070621	35876	12
35865	SS48	20070621	35876	20
35866	SS47	20070621	35876	20
35867	SS41	20070621	35876	20
35868	SS40	20070621	35876	20
35869	SS46	20070621	35876	20
35870	SS45	20070621	35876	20
35871	SS44	20070621	35876	20
35872	SS38	20070621	35876	20
35873	SS37	20070621	35876	20
35877	SS43	20070622	35876	20
35878	SS44	20070622	35876	20
35879	SS45	20070622	35876	20
35880	SS46	20070622	35876	10
35889	SS47	20070623	35876	18
35894	SS48	20070623	35876	20
35895	SS43	20070623	35876	20
35896	SS46	20070623	35876	10

Run Number	Pointing number	Date	Laser	Usable duration (mins)
35901	SS42	20070624	35876	19
35902	SS48	20070624	35876	20
35903	SS49	20070624	35876	19
35904	SS50	20070624	35876	10
35906	SS49	20070625	35876	20
35907	SS50	20070625	35876	20
35908	SS51	20070625	35876	20
35909	SS52	20070625	35876	20
35910	SS53	20070625	35876	20
35911	SS54	20070625	35876	20
35916	SS51	20070626	35876	20
35918	SS52	20070626	35876	20
35919	SS53	20070626	35876	20
36427	SS49	20070914	36448	08
36431	SS49	20070914	36448	20
36432	SS50	20070914	36448	19
36433	SS51	20070914	36448	17
36435	SS52	20070914	36448	20
36436	SS53	20070914	36448	20
36438	SS54	20070914	36448	20
36474	SS53	20070915	36480	10
36478	SS54	20070915	36480	12
36538	SS55	20070918	36533	19

Run Number	Pointing number	Date	Laser	Usable duration (mins)
36584	SS57	20070919	36601	15
36585	SS58	20070919	36601	18
36586	SS59	20070919	36601	20
36743	SS58	20071005	36721	20
36744	SS57	20071005	36721	20
36885	SS61	20071008	36904	20
36886	SS62	20071008	36904	20
36887	SS63	20071008	36904	20
36888	SS64	20071008	36904	18
36889	SS65	20071008	36904	20
36941	SS61	20071009	36904	19
36942	SS62	20071009	36904	20
36973	SS63	20071010	37008	20
36974	SS64	20071010	37008	12
37016	SS61	20071011	37034	20
37017	SS62	20071011	37034	19
37018	SS63	20071011	37034	20
37019	SS64	20071011	37034	20
37055	SS55	20071012	37090	20
37061	SS65	20071012	37090	20

Run Number	Pointing number	Date	Laser	Usable duration (mins)
37062	SS65	20071012	37090	20
37103	SS66	20071013	37148	20
37104	SS67	20071013	37148	20
37106	SS68	20071013	37148	20
37107	SS69	20071013	37148	20
37108	SS66	20071013	37148	20
37160	SS66	20071014	37177	20
37161	SS67	20071014	37177	20
37162	SS68	20071014	37177	20
37163	SS69	20071014	37177	18
37164	SS67	20071014	37177	19
37202	SS68	20071015	37228	20
37203	SS69	20071015	37228	16
37204	SS69	20071015	37228	20
37206	SS70	20071015	37228	20
37208	SS71	20071015	37228	20
37209	SS70	20071015	37228	20
37236	SS70	20071016	37263	20
37237	SS71	20071016	37263	20
37238	SS72	20071016	37263	20

Run Number	Pointing number	Date	Laser	Usable duration (mins)
37239	SS73	20071016	37263	20
37277	SS71	20071017	37296	20
37672	SS57	20071107	37668	12
37673	SS58	20071107	37668	17
37674	SS59	20071107	37668	18
37708	SS73	20071108	37742	06
37749	SS75	20071109	37780	20
37750	SS76	20071109	37780	20
37751	SS81	20071109	37780	20
37752	SS82	20071109	37780	20
37753	SS87	20071109	37780	20
37816	SS75	20071111	37845	10
37818	SS75	20071111	37845	20
37819	SS76	20071111	37845	20
37891	SS76	20071113	37920	20
37892	SS81	20071113	37920	20
37893	SS82	20071113	37920	20
37894	SS87	20071113	37920	19
37929	SS59	20071114	37955	20
41200	SS87	20080607	41195	20
41201	SS93	20080607	41195	20

Run Number	Pointing number	Date	Laser	Usable duration (mins)
41202	SS82	20080607	41195	20
41203	SS75	20080607	41195	10
41216	SS77	20080608	41195	20
41219	SS83	20080608	41195	20
41220	SS89	20080608	41195	20
41228	SS88	20080609	41195	20
41229	SS93	20080609	41195	20
41230	SS95	20080609	41195	20
41231	SS105	20080609	41195	20
41232	SS107	20080609	41195	20
41242	SS77	20080610	41249	20
41243	SS83	20080610	41249	20
41244	SS88	20080610	41249	20
41245	SS89	20080610	41249	20
41246	SS95	20080610	41249	20
41247	SS105	20080610	41249	20
41248	SS107	20080610	41249	20
41259	SS77	20080611	41252	20
41260	SS83	20080611	41252	20
41261	SS89	20080611	41252	20
41262	SS95	20080611	41252	20
41263	SS88	20080611	41252	20

Run Number	Pointing number	Date	Laser	Usable duration (mins)
41493	SS105	20080922	41488	20
41494	SS107	20080922	41488	20
41495	SS74	20080922	41488	20
41496	SS80	20080922	41488	20
41497	SS86	20080922	41488	20
41498	SS92	20080922	41488	20
41523	SS74	20080923	41521	20
41524	SS80	20080923	41521	20
41525	SS86	20080923	41521	20
41526	SS92	20080923	41521	20
41527	SS74	20080923	41521	20
41528	SS113	20080923	41521	20
41529	SS114	20080923	41521	20
41556	SS80	20080924	41550	20
41557	SS86	20080924	41550	20
41558	SS92	20080924	41550	20
41559	SS98	20080924	41550	20
41560	SS104	20080924	41550	20
41561	SS110	20080924	41550	10
41594	SS110	20080925	41593	20

Run Number	Pointing number	Date	Laser	Usable duration (mins)
41595	SS116	20080925	41593	20
41596	SS98	20080925	41593	20
41597	SS104	20080925	41593	20
41598	SS110	20080925	41593	20
41599	SS116	20080925	41593	20
41600	SS98	20080925	41593	20
41706	SS104	20080928	41674	20
41707	SS110	20080928	41674	20
41708	SS116	20080928	41674	20
41709	SS111	20080928	41674	12
41711	SS112	20080928	41674	20
41712	SS111	20080928	41674	20
41900	SS114	20081002	41898	20
41901	SS111	20081002	41898	20
41902	SS112	20081002	41898	20
41903	SS113	20081002	41898	15
41938	SS114	20081003	41898	14
41939	SS120	20081003	41898	20
42012	SS117	20081006	41898	16

Table A.1: The table of all the data runs used in part 1 of the survey analysis.

APPENDIX A

Survey Data Part 2

The following table shows all the data used in part 2 of the survey data set (section 5.3.2) and the auxiliary data from wobble-mode observations taken on IGR J20187+4041 and AGILE 2021+4024. It lists the basic information for each individual data run including the run number (run id), the survey pointing target number (see figure 5.6 or 5.7), the date the data were taken, the laser run used for calibration and the usable duration of the run.

Run Number	Pointing number	Date	Laser	Usable duration (mins)
40565	IGR J20187+4041	20080429	40355	20
40566	IGR J20187+4041	20080429	40355	20
40595	IGR J20187+4041	20080430	40355	20
40596	IGR J20187+4041	20080430	40355	20
40598	IGR J20187+4041	20080430	40355	20
40621	IGR J20187+4041	20080501	40355	20
40622	IGR J20187+4041	20080501	40355	20
40623	IGR J20187+4041	20080501	40355	20
40651	IGR J20187+4041	20080502	40355	20
40652	IGR J20187+4041	20080502	40355	11
40654	IGR J20187+4041	20080502	40355	20
40692	AGILE 2021+4024	20080503	40355	20
40693	AGILE 2021+4024	20080503	40355	20
40694	AGILE 2021+4024	20080503	40355	20
40743	AGILE 2021+4024	20080505	40355	20
40744	AGILE 2021+4024	20080505	40355	19
40746	AGILE 2021+4024	20080505	40355	20
40747	AGILE 2021+4024	20080505	40355	20
40766	AGILE 2021+4024	20080506	40355	20
40767	AGILE 2021+4024	20080506	40355	20
40768	AGILE 2021+4024	20080506	40355	20
40769	AGILE 2021+4024	20080506	40355	20

Run Number	Pointing number	Date	Laser	Usable duration (mins)
42012	SS117	20081006	41898	16
42189	SS111	20081018	42187	20
42190	SS112	20081018	42187	20
42205	SS114	20081019	42203	20
42206	SS117	20081019	42203	20
42207	SS118	20081019	42203	20
42208	SS119	20081019	42203	20
42217	SS117	20081020	42215	20
42218	SS118	20081020	42215	20
42219	SS119	20081020	42215	20
42220	SS120	20081020	42215	20
42221	SS78	20081020	42215	20
42222	SS84	20081020	42215	20
42240	SS90	20081021	42215	20
42241	SS96	20081021	42215	20
42242	SS102	20081021	42215	20
42243	SS108	20081021	42215	20
42244	SS117	20081021	42215	10
42245	SS118	20081021	42215	20
42246	SS119	20081021	42215	20
42284	SS108	20081022	42276	20

Run Number	Pointing number	Date	Laser	Usable duration (mins)
42285	SS78	20081022	42276	20
42336	SS84	20081023	42346	20
42337	SS90	20081023	42346	20
42338	SS96	20081023	42346	20
42339	SS102	20081023	42346	20
42342	SS78	20081023	42346	20
42343	SS108	20081023	42346	20
42344	SS120	20081023	42346	20
42376	SS60	20081024	42382	20
42377	SS60	20081024	42382	20
42378	SS72	20081024	42382	20
42379	SS72	20081024	42382	20
42380	SS84	20081024	42382	20
42381	SS102	20081024	42382	20
42415	SS50	20081025	42433	20
42416	SS56	20081025	42433	20
42417	Cygnus HS2	20081025	42433	20
42418	Cygnus HS2	20081025	42433	20
42419	Cygnus HS2	20081025	42433	20
42420	Cygnus HS2	20081025	42433	20
42421	SS90	20081025	42433	20

Run Number	Pointing number	Date	Laser	Usable duration (mins)
42451	SS56	20081026	42460	20
42452	Cygnus HS2	20081026	42460	20
42453	Cygnus HS2	20081026	42460	20
42454	Cygnus HS2	20081026	42460	20
42455	Cygnus HS2	20081026	42460	20
42456	SS96	20081026	42460	20
42489	SS55	20081027	42500	20
42490	Cygnus HS2	20081027	42500	20
42491	Cygnus HS2	20081027	42500	20
42492	Cygnus HS2	20081027	42500	20
42493	Cygnus HS2	20081027	42500	20
42494	Cygnus HS2	20081027	42500	20
42525	SS81	20081028	42547	20
42526	SS56	20081028	42547	20
42527	SS65	20081028	42547	20
42528	SS65	20081028	42547	20
42529	SS60	20081028	42547	20
42530	SS86	20081028	42547	20
42573	SS87	20081029	42594	20
42574	SS92	20081029	42594	19

Run Number	Pointing number	Date	Laser	Usable duration (mins)
42575	SS80	20081029	42594	10
42607	SS86	20081030	42635	08
42608	SS87	20081030	42635	08
42609	SS92	20081030	42635	20
42610	SS80	20081030	42635	19
42611	SS93	20081030	42635	20
42642	SS86	20081031	42666	20
42645	SS87	20081031	42666	20
42646	SS92	20081031	42666	20
42647	SS80	20081031	42666	20
42648	SS93	20081031	42666	20
42681	SS11	20081101	42696	18
42682	SS16	20081101	42696	10
42683	SS17	20081101	42696	18
42684	SS04	20081101	42696	20
42718	SS10	20081102	42738	20
42719	SS10	20081102	42738	20
42720	SS11	20081102	42738	20
42721	SS116	20081102	42738	20
42722	SS16	20081102	42738	18

Run Number	Pointing number	Date	Laser	Usable duration (mins)
42782	SS11	20081104	42799	12
42783	SS16	20081104	42799	18
42784	SS17	20081104	42799	20
42785	SS10	20081104	42799	20
42786	SS100	20081104	42799	20
42976	SS100	20081116	42981	20
42978	SS106	20081116	42981	20
42979	SS99	20081116	42981	20
42980	SS105	20081116	42981	20
42986	SS100	20081117	41898	20
42987	SS106	20081117	41898	20
42988	SS99	20081117	41898	20
42989	SS105	20081117	41898	20
43023	SS86	20081118	41858	19
43024	SS87	20081118	41858	20
43025	SS92	20081118	41858	20
43026	SS80	20081118	41858	20
43067	SS100	20081119	41858	20
43072	SS106	20081119	41858	20
43073	SS99	20081119	41858	20

Run Number	Pointing number	Date	Laser	Usable duration (mins)
43074	SS105	20081119	41858	20
43111	SS86	20081120	43127	16
43112	SS87	20081120	43127	20
43113	SS92	20081120	43127	17
43114	SS80	20081120	43127	20
43142	SS80	20081121	43163	20
43143	SS86	20081121	43163	16
43144	SS92	20081121	43163	20
43145	SS87	20081121	43163	20
43176	SS65	20081122	43199	20
43236	SS86	20081124	43264	10
43237	SS112	20081124	43264	20
43238	SS101	20081124	43264	20
43239	SS107	20081124	43264	20
43344	SS86	20081201	43357	20
43381	SS81	20081202	43387	20
43446	SS106	20081204	43457	20

Table A.1: The table of all the data runs used in part 1 of the survey analysis.

APPENDIX A

Survey Data Part 3

The following table shows all the data used in part 3 of the survey data set (section 5.3.3) which consists of follow-up observations on Hotspots 5 and 8. It lists the basic information for each individual data run including the run number (run id), the survey pointing target number (see figure 5.6 or 5.7), the date the data were taken, the laser run used for calibration and the usable duration of the run.

Run Number	Pointing number	Date	Laser	Usable duration (mins)
46113	gamma cygni hot spot	20090524	46101	13
46114	gamma cygni hot spot	20090524	46101	20
46115	gamma cygni hot spot	20090524	46101	20
46116	gamma cygni hot spot	20090524	46101	20
46117	gamma cygni hot spot	20090524	46101	20
46132	gamma cygni hot spot	20090525	46126	20
46133	gamma cygni hot spot	20090525	46126	20
46134	gamma cygni hot spot	20090525	46126	19
46153	gamma cygni hot spot	20090526	46141	20
46154	gamma cygni hot spot	20090526	46141	20
46155	gamma cygni hot spot	20090526	46141	20
46170	gamma cygni hot spot	20090527	46165	20
46171	gamma cygni hot spot	20090527	46165	20
46172	gamma cygni hot spot	20090527	46165	20
46214	gamma cygni hot spot	20090529	46213	20
46215	gamma cygni hot spot	20090529	46213	20
46216	gamma cygni hot spot	20090529	46213	11
46236	gamma cygni hot spot	20090530	46230	20
46237	gamma cygni hot spot	20090530	46230	20
46238	gamma cygni hot spot	20090530	46230	20

Run Number	Pointing number	Date	Laser	Usable duration (mins)
46239	gamma cygni hot spot	20090530	46230	20
46251	gamma cygni hot spot	20090531	46245	20
46252	gamma cygni hot spot	20090531	46245	20
46253	gamma cygni hot spot	20090531	46245	16
46261	gamma cygni hot spot	20090601	46263	19
46262	gamma cygni hot spot	20090601	46263	20
46273	gamma cygni hot spot	20090602	46268	13
46274	gamma cygni hot spot	20090602	46268	17
46282	gamma cygni hot spot	20090603	46278	20
46283	gamma cygni hot spot	20090603	46278	20
46286	gamma cygni hot spot	20090604	46285	17
46287	gamma cygni hot spot	20090604	46285	16
46463	gamma cygni hot spot	20090621	46442	19
46464	gamma cygni hot spot	20090621	46442	20
46482	gamma cygni hot spot	20090622	46465	20
46483	gamma cygni hot spot	20090622	46465	20
46484	gamma cygni hot spot	20090622	46465	20
46485	gamma cygni hot spot	20090622	46465	18
46486	gamma cygni hot spot	20090622	46465	20
46488	gamma cygni hot spot	20090622	46465	19
46520	gamma cygni hot spot	20090624	46503	11
46523	gamma cygni hot spot	20090624	46503	20
46524	gamma cygni hot spot	20090624	46503	20

References

[1] R. Browning, D. Ramsden, P. J. Wright, *Nature, 232, 99 (1971).*

[2] B. Parlier et al., *Nature Physical Science, 242, 117 (1973).*

[3] B. McBreen et al., *ApJ, 184, 571 (1973).*

[4] W. Kraushaar et al., *ApJ, 141, 845 (1965).*

[5] G. W. Clark, G. P. Garmire, W. L. Kraushaar, *ApJ, 153, 203 (1968).*

[6] "http://heasarc.gsfc.nasa.gov/docs/cgro/cgro/".

[7] G. Kanbach et al., *Space Sci. Rev., 49 (1988).*

[8] R. C. Hartman et al., *ApJS, 123, 79202, July (1999).*

[9] C. M. Urry, P. Padovani, *Proceedings of the Astronomical Society of the Pacific, 107, 803, September (1995).*

[10] "http://www.nasa.gov/".

[11] "http://gammaray.msfc.nasa.gov/gbm/".

[12] P.M. Saz Parkinson, M. Dormody, M. Ziegler, *Proceedings of the 31st ICRC, Lodz, Poland, 7, July (2009).*

[13] W. Galbraith, *Nature, 171, 349 (1953).*

[14] W. Galbraith, J. Jelley, *Journal of Atmospheric and Terrestrial Physics, 6, 250 (1955).*

[15] T. C. Weekes, K. E. Turver, *Proc. 12th ESLAB Symp. (1977).*

[16] T. C. Weekes et al., *ApJ, 342, 379 (1989).*

[17] *Rossijskaya Akademiya Nauk, Izvestiya, Seriya Fizicheskaya (ISSN 0367-6765), 57, 4, 174 (1993).*

[18] "http://www.mpi-hd.mpg.de/hfm/CT/CT.html".

[19] V. G. Sinitsyna, *Detector-II, 91 (1993).*

[20] J. Barrau et al., *Nuclear Instruments and Methods A, 416, 278 (1998).*

[21] P. Armstrong et al., *Nuclear Instruments and Methods in Physics Research A, 527, 411 (2004).*

[22] B. M. Vladimirsky et al., *Very High Energy Gamma Ray Astronomy, 21 (1988).*

[23] "http://www.mpi-hd.mpg.de/hfm/HESS/".

[24] "http://magic.mppmu.mpg.de/".

[25] "http://icrhp9.icrr.u-tokyo.ac.jp/".

[26] J. M. Davies, E.S. Cotton, *J. Solar Energy Sci. and Eng., 1, 16 (1957).*

[27] M. Punch et al., *Nature, 358, 477 (1992).*

[28] J. Quinn et al., *ApJ, 456, 83 (1996).*

[29] M. Catanese et al., *ApJ, 501, 616 (1998).*

[30] D. Horan et al., *ApJ, 571, 753 (2002).*

[31] K.Kosacket al., *ApJ, 608, 97 (2004).*

[32] G. Puhlhofer et al., *Astroparticle Physics, 20, 267 (2003).*

[33] F. Aharonian et al., *A&A, 370, 112 (2001).*

[34] F. Aharonian et al., *A&A, 393, 37 (2002).*

[35] F. Aharonian et al., *A&A, 403, 1 (2003).*

[36] R. Enomoto et al., *International Cosmic Ray Conference, 359 (2005).*

[37] D. Paneque, H. J. Gebauer, E. Lorenz, R. Mirzoyan, *Nuclear Instruments and Methods in Physics Research A, 518, 619 (2004).*

[38] C. E. Baixeras, *International Cosmic Ray Conference, 227 (2005).*

[39] A. J. Smith, *Presented in International Cosmic Ray Conference (2005)* .

[40] "http://www.lanl.gov/milagro/concept.shtml".

[41] G. Sinnis, *AIP Conf. Proc. 745: High Energy Gamma-Ray Astronomy, 234 (2005).*

[42] D. A. Smith et al., *Nuclear Physics B Proceedings Supplements, 54, 362 (1997).*

[43] D. Bhattacharya et al., *AIP Conf. Proc. 410: Proceedings of the Fourth Compton Symposium, 1626 (1997).*

[44] F. Arqueros et al., *International Cosmic Ray Conference, 2399 (2001).*

[45] J. Zweerink et al., *Proc. SPIE, 3765, 524 (1999).*

[46] M. Garcia-Munoz, G. M. Mason, J. A. Simpson, *Astrophys. J., 217, 859 (1977)* .

[47] S. Funk, *PhD Thesis (2005).*

[48] J.A. Simpson, *Annu. Rev. Nucl. Part. Sci., 33, 323 (1983).*

[49] E. Fermi, *Phys. Rev., 75, 1169 (1949).*

[50] R. D. Blandford, J. P. Ostriker, *Astrophys J., 221, 29 (1978).*

[51] M. S. Longair, *High energy astrophysics, Vol. 2, Cambridge university press (1994).*

[52] R. A. Chevalier, *Ann. Rev. Astron. Astrophys. 15, 175 (1977).*

[53] F. Aharonian et al., *A&A, 481, 401 (2008).*

[54] J. Albert et al., *ApJ, 664, 87 (2007).*

[55] G. E. Romero, G. S. Vila, *Astronomy and astrophysics., 485, Issue 3, 623 (2008).*

[56] W. Bednarek, *Monthly Notices of the Royal Astronomical Society, 397, 1420 (2009)* .

[57] F. Aharonian et al., *Science, 309, 746 (2005).*

[58] V. A. Acciari et al., *ApJ, 679, 1427 (2008).*

[59] F. Aharonian et al., *A&A, 431, 197 (2005)*

[60] A. A. Abdo et al., *ApJ, 658, 33 (2007).*

[61] A. A. Abdo et al., *ApJ, 664, 91 (2007).*

[62] F. Aharonian et al., *ApJ, 636, 777 (2006).*

[63] F. Aharonian et al., *A&A, 499, 723 (2009).*

[64] ROSAT X-ray Catalog.

[65] "http://www.atnf.csiro.au/research/pulsar/psrcat/".

[66] "http://www.mrao.cam.ac.uk/surveys/snrs/".

[67] "http://vizier.u-strasbg.fr/viz-bin/VizieR?-source=J/A+A/455/1165".

[68] "http://fermi.gsfc.nasa.gov/science/resources/docs/vwp/".

[69] J. D. Jackson, *Classical Electrodynamics 3 ed. (1998).*

[70] S. Gammell, *PhD Thesis (2004).*

[71] J. V. Jelley, *Cerenkov Radiation and its applications. Pergamon Press (1958).*

[72] "http://www.sadjadi.org/Cerenkov/theory.htm".

[73] I. de la Calle Perez, *PhD Thesis (2003)*

[74] D.Halliday, R. Resnick, J. Walker, *Fundamentals of Physics, 8 ed. (2007).*

[75] S. Fegan, *PhD Thesis (2004).*

[76] A.M. Hillas, *Proc. 19th Int. Cosmic Ray Conf., La Jolla, 3, 445 (1985).*

[77] J. V. Jelley, N. A. Porter, *QJRAS, 4, 275, September (1963).*

[78] "http://veritas.sao.arizona.edu/".

[79] R. J. White, *AIP Conf. Proc., 745, 797 (2005).*

[80] K. E. Gibbs, *International Cosmic Ray Conference, 2823 (2003).*

[81] J. A. Toner et al., *Presented at The International Cosmic Ray Conference (2007).*

[82] P. Cogan, *PhD Thesis (2006).*

[83] P. Jordan, F. Krennrich, *VERITAS internal memo on lightcone studies (2004).*

[84] A. Weinstein, *Presented at The International Cosmic Ray Conference (2007).*

[85] V. V. Vassiliev, J. Hall, D. B. Kieda, J. Moses, T. Nagai, J. Smith, *International Cosmic Ray Conference, 5, 2851, July (2003).*

[86] V. V. Vassiliev, *Colloboration Presentation on the CFD (2003).*

[87] S. Bradbury, *International Cosmic Ray Conference, 263 (1999).*

[88] E. Hays, *Presented at the International Cosmic Ray Conference (2007)*

[89] D. Horan, *PhD Thesis (2001).*

[90] "http://root.cern.ch".

[91] P. Cogan, *Presented at the International Cosmic Ray Conference (2007).*

[92] T. P. Li, Y. Q. Ma, *ApJ, 272, 317 (1983).*

[93] S. Schlenker, *PhD Thesis (2005).*

[94] W. Hofmann, I. Jung, A. Konopelko, H. Krawczynski, H. Lampeitl, G. Puhlhofer, *Astroparticle Physics, 12, 135143, November (1999).*

[95] M. K. Daniel, *Presented at the International Cosmic Ray Conference (2007).*

[96] D. Berge, S. Funk, J. Hinton, *A&A, 466, 12191229, May (2007).*

[97] A. Daum et al., *Astroparticle Physics, 8, 1 (1998).*

[98] G. Sembroski, *VERITAS internal note, wiki Spectrum Analysis, May (2008).*

[99] G. Maier, *VERITAS internal note, Elog Analysis And Calibration 595, October (2007).*

[100] M. Wood, *Veritas Internal Note, September (2008)*

[101] B. Humensky, *Veritas Internal Note, June (2008).*

[102] A. Weinstein *Veritas Internal Note, August (2008).*

[103] VEGAS Developers, *Veritas Internal Note, VEGAS Release Notes (2009).*

[104] A. Weinstein, *Veritas Internal Note, March (2009).*

[105] A. Weinstein, *Veritas Internal Note, June (2009).*

[106] F. Mavromatakis, *A&A, 408, 237 (2003).*

[107] Y. Uchiyama et al., *ApJ, 571, 866 (2002).*

[108] A. A. Abdo et al., *ApJ, 664, 91 (2007).*

[109] A. A. Abdo et al., *ApJS, 183, 46 (2009).*

[110] M.J. Lang et al., *A&A, 423, 415 (2004).*

[111] J. Albert et al., *Sciencexpress, 18 May (2006).*

[112] V.A. Acciari et al., *ApJ, 698, L133 (2009).*

[113] W. Bednarek, *Mon. Not. R. Astron. Soc., 345, 847 (2003).*

[114] A. Weinstein, *Veritas Internal Note, Aug. (2009).*

[115] A. Weinstein, *Veritas Internal Note, Aug. (2009).*

[116] J. Albert, et al. *ApJ, 675, 25 (2008).*

[117] R. Ong, *VERITAS ESAC Meeting, Veritas Internal Note, March (2007).*